Politecnico di Torino

Collegio di Ingegneria Meccanica, Aerospaziale e dell'Autoveicolo
Corso di Laurea in Ingegneria Aerospaziale - Aeromeccanica e sistemi

a.a. 2023/2024

Numerical model implementation and modeling of an EMA bench

Friction modelling of an epicyclic reducer

Relatori:
Prof. **Dalla Vedova Matteo**
Ing. **Bertone Matteo**
Prof. **Maggiore Paolo**

Candidato:
Luca Enrico Buonpensiero

Politecnico
di Torino

Abstract

In recent years, the aviation industry has been transitioning toward simpler and more efficient systems, aiming to reduce complexity while enhancing safety and reliability. This shift, driven by the "More Electric Aircraft" concept, is gradually replacing hydraulic systems with electromechanical ones, which promise to minimize maintenance, reduce costs, and improve overall system performance. This thesis focuses on the characterization and modelling of an Electromechanical Actuator (EMA), specifically targeting its integration into secondary flight control systems.

The primary objective of this work is to analyze the dynamic behaviour of an EMA through experimental testing on a bench at Politecnico di Torino, simulating the actuation of a secondary flight control. Using a Model-Based Systems Engineering (MBSE) approach, a mathematical model of the EMA was developed, taking into account the interactions between the various gearbox components, particularly the meshing of gears and the dissipative forces caused by friction. The new model improved upon previous High Fidelity (HF) models by more accurately reflecting real-world performance.

Throughout the analysis, it was shown that friction significantly affects the system's behavior, particularly at lower command speeds, where meshing forces become more relevant. The new friction model demonstrated a reduction in Root Mean Square Error (RMSE) when compared to the previous HF model, which exhibited increasing divergence from desired results at higher command inputs. This improved precision, especially in representing the angular position of the motor, confirms the validity of the friction-based approach.

Concluding the study, potential future developments include implementing gear degradation models and studying Prognostics and Health Management (PHM) to ensure long-term reliability of these systems. Additionally, incorporating the backlash effect into the current model could provide a more comprehensive understanding of gear dynamics and further enhance the model's accuracy.

This work represents a significant step forward in the understanding and modelling of EMAs, offering valuable insights for future developments in the aerospace industry and the continued advancement of More Electric Aircraft technologies.

Politecnico
di Torino

Politecnico
di Torino

Summary

Abstract 3

Figure Index 8

Tables index 9

1. Introduction 12

1.1. Traditional Mechanical Systems 13

1.2. The Advent of Fly-by-Wire Systems 15

1.2.1 The Evolution Toward Electromechanical Systems 16

1.3. The Electromechanical Servovalve 18

1.3.1. Electric actuation system 20

2. Activity and test bench description 21

2.1. Test bench 21

2.1.1 Activity description 25

2.2. High Fidelity model 27

2.3. High Fidelity Electro-mechanical actuator model description 28

3. Dynamic analysis 29

3.1. Physical model 30

3.2. Mathematical model 33

3.2.1. Solar shaft equilibrium equation 34

3.2.3. Elastic and viscous meshing forces 39

3.3. Simulation 41

3.4. Energy dissipation 43

3.4.1. Sliding losses of the meshing teeth 43

3.4.2. Estimation of the friction coefficient 44

3.5. Gear Meshing Geometry 46

3.6. Crawling speed 50

3.7. Friction pairs 51

3.8. Gear meshing stiffnesses 53

3.9. Phase differences in planets gear meshing 56

4. Simulink model 63

4.1. Block 1 and 2: Relative displacements and their derivatives 64

4.2. Block 3: Gear mesh elastic forces 65
4.3. Block 4: Gear mesh viscous forces 66
4.4. Block 5: Equations of motion 67
4.5. Block 6: Curvature radii of friction 69
4.6. Block 7: Calculation of friction losses for gearing 70
5. Comparison and final results 71
5.1. RMSE calculation 82
6. Conclusion and future developments 84
Appendix A 88
Appendix B 92
Bibliography 107

Politecnico di Torino

Figure Index

Figure 1.1: Airplanes Control devices;
Figure 1.2: Cables and pulleys on traditional mechanical systems;
Figure 1.3: Electromechanical servovalve;
Figure 1.4: Power-by-wire actuators and HSA composition. (a) EHA, (b) EMA, and (c) HAS;
Figure 1.5: Electromechanical actuator (EMA);
Figure 1.6: Scheme of an electric drive system;
Figure 2.1: Test bench flow diagram;
Figure 2.2: Microbox PLC SIMATIC IPC427E;
Figure 2.3: Control Unit CU310-2 PN and Power module;
Figure 2.4: Epicyclic reducer;
Figure 2.5: Converter;
Figure 2.6: CS 25.671 (d) details
Figure 2.7: High Fidelity model overview;
Figure 3.1: Modelization flowchart;
Figure 3.2: Main elements of the planetary gearbox;
Figure 3.3 Lumped-Parameter Dynamic Model;
Figure 3.4: Shaft torsional stiffness;
Figure 3.5: Free body diagram of the solar wheel;
Figure 3.6: Backlash function
Figure 3.7: Free body diagram of the satellite 1;
Figure 3.8: Free body diagram of the satellite 2;
Figure 3.9: Free body diagram of the satellite 3;
Figure 3.10: Contact segment;
Figure 3.11: External wheel curvature radii;
Figure 3.12: Internal wheel curvature radii;
Figure 3.13: Curvature radii along the solar-satellite contact line;
Figure 3.14: Curvature radii along the crown-satellite contact line;
Figure 3.15: Meshing between external and internal gears;
Figure 3.16: Lever arms and friction forces;
Figure 3.17: Mesh stiffness evaluation graph;
Figure 3.18: Contact segment ($\theta_p = {}^{2\pi}/_{z}$, angular pitch);
Figure 3.19: 2 Pairs of teeth in mesh;
Figure 3.20: Trend of mesh stiffness between sun gear and planets;
Figure 3.21: Trend of mesh stiffness between crown and planets;
Figure 3.22: Current behavior periodicity in the motor;
Figure 4.1: Simluink Friction model blocks;
Figure 4.2: Relative elastic displacements;
Figure 4.3: Relative elastic displacements derivates;
Figure 4.4: Elastic torque between the sun-planet and planet-ring gear meshes;

Figure 4.5: Viscous torque between the sun-planet and planet-ring gear meshes;
Figure 4.6: Equation of equilibrium for the sun gear;
Figure 4.7: Equation of equilibrium for the satellites;
Figure 4.8: Calculation of friction curvature radii;
Figure 4.9: Frictional torque losses in gear engagements;
Figure 5.1: Ramp 0.01, Motor and encoder angular position;
Figure 5.2: Detail of the almost oscillatory trend of motor angular position;
Figure 5.3: Ramp 0.02, Motor and encoder angular position;
Figure 5.4: Ramp 0.03, Motor and encoder angular position;
Figure 5.5: Ramp 0.04, Motor and encoder angular position;
Figure 5.6: Ramp 0.05, Motor and encoder angular position;
Figure 5.7: Ramp 0.06, Motor and encoder angular position of HF and HFF model;
Figure 5.8: Ramp 0.07, Motor and encoder angular position of HF and HFF model;
Figure 5.9: Ramp 0.08, Motor and encoder angular position of HF and HFF model;
Figure 5.10: Ramp 0.09, Motor and encoder angular position of HF and HFF model;
Figure 5.11: Ramp 0.1, Motor and encoder angular position of HF and HFF model;
Figure A.1: Single-stage epicyclic gear train;
Figure A.2: Top view epicyclic reducer;
Figure: A.3: Reducer shaft diagram;

Tables index

Table 2.1: Electric motor: Engineering data;
Table 2.2: Electric motor: Mechanical data;
Table 5.1: RMSE values
Table A.1: Planetary gearbox Datasheet

Politecnico
di Torino

1. Introduction

Flight controls play a central role in ensuring the safe and dependable operation of an aircraft during all phases of flight. These controls allow the pilot to modify the areas of wind-resistant control surfaces like ailerons, rudders, and lifts in order to control roll, yaw, and pitch. The ability to control these surface areas is essential not only for the normal agility of the aircraft but also for managing adverse weather, correcting deviations from the desired path, and responding promptly to in-flight emergencies. The doctor examined the patient thoroughly to determine the cause of his symptoms.[1]

Flight controls in the field of aviation have experienced significant evolution over time. During the early days of aviation, wind-resistant surface areas on airplanes were controlled using simple mechanical systems made up of steel cords, pulleys, and bars directly connected to the pilot's controls. Although the systems were simple and long-lasting, they required a significant amount of physical effort from the pilot, especially when operating larger aircraft or flying at high speeds. Additionally, the complete reliance on mechanics in these systems limited both the speed and precision of commands sent to the control surfaces.

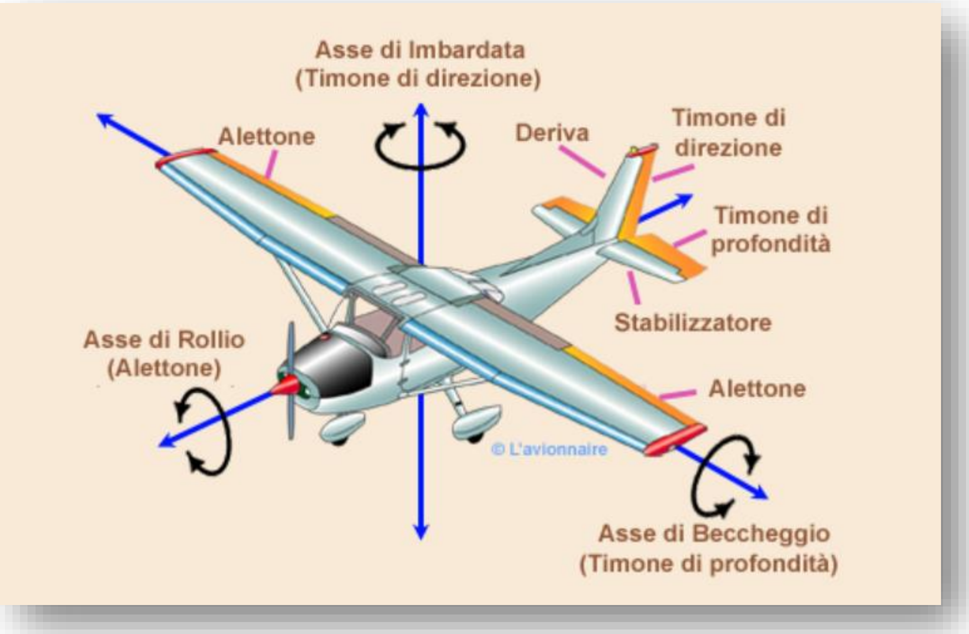

Figure 1.1: Airplanes Control devices [2]

As aircraft and missions grew more complex, the need for enhanced flight control systems became increasingly apparent. This need drove the development of assisted flight controls, which integrated mechanical and hydraulic power. In hydromechanical systems, the introduction of hydraulic actuators enabled the multiplication of the pilot's applied force, allowing for the control of progressively larger and heavier aircraft with minimal physical effort. These systems relied on hydraulic pumps that powered cylinders linked to the control surfaces, thereby transforming a small input from the pilot into a significantly amplified force.

1.1. Traditional Mechanical Systems

During the beginnings of aviation, flight control systems were completely mechanical due to the technology limitations and ease of building. The systems utilized steel cables, pulleys, levers, and linkages that connected the cockpit controls directly to the aerodynamic surfaces, including ailerons, rudders, and elevators. Every action taken by the pilot using the controls was sent to the control surfaces via a system of rods and cables, which, although sturdy and simple to upkeep, had some constraints.

Initially, the pilot had to exert a significant amount of physical effort due to the inertia of the mechanical components and aerodynamic resistance of the control surfaces, particularly when performing high-speed maneuvers or flying larger aircraft. The rise in aerodynamic forces while flying caused a corresponding rise in the force needed to operate the control surfaces, consequently restricting the maneuverability and efficiency of the aircraft's controls.
Additionally, mechanical systems had a tendency to experience issues with reliability and precision. Vibrations, wear of components, and regular adjustments could impact control effectiveness, causing mechanical play and delays in control surface response.

Another important drawback of conventional mechanical systems was their intricate design and integration into the aircraft's structure. The wires and wheels needed to be guided accurately inside the airplane, which led to more space being used and a higher total weight for the system. This also restricted the ability to add redundant systems, which are crucial for enhancing aircraft safety, particularly in complicated missions or demanding operational settings.

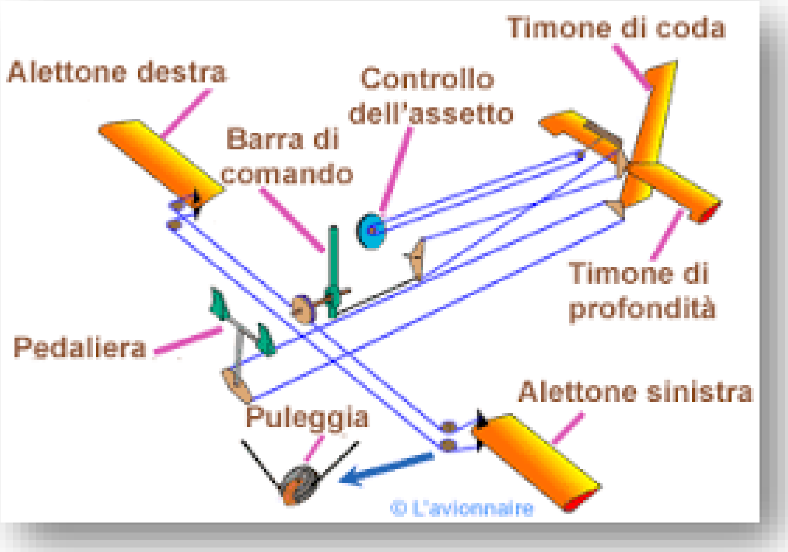

Figure 1.2: Cables and pulleys on traditional mechanical systems

A key aspect of fly-by-wire systems is the introduction of automation and electronic management of flight controls. Onboard computers do not merely transmit the pilot's commands but process them to optimize the aircraft's response, correcting any errors or compensating for changing atmospheric conditions. This allows the aircraft to maintain artificial stability, enhancing safety and reducing the pilot's workload, who can then focus on other critical tasks.

The flight control actuation systems, both hydraulic and electromechanical, play a crucial role in this context. Actuators are devices that convert control signals, sent by the fly-by-wire system or hydromechanical controls, into mechanical movements that directly operate the control surfaces. Hydraulic actuators, for example, use fluid pressure to generate powerful and precise movements, ideal for large aircraft or control surfaces requiring significant forces.

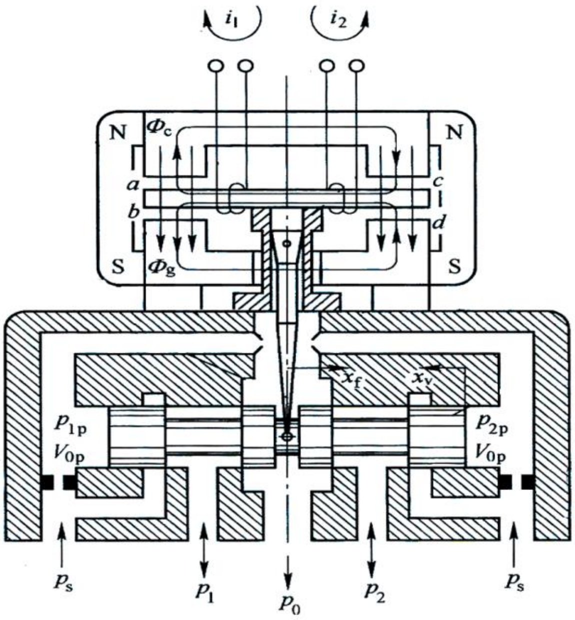

Figure 1.3: Electromechanical servovalve

1.2. The Advent of Fly-by-Wire Systems

Beginning in the 1970s, there was a push to enhance the accuracy, security, and adaptability of flight control systems, resulting in the creation of fly-by-wire (FBW) systems. These systems signify a technological shift in flight control, substituting conventional mechanical and hydraulic connections with fully electronic control systems.

In a fly-by-wire system, the pilot's instructions are not sent directly to the control surfaces through cables or hydraulic lines anymore. Instead, digital electrical signals are generated from the pilot's control movements through position sensors and transducers. The electrical signals are transmitted to onboard computers, which analyze the data in real-time, considering factors like airspeed, aircraft position, weather conditions, and planned maneuvers [3].

The core of the fly-by-wire system consists of flight control computers, which use advanced algorithms to interpret the pilot's commands and generate the appropriate control signals for the actuators that move the aerodynamic surfaces. This approach not only improves precision and response speed but also enables the implementation of automatic stabilization systems, fault protection, and emergency management, significantly reducing the pilot's workload.

Another major benefit of fly-by-wire systems is the capability to seamlessly incorporate additional functionalities like automated flight control systems, piloting assistance, and adaptive flight modes. These systems are able to adapt to flight conditions automatically, enhancing stability and safety, and enabling the pilot to concentrate on high-level tasks like mission management and strategic navigation.

Nonetheless, the shift to fly-by-wire systems brought about fresh hurdles, including the requirement to guarantee the dependability of electronic systems and protection against software malfunctions. In order to deal with these problems, present fly-by-wire systems are created with thorough redundant features, such as numerous control computers and replicated communication pathways, guaranteeing the system can still function safely even if one or more parts fail.

1.2.1 The Evolution Toward Electromechanical Systems

The ongoing advancements in technology have resulted in the creation of more complex flight control systems, especially those that utilize electromechanical components. These systems, merging fly-by-wire features with high-tech electromechanical actuators, embody state-of-the-art flight control technology.

High-precision electric motors are utilized in electromechanical actuators to create the motion of control surfaces. These actuators provide multiple benefits compared to conventional hydraulic systems, such as higher energy efficiency, lower system weight, and enhanced operational reliability. Moreover, due to the ability to control electric motors precisely through digital signals, electromechanical systems can offer rapid and accurate responses to changes in flight commands.

Sophisticated electromechanical systems are well-suited for tasks that demand precision and quick reactions, like advanced aircraft, drones, and space expeditions. Moreover, decreasing reliance on traditional hydraulic systems simplifies aircraft design and maintenance, reduces critical components, and enhances overall system reliability.[4]

Research [6] indicates that PBW (power-by-wire) actuators bring numerous advantages to actuation systems, primarily due to their fault-tolerant nature and the elimination of pipes and fluids. These benefits include:

a) enhanced safety and reliability, thanks to the absence of hazardous and flammable hydraulic fluids;
b) reduced weight, volume, and complexity in power transmission pathways (Figure 4);
c) simplified maintenance and lower costs, as there are no hydraulic leaks and diagnostics are improved;
d) greater energy efficiency and superior dynamic performance.

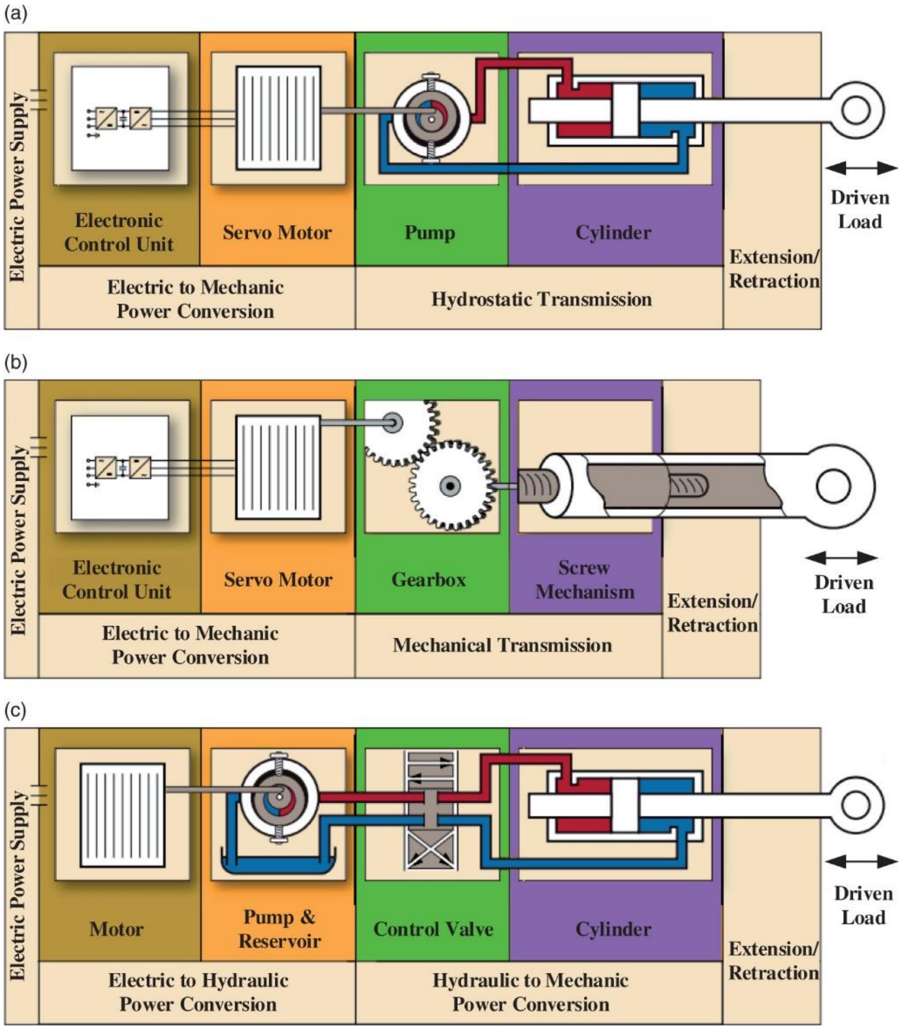

Figure 1.4: Power-by-wire actuators and HSA composition. (a) EHA, (b) EMA, and (c) HSA. [7]

These actuators are already integrated into operational aircraft, where EHAs and EMAs have matured sufficiently for use in recent large commercial transport aircraft. For example, EMAs are utilized in landing gear braking, mid spoiler surfaces, and the trimmable horizontal stabilizer on the Boeing 787. On the Airbus A380, EHAs are employed in primary flight controls (ailerons and elevators), while EMAs are used for slats, the trimmable horizontal stabilizer, and thrust reverser actuation. In military aviation, the Joint Strike Fighter features primary flight control systems driven by EHAs. Actuator engineers have estimated that PBW actuators and associated electrical systems could significantly reduce fuel consumption and maintenance costs in an all-electric passenger aircraft, leading to a 30-50% decrease in ground service equipment. In combat scenarios, military aircraft could see a reduction in take-off weight by 270-450 Kg and up to a 14% decrease in fuselage vulnerability. Although PBW actuators are relatively new to the aerospace industry, the MEA/AEA concept presents substantial future opportunities for these actuators.

As depicted in Figure 4(a), an EHA is essentially a self-contained hydraulic actuator with a pump driven by a variable-speed electric motor. In EHAs, power control is handled by the pump instead of traditional hydraulic systems, with adjustments in pump speed leading to changes in flow and hydraulic power levels. The electric motor and pump units regulate the position of the piston linked to the load by moving fluid between cylinder chambers, getting rid of the need for large piping systems and outside hydraulic sources. However, EMAs eliminate the necessity for hydraulic parts in the area, opting for mechanical drives to control the screw rod. This results in decreased maintenance needs, as well as a dependable, leak-proof operation. It is commonly acknowledged that EMAs generally have a weight advantage compared to EHAs when the actuation needs are the same. In spite of these advantages, engineers and researchers continue to face obstacles in progressing EMA technology for upcoming aircraft. In contrast to traditional hydraulic servo actuators, EMAs encounter various challenges such as limited understanding in areas like reliability, jamming risk, health monitoring, and thermal management. Conducting thorough experimental tests is vital to guarantee that airborne EMAs perform reliably.

This study reviews the development and testing of one particular linear EMA system, with a focus on its application in flight controls, tested on a test bench.

1.3. The Electromechanical Servovalve

EMAs are tools that utilize an electric motor to produce the necessary force or torque for adjusting aerodynamic surfaces, with the movement being transferred via a mechanical setup. This brushless motor is connected to a gear box and, when needed, a linear actuator like a ball or roller screw can be added. Digital power electronic devices manage the onboard electrical system to provide the necessary power.

In recent decades, the aerospace industry has been steadfast in its pursuit of developing "more electric" aircraft. This has led to a gradual, yet steady, increase in the adoption of electrical technology in flight control systems, starting with fly-by-wire and continuing with the integration of electromechanical actuators, partially replacing traditional hydraulic and electrohydraulic actuators. This transition has allowed for more versatile configurations, improved aircraft dynamics, and effectively addressed issues related to noise and vibration, particularly through the use of piezoelectric technologies. [9]

Despite the advancements made, electromechanical actuators (EMAs) have not yet reached full technological maturity and continue to present various safety issues. These problems can be partially mitigated through more complex designs, which, however, lead to increased production costs.

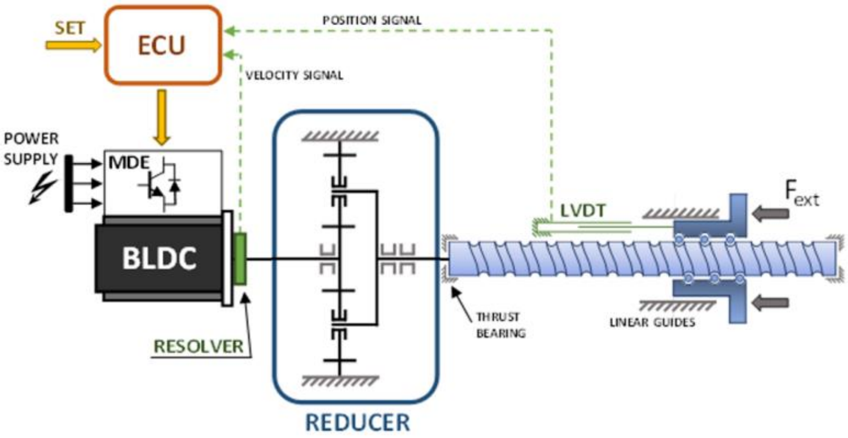

Figure 1.5: Electromechanical actuator (EMA) [10]

Because of safety issues, the utilization of EMAs as main actuators for flight control is presently restricted to experimental aircraft. Developing a strong Prognostics and Health Management (PHM) system could be a helpful approach in dealing with these difficulties by quickly identifying faults and correctly predicting the Remaining Useful Life (RUL) of deteriorating components.

Incorporating a PHM system into aircraft control parts poses numerous difficulties, which are exacerbated by the use of electromechanical technology. The primary obstacle is the insufficient experimental data available, as EMAs are not commonly used in flight control systems yet, resulting in a scarcity of trustworthy past data. Another problem stems from the restrictions of the computational power on board, leading to the need for basic functions and effective algorithms to evaluate the health of each monitored component. Moreover, the complexity of extracting useful data during flight is increased by the unpredictable commands given to the actuators and the fluctuating loads from gusts and turbulence, necessitating a reduction in the number of sensors to prevent higher costs and reliability problems. Ultimately, the prognostic algorithm must accurately capture the nonlinear nature of both the monitored system and degradation modes, as well as the influence of non-Gaussian noise, in order to minimize uncertainty in predictions and achieve optimal accuracy.

1.3.1. Electric actuation system

An actuation system is described as a system that can generate and manage the movement of a mechanical part (mechanical load). The controlled mechanical load parameters can be static (position), kinematic (velocity), or dynamic (acceleration, torque, or force). Each actuation system consists of a power element, referred to as the actuator, that is tasked with producing the mechanical effort linked to the movement. This actuator may be hydraulic, pneumatic, electric, or of a different kind.

An electric drive system is defined as one that utilizes an electric actuator, i.e., an electric machine, typically operating as a motor, in which energy is converted from electrical to mechanical form (electromechanical energy conversion). Motion control is achieved by regulating the motor's supply parameters (voltage, current, frequency).

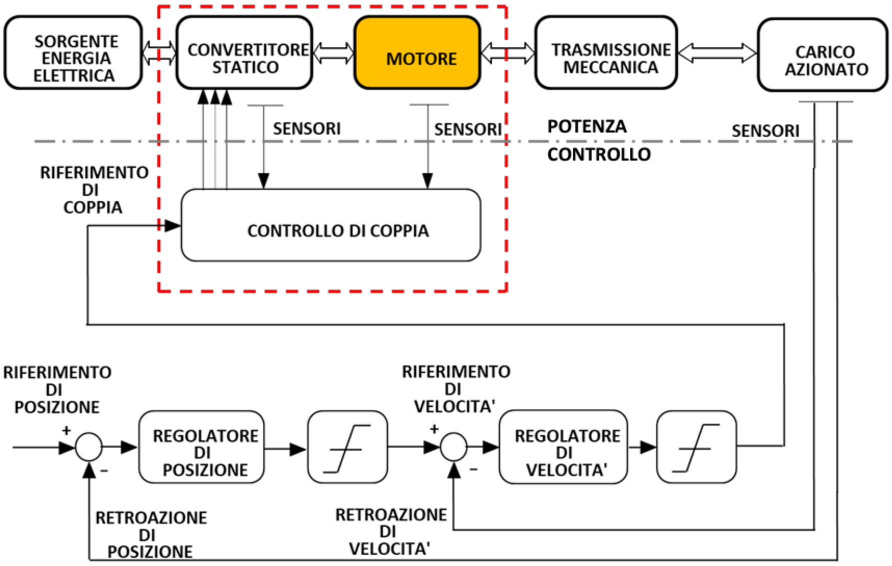

Figure 1.6: Scheme of an electric drive system

To accomplish this, a power device is interposed between the motor and the electrical energy source (such as the public electricity grid) to provide the motor with the required voltage, current, and frequency levels. Excluding solutions that use rotating converters, this device will generally be a static converter, composed of a power electronics structure employing components such as diodes, thyristors, transistors, etc., and possibly a transformer (to adjust the voltage level and/or the number of phases). The basic schematic of a generic electric drive system is shown in Figure 1.6. [8]

2. Activity and test bench description

2.1. Test bench

Over the years, numerous research projects and theses at the Politecnico di Torino have led to the development, assembly, and study of a test bench that replicates an electromechanical actuator. The test bench was assembled at the research laboratory of the DIMEAS department at the Politecnico, where the EMA bench tests and measurements were carried out. The only difference from a real actuator is the absence of a linear conversion of the rotational motion generated by the gearbox. Instead, an encoder, a sensor for measuring the angular position, is mounted on a smaller gear that meshes directly with the gearbox output. The test bench consists of the following components:

- **Control unit**: The control unit essentially drives the motor when a command is issued by the user through the Siemens human-machine interface platform. It processes the desired command and the rotor position, applying the control law to determine the correct phase commutation. This operation is physically carried out by the inverter (Power unit).

- **Power module**: The inverter is responsible for converting the three-phase current based on the rotor's position. The frequency at which the inverter switches the phases directly affects the speed of the rotating magnetic field and, consequently, the speed of the motor's rotation. In this way, a rotating magnetic field is generated inside the motor, which interacts with the magnetic field of the permanent magnets, causing the motor to rotate.

- **Microbox PLC**: The programmable logic controller runs Siemens' TIA software, which contains a detailed model of the servomechanism. With this program it is possible to teach the desired command to the servomechanism (step, ramp, sinusoid).

- **Converter**: The test bench contains two converters; The converter transforms from 220V to 24V and is used to correctly power the power plant.
- **Electric motor**: Generates mechanical power to drive the servomechanism. The motor is an 8-pole PMSM (permanent magnet synchronous motor) with three-phase power supply.
- **Epicyclic reducer or Gearbox**: Made at the Polytechnic using Fused Deposition Modelling (FDM) technology, it is connected to the electric motor shaft. The reducer has 2 stages and a transmission ratio of 124. The detail of the reducer in its stages and transmission ratios are explained in Appendix A.

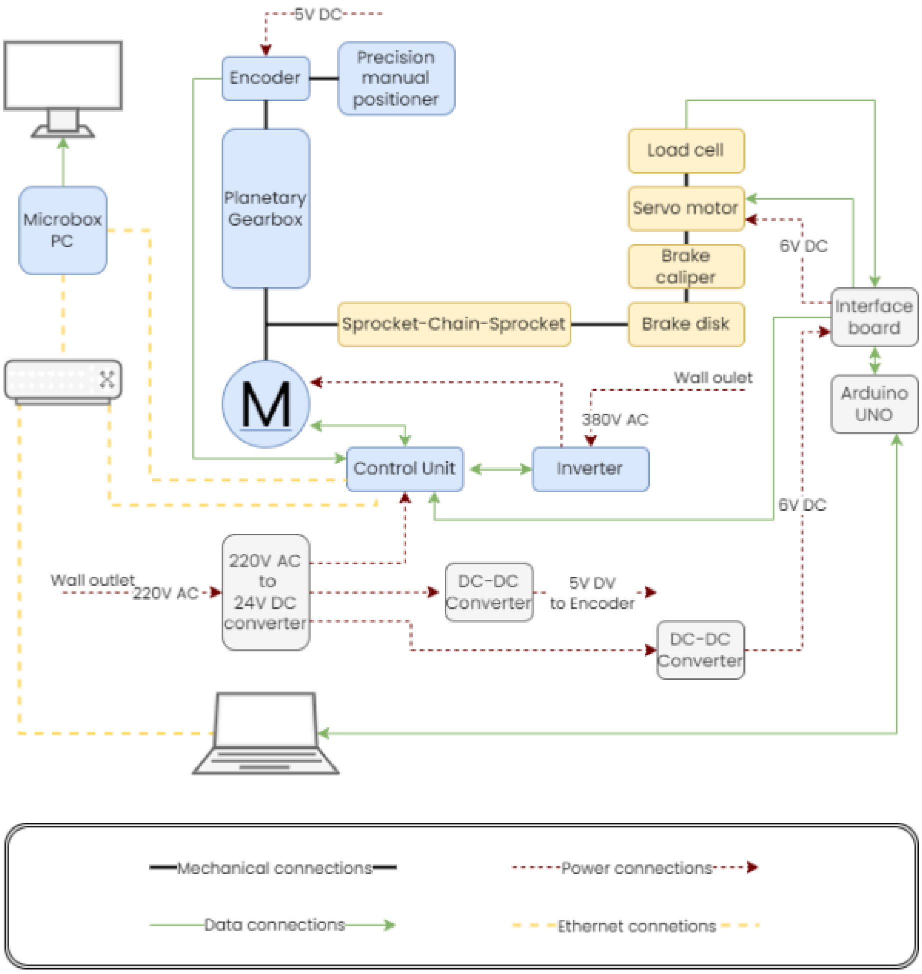

Figure 2.1: Test bench flow diagram [11]

Figure 2.2: Microbox PLC SIMATIC IPC427E;

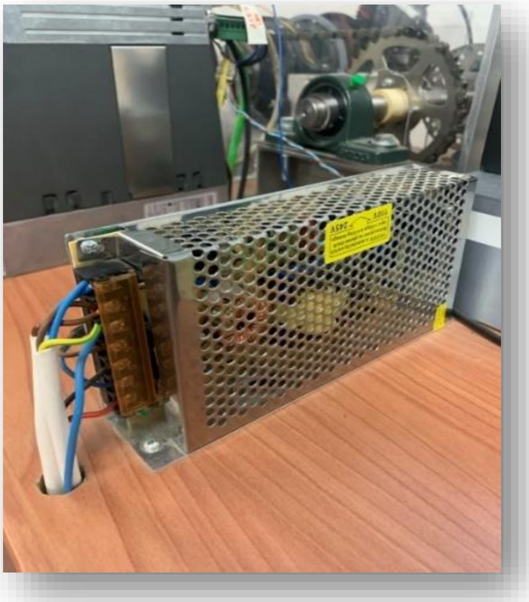

Figure 2.3: Control Unit CU310-2 PN and Power module;

Figure 2.4: Epicyclic reducer;

Figure 2.5: Converter;

The technical details of the devices follow:

Technical data	
Rated torque (100 K)	5.3 Nm
Static torque (60 K)	5.00 Nm
Static torque (100 K)	6.0 Nm
Rated speed (100 K)	2000 rpm
Number of poles	8
Rated current	3.0 A
Stall current (60 K)	2.55 A
Stall current (100 K)	3.15 A
Moment of inertia	7.700 kg*cm2
Efficiency	90 %

Table 2.1: Electric motor: Engineering data

Mechanical Data	
Motor type	Permanent-magnet synchronous motor
Shaft height	63
Cooling Natural cooling	Cooling
Radial runout tolerance 0.040 mm	0.040 mm
Concentricity tolerance 0.10 mm	0.10 mm
Axial runout tolerance 0.10 mm	0.10 mm
Vibration severity grade	Grade A
Connector size	1
Degree of protection	IP64
Temperature monitoring	Pt1000 temperature sensor
Electrical connectors	Connectors for signals and power
Encoder AM24DQI	Absolute encoder 24 bits

Table 2.2: Electric motor: Mechanical data

2.1.1 Activity description

The purpose of the sperimental activity is to study the EMA actuator under different commands in order to evaluate, through the model-based systems engineering (MBSE) approach, the friction present in the gearbox and how it affects the commanded position of the end user, that could be associated with the drive of a plane's mobile surface.

This EMA test bench fairly accurately replicates a real electromechanical servomechanism. As EMA systems are increasingly being adopted in the aerospace sector, as introduced in Chapter 1, the aim of this study is to analyze its practical implementation. In general, EMAs are finding their application in the actuation of secondary flight controls, which typically operate at ranges between 5-6 $°/s$ (high-lift devices) and 20-30 $°/s$ (spoilers and airbrakes). For the typical actuation speed of primary and secondary flight controls in large commercial aircraft, the relevant regulatory framework is found within **CS-25** (Certification Specifications for Large Aeroplanes) and its amendments under **EASA** (European Union Aviation Safety Agency) regulations. Specifically, these regulations address general requirements for flight control systems and their functionality, ensuring smooth and effective operations during various phases of flight. [28].

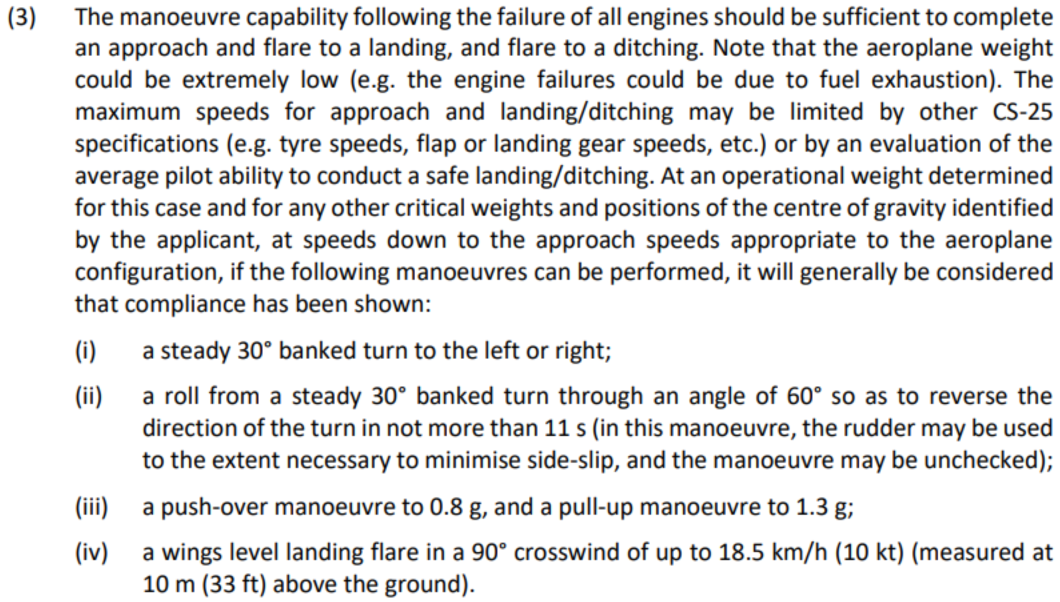

(3) The manoeuvre capability following the failure of all engines should be sufficient to complete an approach and flare to a landing, and flare to a ditching. Note that the aeroplane weight could be extremely low (e.g. the engine failures could be due to fuel exhaustion). The maximum speeds for approach and landing/ditching may be limited by other CS-25 specifications (e.g. tyre speeds, flap or landing gear speeds, etc.) or by an evaluation of the average pilot ability to conduct a safe landing/ditching. At an operational weight determined for this case and for any other critical weights and positions of the centre of gravity identified by the applicant, at speeds down to the approach speeds appropriate to the aeroplane configuration, if the following manoeuvres can be performed, it will generally be considered that compliance has been shown:

(i) a steady 30° banked turn to the left or right;

(ii) a roll from a steady 30° banked turn through an angle of 60° so as to reverse the direction of the turn in not more than 11 s (in this manoeuvre, the rudder may be used to the extent necessary to minimise side-slip, and the manoeuvre may be unchecked);

(iii) a push-over manoeuvre to 0.8 g, and a pull-up manoeuvre to 1.3 g;

(iv) a wings level landing flare in a 90° crosswind of up to 18.5 km/h (10 kt) (measured at 10 m (33 ft) above the ground).

Figure 2.6: CS 25.671 (d) details

In this study, it has been observed that the meshing between the shafts and the gears of the reducer actually degrades the final angular position of the motor, and consequently of the load, leading to significant effects. For example, consider a mobile surface commanded to deploy at 6 $^{\circ}/s$ but actually extending at 4.5 $^{\circ}/s$ cause friction. For actuation times of secondary controls, which can take up to 10-20 seconds, this discrepancy results in noticeable differences. In real world scenarios, this would put the pilot in a more difficult and complex control situation, where a movable surface (or more) might be deployed at 70 degrees instead of the commanded 80-90 degrees, with increased safety risks.

In practice, what is done is to issue a command through the Siemens platform, which acts as an interface between human and machine, and convert it into a specific electrical impulse. This impulse, circulating in the motor's coils, generates a driving torque on the motor shaft, which is connected to the epicyclic gearbox and sets the rest of the gear mechanism in motion. The command issued via the platform is a command on the output shaft, i.e., on the encoder; for example, a command of 0.03 rad/s corresponds to a rotation of the encoder at 0.03 rad/s, or 1.72 degrees per second.

Some tests were carried out to calculate the degradation of the command by executing only ramp commands of various amplitudes. It is important to note that, for the extension of a secondary flight surface, a ramp command of a certain amplitude is issued, which corresponds to the speed at which we want the surface to be deployed.

10 tests were performed with 10 increasing ramp commands, starting from the smallest (approximately 0.6 $^{\circ}/s$) to the largest (6 $^{\circ}/s$), to observe how friction affects the motor at different speeds. The command test are called by increasing numbers ‘0.01, 0.02, … 0.09, 0.1’ because this writing indicates respectively a ramp command with an amplitude of 0.01 radiant/s, 0.02 rad/2 and so on. Additionally, the previously developed HF model was also used to evaluate how reliable it is for this type of command and to possibly compare it with the subsequently created model.

Here the logical path taken is outlined:

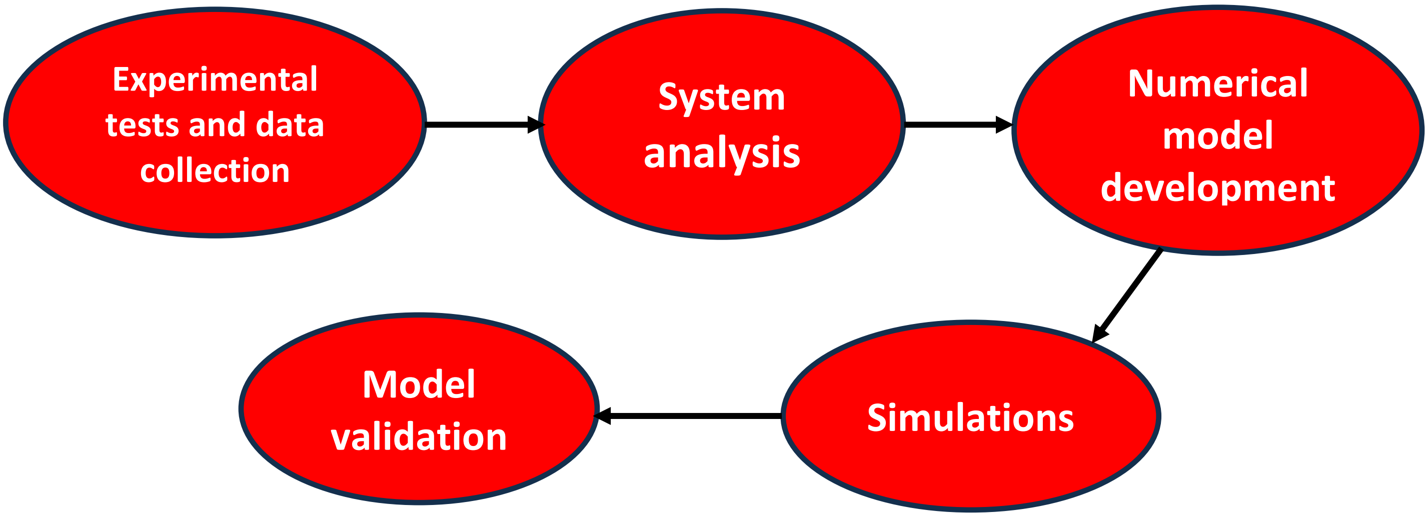

2.2. High Fidelity model

In previous works, a numerical model was developed that can accurately replicate the behavior of the actual test bench components. Previous studies focused on the possibility of replicating the behavior of a system characterized by reaction times between those of a primary flight control and those of a secondary flight control. As a result, a Matlab Simulink model has been developed, using an integration step of $1 * 10^{-6}$ s. This allows for a faithful representation of the system's electronic components' behavior, remaining one or two orders of magnitude below the characteristic time of the electronic part itself. [12]

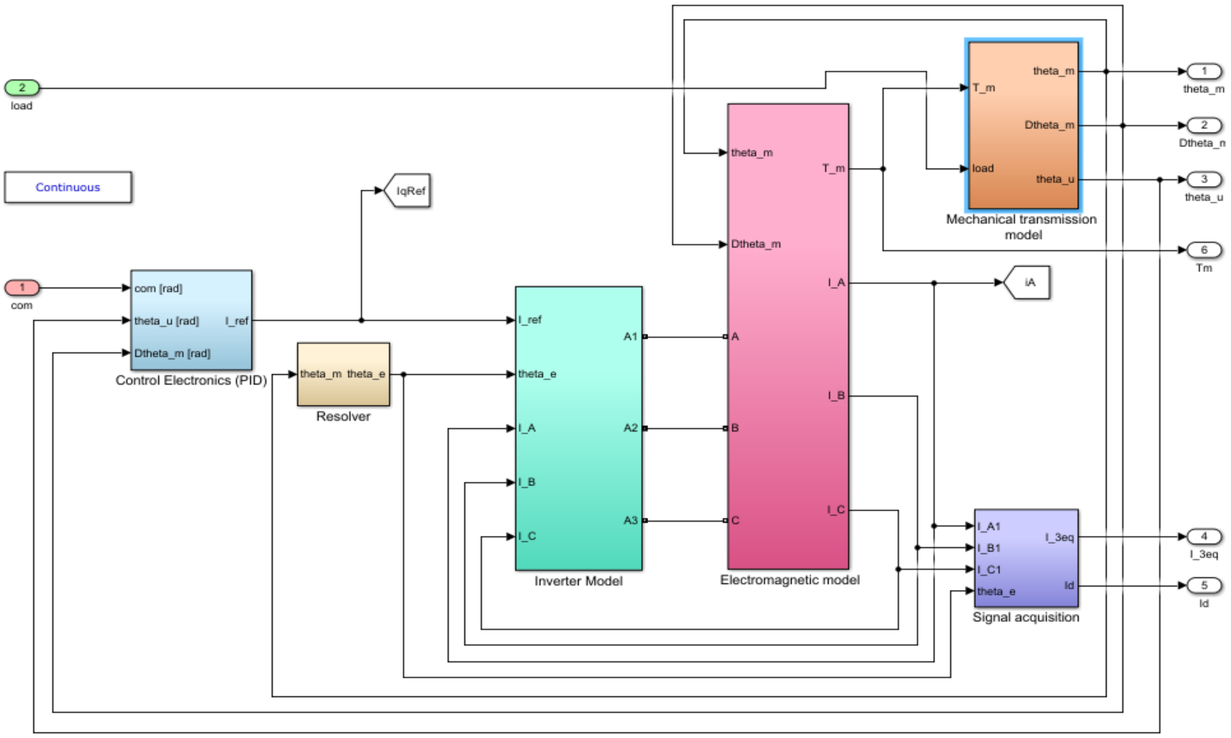

Figure 2.7: High Fidelity model overview

Given the need to replicate the system's behavior over long time intervals, a fixed-step integration method, ODE 1, also known as Euler's method, was adopted; this choice has a lower cost in terms of required memory, although more demanding in terms of computational resources.

2.3. High Fidelity Electro-mechanical actuator model description

As we saw in the figure 2.7, the model built by previous works is composed of numerous sub-systems, that we briefly describe:

- Control Electronics (PID): The PWM (Pulse Width Modulation) controller, receives as input the command and transforms it into a reference current that is applied to the motor. In the aerospace field, PID controllers are widely used;

- Resolver: Converts the angular position of the motor into an electrical angular position, used than by the inverter to control the three currents inside the three-phase motor;

- Inverter Model: Transforms the modulated signal from the controller into a supply current for the motor. The information signal must be translated into a high-power signal before, for this there is an H-bridge, an electronic circuit composed of diodes and transistors, commonly used in aviation to solve this problem.

- BLDC electromagnetic model: The sub-system of the electric motor, that provides as output the torque supplied, which is engaged via the motor-shaft directly into the gearbox;

- Motor-transmission dynamical model: Is the mechanical part of the actuator. It contains the equations of motion and the mathematical model studied in this work, that calculates the friction and the meshing between motor-shaft/planes and planets/crown. Having as input the torque delivered, it returns as output the angular displacement of the motor and the user (encoder).

- Signal acquisition: this block has nothing to do with a real electromechanical actuator component, but it is used for the elaboration of some data generated by the simulation. The subsequent sections will focus on describing each individual sub-system to gain a comprehensive understanding of the working flow of the model [13][14].

This work presents the modifications made to the *'Motor-transmission dynamical model'* block, taking into account the physical meshing between the gears, the exchange of forces, and the calculation of friction and its torque acting on the shafts. The detailed explanation is provided in Chapter 4. Following this, the mathematical model used to implement the equations governing the mechanical phenomenon is described.

3. Dynamic analysis

Once the electronic components of the test bench and the block model in Simulink have been described, we can analyze the planetary gearbox, which is at the core of the friction phenomena. Its modeling, like any mechanical system, is carried out in several steps illustrated in the figure 3.1.

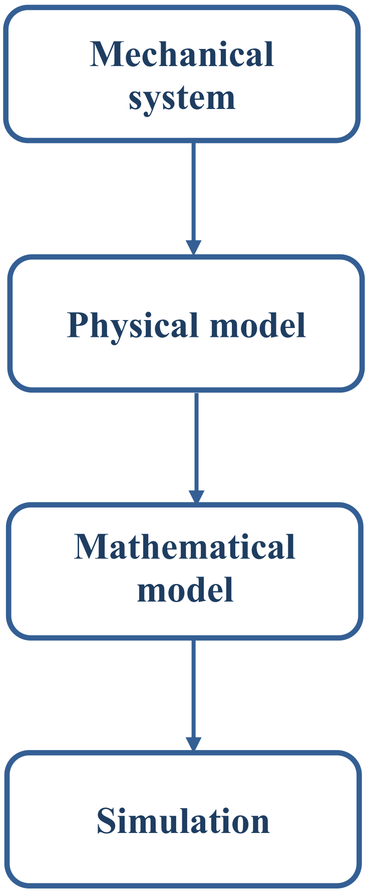

Figure 3.1: Modellization flowchart

For the mechanical system, refer to Appendix A, which contains a detailed description of the components in the gearbox.

3.1. Physical model

The physical model represents a system equivalent to the mechanical system, based on certain assumptions made to simplify the model. In this case, an elasto-dynamic analysis was chosen. The model takes into account quantities such as:

- The inertia of the bodies;
- The stiffness and damping of the bodies;
- The backlash between the rings;

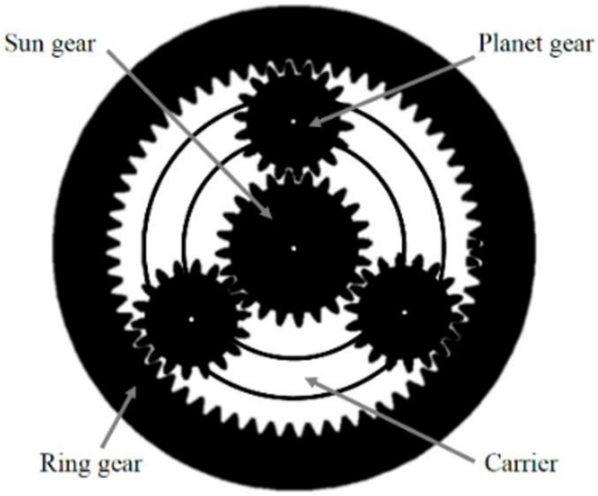

Figure 3.2: Main elements of the planetary gearbox [15]

Backlash has been previously studied [12], and therefore it is not considered in this thesis work.

The planetary gearbox's dynamic behavior was analyzed with a rotational mathematical model that simplifies the equations of motion and reduces computational costs. Nevertheless, not all translational effects (and therefore the bearing reactions) are considered.[16]

The model was designed for a particular gearbox, but it was also configured to be suitable for any planetary gearbox with three planets in the reduction stage. In any scenario, it can be readily adjusted for systems containing more than three planets.

The gear mesh stiffness is represented as springs, with damping elements placed in parallel to simulate viscous effects.

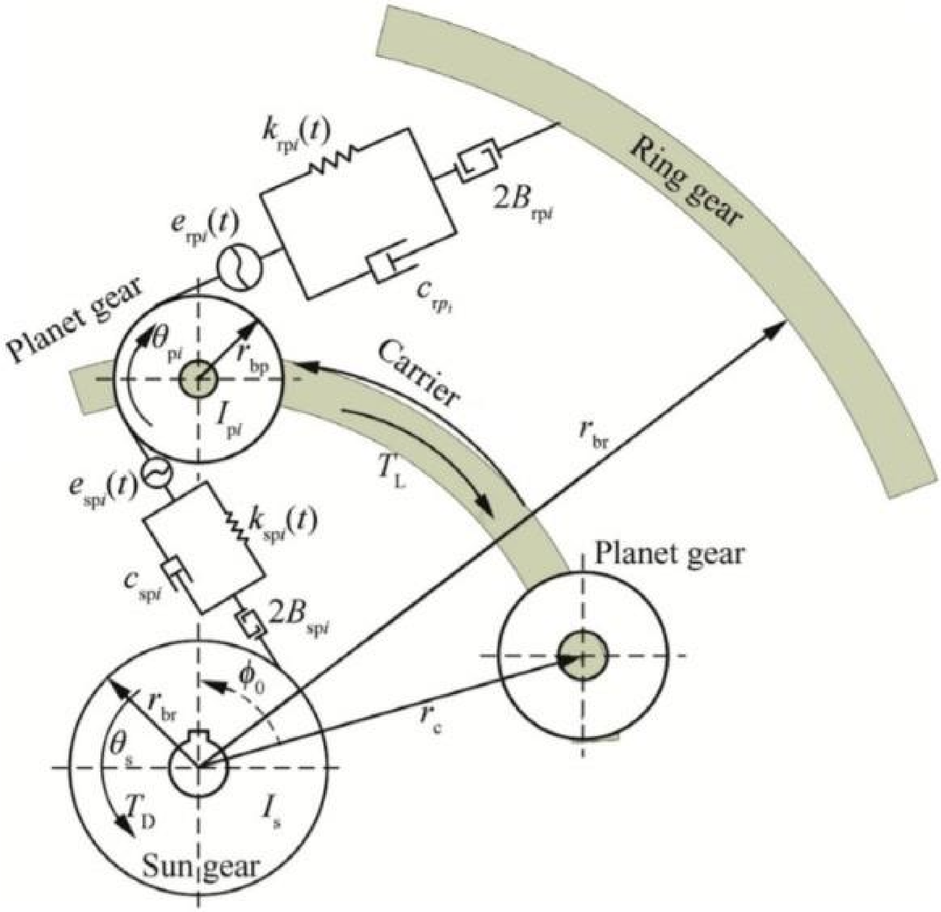

Figure 3.3 Lumped-Parameter Dynamic Model [16]

The chosen modeling methodology is the lumped parameter approach, which considers elastic elements as massless and mass elements as rigid. The correct selection of parameters (such as masses, stiffnesses, damping, etc.) allows for the development of a reliable model for the overall study of the system's dynamics.

So we can write the stiffness and damping coefficient of a generic shaft as:

$$K_{\theta} = \frac{I_p * G_s}{L_s} \tag{3.1}$$

$$C_s = 2 * \varepsilon * \sqrt{K_\theta * m_s} \tag{3.2}$$

With:

- $\mathrm{I}_p = \frac{\pi}{2} * r_s^4$ the polar moment of inertia of the section [mm^4] with r_s the radius of the shaft;
- G_s the shear modulus [GPa];
- L_s the length of the shaft section [mm];
- m_s the mass of the shaft;
- ε the damp ratio, calculated in the script matlab called *dinamica riduttore*.

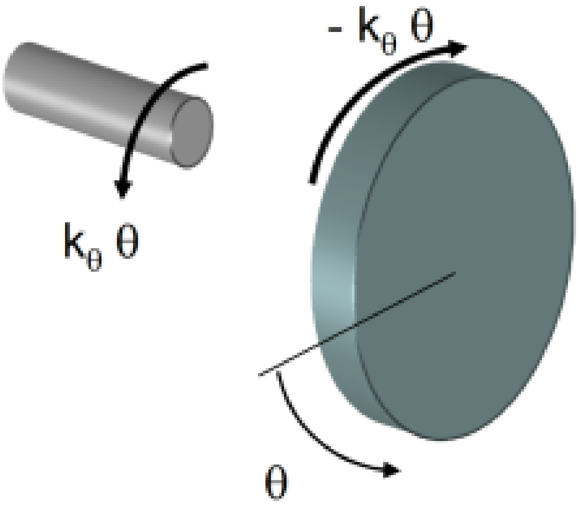

Figure 3.4: Shaft torsional stiffness

3.2. Mathematical model

Having chosen a dynamic model with lumped parameters, with reference to figure 3.3 we can introduce a series of parameters and initial simplifying hypotheses:

- Equal and constant viscous damping coefficients for ring-planet gears $crp1 = crp2 = crp3 = crp$;
- Equal and constant viscous damping coefficients for sun-planet gears $csp1 = csp2 = csp3 = csp$;
- Equal and constant ring-planet gear mesh stiffness $krp1=krp2=krp2=krp$;
- Negligible transmission error $esp \simeq 0$ and $erp \simeq 0$;
- Pressure angle of sun-planet α_{sp} and ring-planet α_{rp} constant during the meshing.

The equations of motion developed for each rotating element of the reducer are presented below. The equations of motion are reported, considering the 5 degrees of freedom of the gearbox: rotation of the sun-gear, rotations of the 3 satellites, rotation of the train carrier and the crown, that has been considered fixed.

We define the following quantities:

- T_D Input torque to the sun gear [Nm];
- T_L Load tourqe on the planet carrier [Nm];
- r_{bp} Base radius of the planet gears [m];
- r_{br} Base radius of the ring gear [m];
- r_{bs} Base radius of the sun gear [m];
- r_c Radius of the planet carrier [m];
- c_{sp} Viscous damping coefficient of the sun-planet gears [kg/s];
- c_{rp} Viscous damping coefficient of the ring-planet gears [kg/s];

- k_{sp} Sun-planet gear mesh stiffness [N/m];
- k_{sp} Ring-planet gear mesh stiffness [N/m];
- I_{sol} and I_{sat} the the moments of inertia of the motor-shaft and the satellites (same for all satellites while a little bit different from the driven-shaft)

3.2.1. Solar shaft equilibrium equation

The free body diagram of the solar wheel was created with $r_{bs} = radius\ of\ the\ solar\ base$, in order to derive the equation of motion:

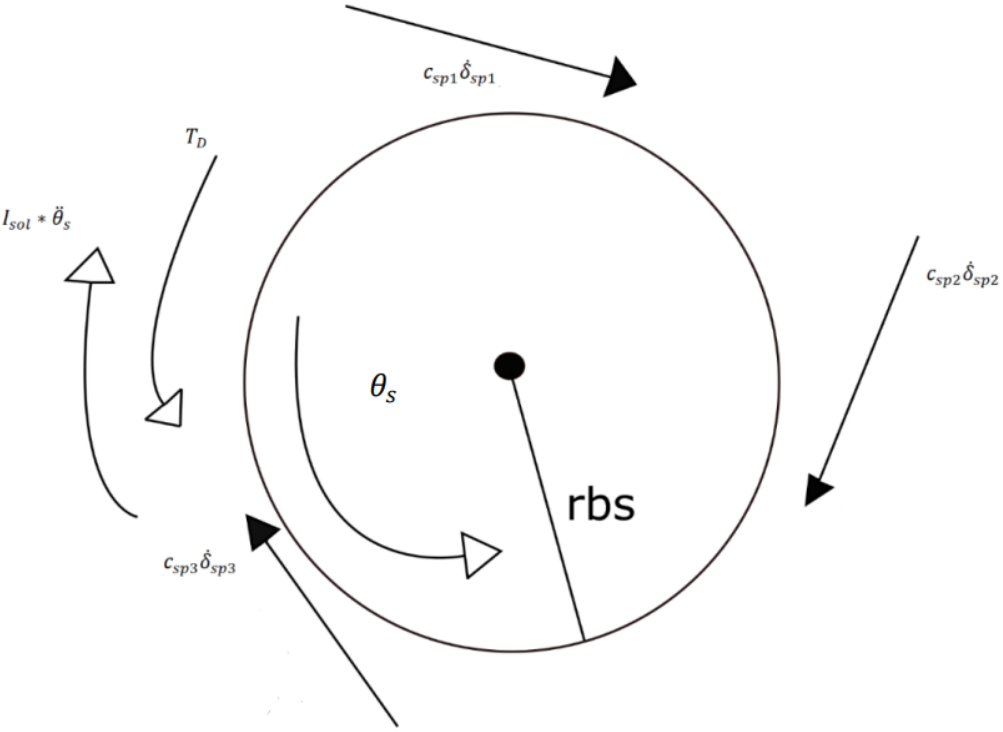

Figure 3.5: Free body diagram of the solar wheel

From which the following equation of motion derives:

$$T_D - \; r_{bs} * (c_{sp1}\dot{\delta}_{sp1} + c_{sp2}\dot{\delta}_{sp2} + c_{sp3}\dot{\delta}_{sp3}) - r_{bs} * (k_{sp1} * f(\delta_{sp1}, B_{sp1}) + k_{sp2} * f(\delta_{sp2}, B_{sp2}) + k_{sp3} * f(\delta_{sp3}, B_{sp})) = I_{sol} * \ddot{\theta}_S \tag{3.3}$$

The $f(\delta_{spi}, B_{spi})$ terms are the *backslash function*; Backlash represents the clearance between two interacting moving parts and is essential to allow relative rotation between them.

This phenomenon is particularly evident in mechanical systems equipped with a driving gear and a driven gear that are not directly interconnected, meaning that the motor shaft and the load shaft are connected to each other through intermediate gear trains.

The function representing the backlash phenomenon is shown in Figure 3.6 and can be expressed as:

$$f(\delta, B) = \begin{cases} \delta - B & if \quad \delta > B \\ 0 & elseif \quad -B < \delta < B \\ \delta + B & else \quad \delta < -B \end{cases} \tag{3.4}$$

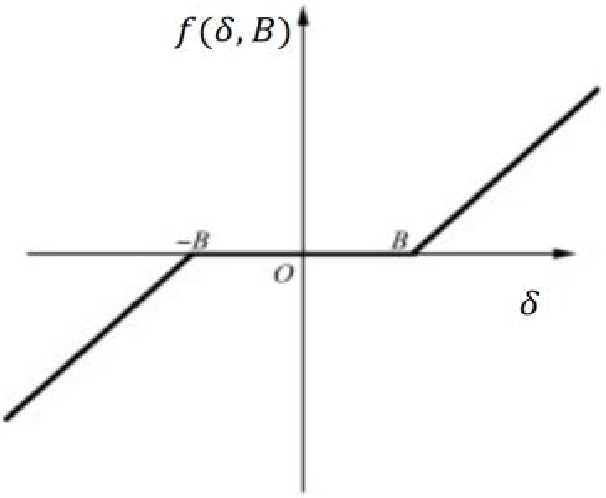

Figure 3.6: Backlash function

- δ (delta)**:** represents the relative displacement or angular error between two components in a transmission system, such as the angular error between the driven and driving gear teeth in a gear mesh.
- *B* (backlash)**:** represents the magnitude of mechanical play or the angular distance that can be traveled before the gear teeth re-engage. It quantifies the clearance between gear teeth before motion is transmitted from the driving to the driven element

Since this has already been tested and validated in previous models, for convenience it has not been considered in this model. Since the latter is already very complex and large, including the backslash would have weighed down the computational load of the Simulink program too much. Therefore in our model it will be $f(\delta spi, Bspi) = 1$;

For simplicity, it will no longer be included in the equations.

3.2.2. Relative rotation balance of the satellite shafts with respect to the train carrier.

As previously mentioned, since the model is purely rotational, the gyroscopic effects resultingv from the rotation of the three planet gears around the carrier axis are not considered. The equilibrium equations are as follows:

Satellite 1:

$$\left(k_{sp1} - k_{rp1}\right) * r_{bp} + \left(c_{sp1} * \delta'_{sp1} - c_{rp1} * \delta'_{rp1}\right) * r_{bp} = \mathrm{I}_{sat} * \ddot{\Theta}_{p2\_c} \qquad (3.5)$$

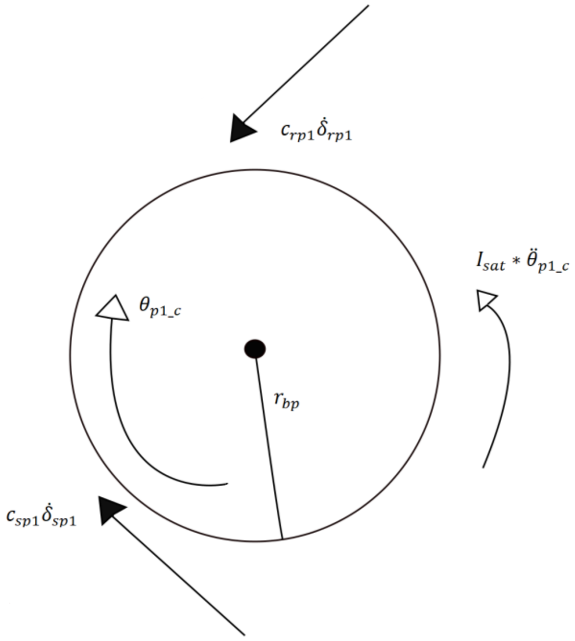

Figure 3.7: Free body diagram of the satellite 1;

Satellite 2:

$$(k_{sp2} - k_{rp2}) * r_{bp} + (c_{sp2} * \delta'_{sp2} - c_{rp2} * \delta'_{rp2}) * r_{bp} = \mathrm{I}_{sat} * \ddot{\Theta}_{p2\_c} \tag{3.6}$$

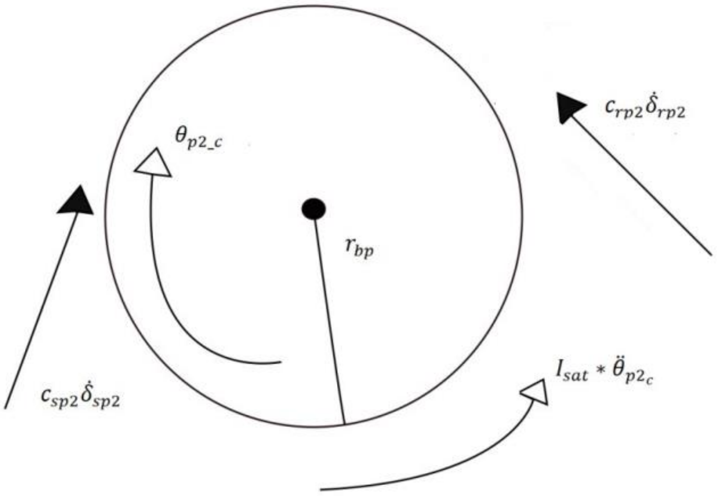

Figure 3.8: Free body diagram of the satellite 2

Satellite 3:

$$\left(k_{sp3} - k_{rp3}\right) * r_{bp} + \left(c_{sp3} * \delta'_{sp3} - c_{rp3} * \delta'_{rp3}\right) * r_{bp} = \mathrm{I}_{sat} * \ddot{\Theta}_{p3\_c} \qquad (3.7)$$

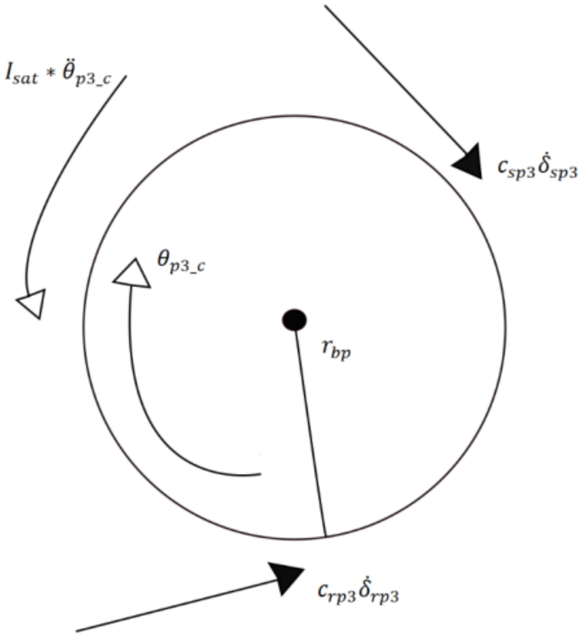

Figure 3.9: Free body diagram of the satellite 3

There is also the final equation related to the rotation of the planet carrier, located in the second stage of the gearbox, which drives the final gear connected to the encoder. In our model, this equation was not created as it is unnecessary. Our main interest is to calculate the correct motor angular position, which, through the transmission ratio τ, will directly give us the angular position of the load.

In any case, this would have been the relevant equation:

$$
\begin{aligned}
&(c_{sp1}\dot{\delta}_{s}p1 * r_c * \cos(\alpha_{sp}) + c_{rp1}\dot{\delta}_{r}\, p1 * r_c * \cos(\alpha_{rp}) + \\
&c_{sp2}\dot{\delta}_{s}p2 * r_c * \cos(\alpha_{sp}) + c_{rp2}\dot{\delta}_{r}\, p2 * r_c * \cos(\alpha_{rp}) + c_{sp3}\dot{\delta}_{s}p3 * \\
&r_c * \cos(\alpha_{sp}) + c_{rp3}\dot{\delta}_{r}p3 * r_c * \cos(\alpha_{rp})) + (k_{sp1} * r_c * \cos(\alpha_{sp}) + \\
&(k_{rp1} * r_c * \cos(\alpha_{rp}) + (k_{sp2} * r_c * \cos(\alpha_{sp}) + (k_{rp2} * r_c * \cos(\alpha_{rp}) + \\
&(k_{sp3} * r_c * \cos(\alpha_{sp}) + (k_{rp3} * * r_c * \cos(\alpha_{rp})) - T_L = I_{car} * \ddot{\theta}_{car}
\end{aligned}
\tag{3.8}
$$

With rc the radius of the satellite carrier.

3.2.3. Elastic and viscous meshing forces

The dynamic meshing forces mainly depend on variations in mesh stiffness and transmission errors. These forces, which vary during rotation, are transmitted through the supports to the gearbox housing.

Elastic meshing forces

Elastic force on the solar is:

$$F_{elast}^{sol} = k_{sp1} * \delta_{sp1} + k_{sp2} * \delta_{sp2} + k_{sp3} * \delta_{sp3} \tag{3.9}$$

On the satellites:

$$F_{elast}^{sat1} = k_{sp1} * \delta_{sp1} - k_{rp1} * \delta_{rp1} \tag{3.10}$$

$$F_{elast}^{sat2} = k_{sp2} * \delta_{sp2} - k_{rp2} * \delta_{rp2} \tag{3.11}$$

$$F_{elast}^{sat3} = k_{sp3} * \delta_{sp3} - k_{rp3} * \delta_{rp3} \tag{3.12}$$

Viscous meshing forces

On the solar:

$$F_{visc}^{sol} = c_{sp1} * \delta'_{sp1} + c_{sp2} * \delta'_{sp2} + c_{sp3} * \delta'_{sp3} \tag{3.13}$$

On the satellites:

$$F_{visc}^{sat1} = c_{sp1} * \delta'_{sp1} - c_{rp1} * \delta'_{rp1} \tag{3.14}$$

$$F_{visc}^{sat2} = c_{sp2} * \delta'_{sp2} - c_{rp2} * \delta'_{rp2} \tag{3.15}$$

$$F_{visc}^{sat3} = c_{sp3} * \delta'_{sp3} - c_{rp3} * \delta'_{rp3} \tag{3.16}$$

The equations 3.17 to 3.28 express the relative movements between the various components of the gear system, such as the sun gear and the planet gears. These displacements are given by the differences in angular velocities and positions of the components. Physically, this represents the deformation of the gears during meshing. Their importance lies in describing how the gear teeth move relative to each other during engagement.
The displacements and their derivative along the sun-planet gear meshes were calculated as follows:

$$\delta_{sp1} = r_{bs} * (\theta_s - \theta_c) - r_{bp} * \theta_{p1\_c} \tag{3.17}$$

$$\delta'_{sp1} = r_{bs} * (\theta'_s - \theta'_c) - r_{bp} * \theta'_{p1\_c} \tag{3.18}$$

$$\delta_{sp2} = r_{bs} * (\theta_s - \theta_c) - r_{bp} * \theta_{p2\_c} \tag{3.19}$$

$$\delta'_{sp2} = r_{bs} * (\theta'_s - \theta'_c) - r_{bp} * \theta'_{p2\_c} \tag{3.20}$$

$$\delta_{sp3} = r_{bs} * (\theta_s - \theta_c) - r_{bp} * \theta_{p3\_c} \tag{3.21}$$

$$\delta'_{sp3} = r_{bs} * (\theta'_s - \theta'_c) - r_{bp} * \theta'_{p3\_c} \tag{3.22}$$

The displacements and their derivative along the planet-ring gear meshes:

$$\delta_{rp1} = r_{bp} * \theta_{p1\_c} - r_{br} * \theta_{car} \tag{3.23}$$

$$\delta'_{rp1} = r_{bp} * \theta'_{p1\_c} - r_{br} * \theta'_{car} \tag{3.24}$$

$$\delta_{rp2} = r_{bp} * \theta_{p2\_c} - r_{br} * \theta_{car} \tag{3.25}$$

$$\delta'_{rp2} = r_{bp} * \theta'_{p2\_c} - r_{br} * \theta'_{car} \tag{3.26}$$

$$\delta_{rp3} = r_{bp} * \theta_{p3\_c} - r_{br} * \theta_{car} \tag{3.27}$$

$$\delta'_{rp3} = r_{bp} * \theta'_{p3\_c} - r_{br} * \theta'_{car} \tag{3.28}$$

3.3. Simulation

To simulate the dynamic behavior of the system, the equations of motion were derived. These were then integrated into the Simulink environment, a software within the MATLAB programming language. The advantages of this software are:

- The possibility of block-based modelling of both dynamic and non-dynamic systems;
- By varying the model parameters, we can understand how the system evolves, identify the key factors that most influence the model, and how they do so. This procedure is particularly useful both in the design phase and in the improvement phase of the model;
- Monitoring the forces involved in real-time allows us to understand which elastic or viscous components are primarily responsible for meshing, depending on the type of command given.

The main blocks of the model are described, following the mathematical model just presented, in Chapter 4.

In addition, there are several MATLAB scripts and functions that complement the Simulink model, which calculate all the quantities described so far, as well as those that follow. They can be found in the Appendix B-Matlab Script Appendix. Specifically:

- *Main HF:* It defines the main parameters of the HF model, including the parameters of the controller, the inverter, and the motor. Once the program is executed, it opens the corresponding Simulink model and starts the simulation. Additionally, it reorganizes and saves the relevant data into output structures, allowing for easy selection of the quantities of interest.

- *Dinamica riduttore:* It contains all the geometric data of the gearbox (gear ratio, shaft lengths, tooth dimensions of the gears on different shafts, etc.), the calculation of the moments of inertia, and the meshing stiffness through the call of another function called *'mesh stiffness*.' It also includes the contact segments between the teeth of the different shafts and their evolution during meshing. Additionally, it estimates the friction coefficient for this type of rotational dynamics, as described in section 3.4.2.

- *mesh stiffness:* A function that calculates the meshing stiffnesses according to the Kuang & Yang Model. [25]

- *BancoEMA_ramp0.01 and others*: There are 10 files with this name, changing only the last part, according to the specific command we are performing (ramp 0.02, 0.03, … 0.1). These scripts are used to visualize the quantities recorded during the tests, and subsequently compare them with those from the Stiffness model. They simply open CSV files, which is the format used by Siemens software to record the data obtained from the test bench, extract the variables of interest, and insert them into convenient vectors for subsequent on-screen visualization.

- *saveresultsHF:* This script simply saves the data, at the end of a simulation, into vectors, which are then plotted in MATLAB for easier visualization. In the same graph, it also plots the corresponding experimentally measured quantity, allowing for an immediate assessment of the model's effectiveness.

3.4. Energy dissipation

Losses in mechanical transmission must be considered in a accurate model. The text below explains the model that is utilized to calculate the different elements of loss in the gearbox. Power losses related to gears can be divided into two groups:

- Load-dependent losses;
- Load-independent losses

Among the load-dependent power losses, those caused by sliding between the meshing teeth are included. The friction model for this type of loss is now presented.

3.4.1. Sliding losses of the meshing teeth

It is important to recognize that the force transmitted between meshing teeth during sliding motion has two components: one perpendicular to the tooth surface and the other tangential, aligning with the relative sliding velocity. [17]

Pure rolling motion happens only at the point of contact between the pitch circles of the gears. Sliding happens above and below this point, causing a friction force between the interacting teeth known as $Fatt(t)$. The frictional force creates a torque that varies based on the position of the contact point on the line of action:

$$.F_{att}(t) = \mu * F_n(t) \tag{3.29}$$

Where:

- μ is the coefficient of friction;
- $F_n(t)$ is the force exchanged between the teeth during meshing and directed along the line of action [N];
- $F_{att}(t)$ is the tangential friction force perpendicular to the line of action [N].

The coefficient μ is assumed to remain constant during meshing. However, it is necessary to account for the change in sign with the direction of the relative sliding velocity VS:

$$\mu = \mu_0 * sign(V_s) \begin{cases} \mu_0, & V_s > 0 \\ -\mu_0, & V_s < 0 \end{cases} \tag{3.30}$$

Vibrations can be initiated by the reversal of the friction force. In straight-tooth gears, this phenomenon is very important, but it is not important in helical gears, as in our situation.

To simulate the presence of friction during meshing, the following steps were taken:

1. Estimation of the friction coefficient μ_0;
2. Calculation of the contact geometry, deriving the expressions for the curvature radii of the gears;
3. Determination of the expression for the sliding velocity of the two profiles along the contact segment;
4. Calculation of the friction torque exerted by $Fatt(t)$.

3.4.2. Estimation of the friction coefficient

Determining the friction coefficient is crucial and can be done through experimental testing or consulting the formulas in the literature. It should be emphasized that the coefficient changes during meshing depending on the movement of the contact point along the line of action and various operating parameters like contact force. In order to simplify the modelling of the system, a consistent friction coefficient is used, determined by averaging the values measured along the path of contact. Listed below are a few of the equations applied in this thesis work to calculate the Coulomb friction coefficient.

Friction coefficient with ISO/TR 14179-2

The first expression is taken from ISO/TR 14179-2 [18] and is here reported:

$$\mu_{sol-sat} = 0.048 * \left(\frac{\frac{F_{sol-sat}}{b}}{V_c * \rho_{sol-sat}} \right)^{0.2} * \eta^{-0.05} * R_{am}^{0.25} * X_L \tag{3.31}$$

With:

- V_c is the sum of the velocities at the pitch point [m/s];
- $\rho_{sol-sat}$ is the curvature radius at the pitch point [mm];
- b is the face width of the gear teeth [mm];
- $F_{sol-sat}$ is the contact force between the solar gear and the planet gear per unit length [N/mm];
- X_L is a factor related to the type of lubricant, set equal to 1 because is absent here;
- η is a coefficient similar to a dynamic viscosity at the point of contact between the rings;
- R_{am} is the arithmetic mean of the surface roughness, equal to $\frac{1}{2}(R_{a1} + R_{a2})\ [\mu m]$;

For the satellite-crown mesh the expression is the same, it changes only the $F_{sat-cor}$ force.

Friction coefficient with ISO/TR 6336-4

Another expression used is derived from the regulations ISO/TR 6336-4 [19], for the solar-satellite meshing:

.

$$\mu_{sol-sat} = 0.143 * \left(\frac{\delta * \frac{F_{sol-sat}}{b}}{V_c * \rho_{sol-sat} * \eta_d} \right)^{0.25} \tag{3.32}$$

With η_d representing the dynamic viscosity and δ the average roughness of the contact surfaces.

3.5. Gear Meshing Geometry

The point where the teeth touch is on the line that touches the base circles of the gears, called the contact line. The contact portion is determined by where the addendum circles of the two gears intersect with this line.

The line segment $s_{contact} = AB$ signifies the specific part of the interaction where the teeth actually engage in meshing. While in use, the contact point between the conjugate profiles shifts along the line of action, staying within the range marked by points A and B. [15]

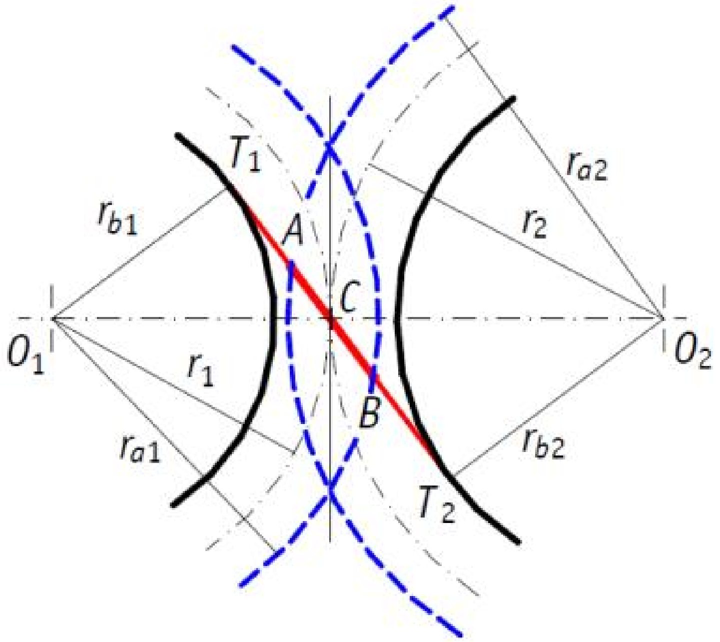

Figure 3.10: Contact segment [20]

The contact segment is divided into two parts: the first part, called the approach segment s_{acc}, extends between point A and the pitch point C. The second part is known as the recess segment s_{rec}, spanning from points C to B. Additionally, the segment from T_1 to T_2 is referred to as the base segment s_{base} corresponding to the segment $s_{base} = T_1T_2$. Looking at figure figure 3.7, we can calculate these segments as:

$$s_{acc} = \sqrt{r_{a2}^2 - r_{b2}^2} - r_{p2} * \sin(\alpha) \tag{3.33}$$

$$s_{rec} = \sqrt{r_{a1}^2 - r_{b1}^2} - r_{p1} * \sin(\alpha) \tag{3.34}$$

$$s_{base} = (r_{b1} + r_{b2}) * \tan(\alpha) \tag{3.35}$$

With:

- α is the operating pressure angle [rad];
- $r_{a1}\ and\ r_{a2}$ are the addendum radius of the driving (sun) gear and driven (planet) gear [m];
- $r_{b1}\ and\ r_{b2}$ are the base radius of the driving gear and driven gear [m];
- $r_{p1}\ and\ r_{p2}$ are the pitch radius of the driving gear and driven gear [m];

The general position of the contact point along the contact segment is identified by the angle θ_{pos}, which is the angle between the starting position θ_{pos-A} and the ending position θ_{pos-B} of the meshing between a pair of engaged teeth. From figure 3.7 we can obtain:

$$\theta_{pos-A} = \arctan\left(\frac{r_{b1}*\tan(\alpha) - s_{acc}}{r_{b1}}\right) \tag{3.36}$$

$$\theta_{pos-B} = \arctan\left(\frac{r_{b1}*\tan(\alpha) + s_{rec}}{r_{b1}}\right) \tag{3.37}$$

Once the angle θ_{pos} is defined, the expressions for the radii of curvature of the teeth for both the sun gear and the planet gear are subsequently derived, with reference to the meshing between external gears (see figure 3.8 and 3.9).

Defined also:

- ρ_{sol1} is the curvature radius of the driving gear [m];

- ρ_{sat2} is the curvature radius of the driven gear [m];

Referring to the figure 3.7 we can calculate:

$$\rho_{sol1} = T_1P = r_{b1} * \tan(\theta_{pos}) \tag{3.38}$$

$$\rho_{sat2} = T_2P = s_{base} - \rho_{sol1} \tag{3.39}$$

The radii of curvature change in an inverse relationship while the teeth pair are meshed, meaning as the contact point moves along the teeth flanks. One rises while the other falls as a result.

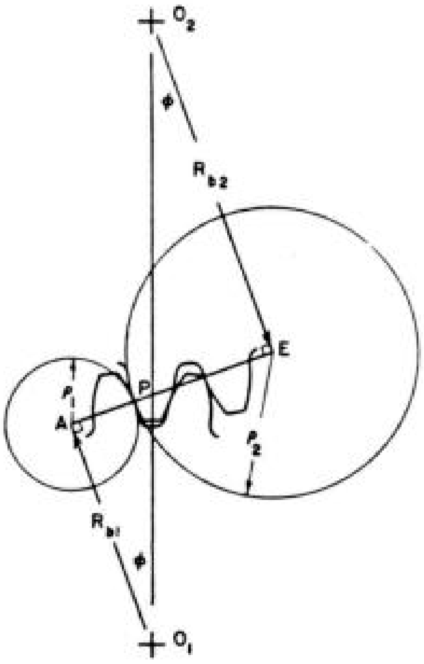

Figure 3.11: External wheel curvature radii

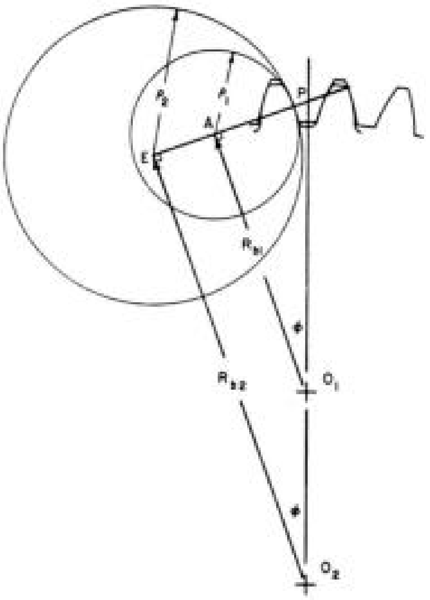

Figure 3.12: Internal wheel curvature radii

So these are the curvature radius trends plotted in Matlab. The script is provided at the end in Appendix B-Script Matlab:

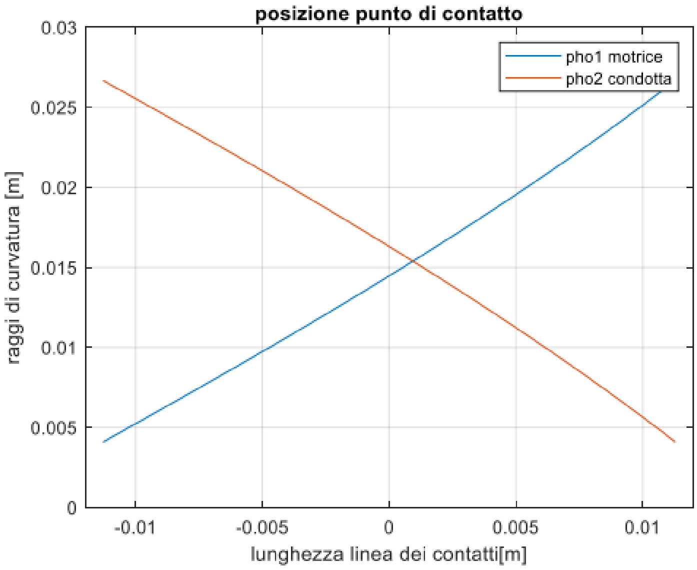

Figure 3.13: Curvature radii along the solar-satellite contact line;

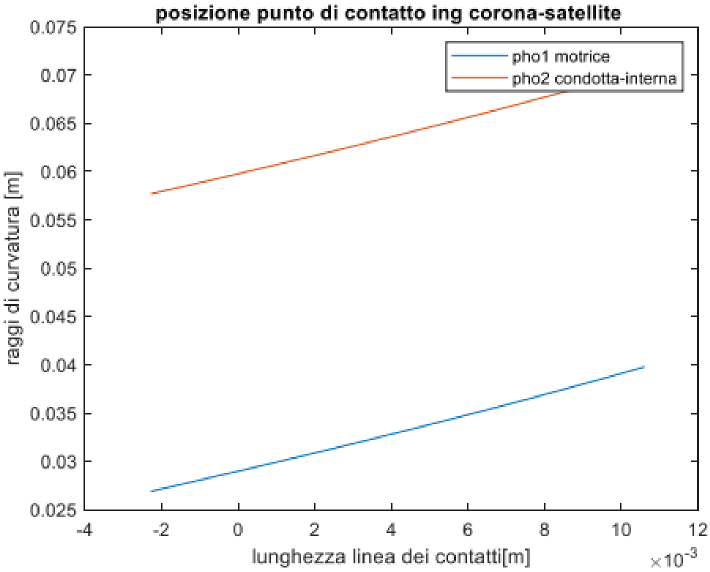

Figure 3.14: Curvature radii along the crown-satellite contact line;

3.6. Crawling speed

The illustration in Figure 3.10 depicts the gear configuration of the two wheels in our reducer. In this case, we can see the sliding velocity as the discrepancy between the tangential velocity elements of the tooth flanks where they meet.

Defining:

- w_{sol} the rotational speed of the sun gear [rad/s];
- w_{sat} the rotational speed of the i-th planet gear [rad/s];
- w_{car} the rotational speed of the carrier [rad/s];
- ρ_{sol1} and ρ_{sat2} the curvature radii of the sun gear and the planet gear, respectively, for the sun-planet meshing [m];
- ρ_{sat1} and ρ_{ring2} the curvature radii of the planet gear and the ring gear, respectively, for the ring-planet meshing [m];

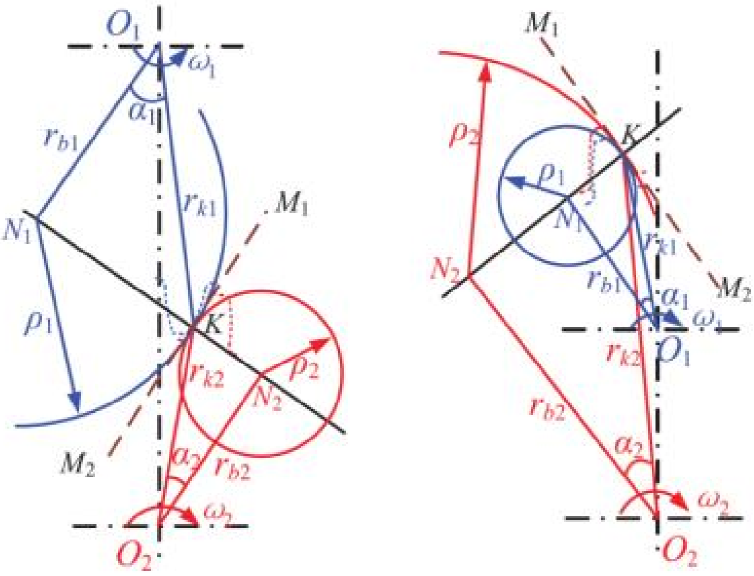

(a) (b)

Figure 3.15: Meshing between external and internal gears

The meshing phenomenon between the sun gear and the planet gears, as well as between the ring gear and the planet gears, occurs simultaneously.
Since the planet gears rotate both around their own centers and around the sun gear's axis together with the carrier, the sun-to-planet sliding velocity v_{sp} and the ring-to-planet sliding velocity v_{rp} can be expressed as follows:

$$v_{sp} = (w_{sol} - w_{car}) * \rho_{sol1} - (w_{sat} - w_{car}) * \rho_{sat2} \tag{3.40}$$

$$v_{rp} = (w_{sat} - w_{car}) * \rho_{sat1} \tag{3.41}$$

3.7. Friction pairs

Friction forces act perpendicularly to the contact forces between the tooth surfaces, generating resisting torques that depend on the shape of the gear teeth (Figure 3.11). The frictional torques vary during meshing because the lever arm of the friction force $F_{att}(t)$ changes as the contact point moves along the line of action. Friction in the sun-planet system depends on the curvature radii ρ_{sol1} and ρ_{sat2}, while in the ring gear, it depends on the curvature radii ρ_{sat1} and ρ_{ring2} for the meshing between the planets and the ring gear.

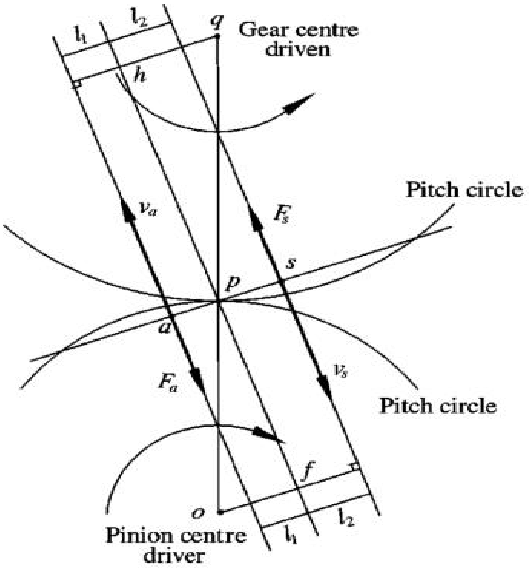

Figure 3.16: Lever arms and friction forces

The friction force varies based on the direction of the relative velocity of the teeth along the line of contact.

The presence of frictional torques affects the rotational equilibrium equations (equations 3.3-3.7) of the sun gear and the planet gears, which are then solved through integration respectively:

$$T_D - r_{bs} * (c_{sp1}\dot{\delta}_{sp1} + c_{sp2}\dot{\delta}_{sp2} + c_{sp3}\dot{\delta}_{sp3}) - r_{bs} * (k_{sp1} + k_{sp2} + k_{sp3}) - T_{att\_sp1} - T_{att\_sp2} - T_{att\_sp3} = I_{sol} * \ddot{\theta}_S \tag{3.42}$$

$$(k_{sp1} - k_{rp1}) * r_{bp} + (c_{sp1} * \delta'_{sp1} - c_{rp1} * \delta'_{rp1}) * r_{bp} - T_{att_{sp1}} - T_{att_{rp1}} = \mathrm{I}_{sat} * \ddot{\Theta}_{p1\_c} \tag{3.43}$$

$$(k_{sp2} - k_{rp2}) * r_{bp} + (c_{sp2} * \delta'_{sp2} - c_{rp2} * \delta'_{rp2}) * r_{bp} - T_{att_{sp2}} - T_{att_{rp2}} = \mathrm{I}_{sat} * \ddot{\Theta}_{p2\_c} \tag{3.44}$$

$$(k_{sp3} - k_{rp3}) * r_{bp} + (c_{sp3} * \delta'_{sp3} - c_{rp3} * \delta'_{rp3}) * r_{bp} - T_{att_{sp3}} - T_{att_{rp3}} = \mathrm{I}_{sat} * \ddot{\Theta}_{p3\_c} \tag{3.45}$$

The friction pairs can be calculated as follows, considering the friction forces described in section 3.4.1:

$$T_{att\_sp} = (\mu_{sol-sat} * F_{sp} * sign(V_{sp}) * \rho_{sol1} \tag{3.46}$$

$$T_{att\_rp} = (\mu_{ring-sat} * F_{rp} * sign(V_{rp}) * \rho_{sat1} \tag{3.47}$$

3.8. Gear meshing stiffnesses

Meshing stiffness indicates the relationship between the tangential force along a line of action and the deflection of the tooth in the same direction. It is defined as the force required to deform a single tooth with a width of 1 meter by 1 meter along the line of action ([N/m/m]). Since the applied force on a tooth varies in intensity, direction, and point of application, the tooth deflection continually changes. Therefore, the variability of the meshing stiffness is influenced by both the variability of the tangential force (intensity, direction, and sense) and the change in the number of engaged teeth (degree of coverage) during meshing. [24]

Figure 3.13 shows the steps to calculate the meshing stiffness for a planetary gearbox. Since there are multiple planet-sun and planet-ring gear pairs, the stiffness of each pair is assessed experimentally.

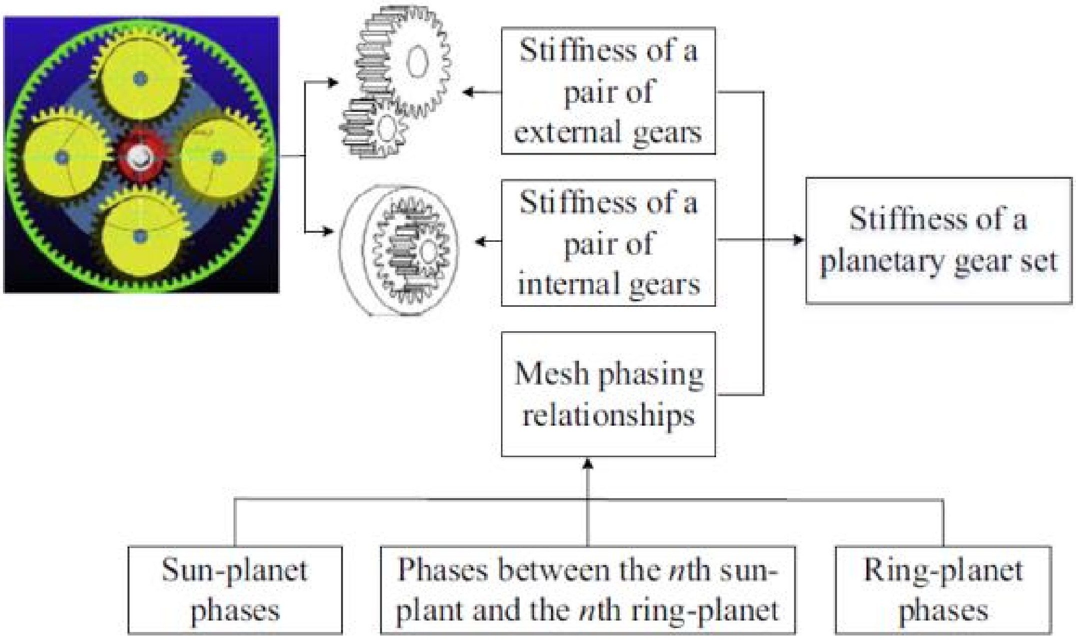

Figure 3.17: Mesh stiffness evaluation graph

Following a finite element analysis, J. H. Kuang and Y. T. Yang developed an analytical model for calculating mesh stiffness [25]. Their model represents the stiffness of a single tooth, which is conceptualized as a cantilever beam. Specifically, equation 3.44 expresses the variability of stiffness as a function of the contact point position, its displacement, and other parameters. This approach allows for the exact determination of stiffness along the entire path of action, i.e., throughout the meshing process, from the initial contact between gear teeth to their separation. The stiffness of a single tooth $K_i(r_i)$ as a function of the radial distance r_i from the gear axis as well as the Kuang and Yang's empirical equation is:

$$K_i(r_i) = 10^9 * [(A_0 + A_1 * x_i) + (A_2 + A_3 * x_i) * \frac{x_i - R_i}{(1+x_i)*m}] \tag{3.48}$$

Where the experimental coefficients are:

- $A_0 = 3.867 + 1.612 * Z_i - 0.02916 * Z_i^2 + 0.0001553 * Z_i^3;$
- $A_1 = 17.060 + 0.7289 * Z_i - 0.01728 * Z_i^2 + 0.00009993 * Z_i^3;$
- $A_2 = 2.637 - 1.222 * Z_i + 0.02217 * Z_i^2 - 0.0001179 * Z_i^3;$
- $3A_3 = -6.330 - 1.033 * Z_i + 0.02068 * Z_i^2 - 0.0001130 * Z_i^3;$

m is the module of the gear [m], x_i is the correction factor of the i-th gear, equal to the ratio between the displacement v of the cutting line from the reference line and the module m, $x_i = \frac{v_i}{m}$, Z_i the number of teeth of the i-th gear and R_i is the pitch radius of the i-th gear [m];"

According to what was previously stated in the physical model described in paragraph 3.1, when two teeth are meshing, there are two constants, K_1 and K_2, which are arranged in series. The stiffness of a single pair of meshing teeth is the single stiffness equivalent to the stiffness values arranged in series. So $K_{equivalent}$ will be:

$$K_{eq} = \frac{K_1(r_1)*K_2(r_2)}{K_1(r_1)+K_2(r_2)} \tag{3.49}$$

Considering 4 contact points:

A. Point of engagement initiation;

B. Point of engagement initiation for a single pair of teeth;

C. Point of disengagement for a single pair of teeth;

D. Point of disengagement.

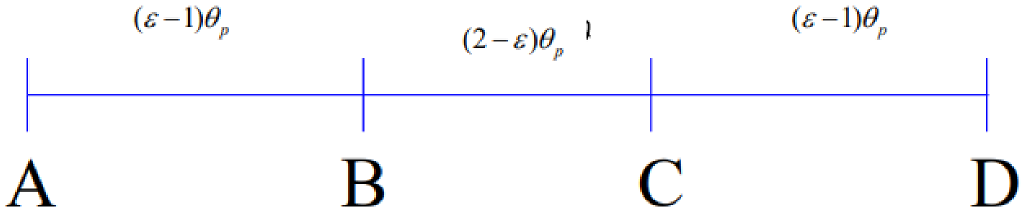

Figure 3.18: Contact segment ($\theta_p = {}^{2\pi}/_{z}$, angular pitch)

If $\varepsilon = 1$ (contact ratio), there would always be a single pair of teeth in mesh, and the meshing stiffness K_{tot} would coincide with the stiffness of the individual pair K_{eq}, but this is a limiting case. Typically, ε is between 1 and 2, meaning that during meshing, the system cyclically transitions between having one and two pairs of teeth in contact. Consider a generic gear system with two pairs of teeth: pair A consists of teeth 1 and 2, and pair B consists of teeth 3 and 4. Teeth 1 and 3 belong to the driving gear, while teeth 2 and 4 belong to the driven gear, as shown in Figure 3.17.

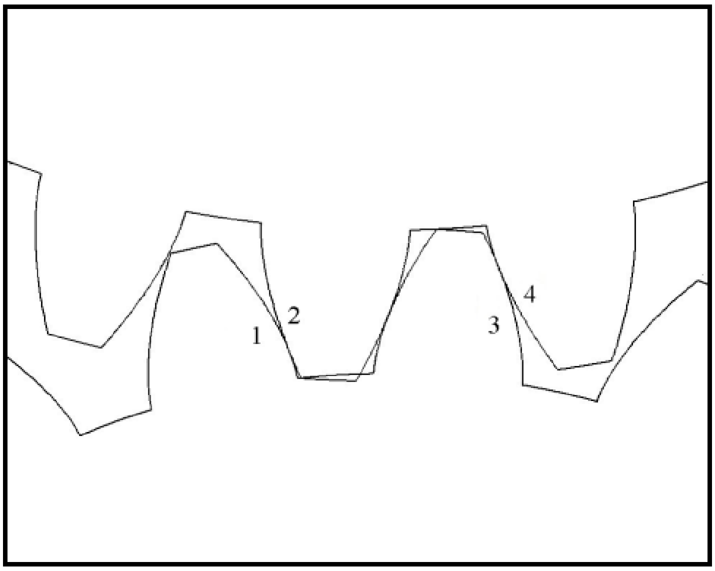

Figure 3.19: 2 Pairs of teeth in mesh

In the initial phase, tooth 1 begins to engage with its corresponding tooth on the other gear, while tooth 3, which precedes it by one pitch, traverses the final section of its engagement path, between points C and D. When pair A starts to travel along segment B-C, pair B has already disengaged, while the subsequent pair of teeth has not yet begun to engage.

During the central phase of engagement (segment B-C), only one pair is loaded, and therefore, the engagement stiffness coincides with the stiffness of pair A, denoted as K_S^A. In contrast, during the initial and final segments, two pairs are engaged, resulting in a situation analogous to two springs arranged in parallel. Thus, in this case, K_M is equal to the sum of the stiffnesses of the engaged pairs, K_S^A and K_S^B

The stiffnesses of the two engaged pairs are:

$$K_S^A = \frac{K_1^A(r_1^A) * K_2^A(r_2^A)}{K_1^A(r_1^A) + K_2^A(r_2^A)} \tag{3.50}$$

$$K_S^B = \frac{K_1^B(r_1^B) * K_2^B(r_2^B)}{K_1^B(r_1^B) + K_2^B(r_2^B)} \tag{3.51}$$

While K_M:

- $K_M = K_S^A$ if there is only one engaged pair, that is, when traversing segment B-C;
- $K_M = K_S^A + K_S^B$ if there are two engaged pairs, specifically along segments A-B and C-D.

3.9. Phase differences in planets gear meshing

Multiple tooth engagements in epicyclic gear systems involve a variable number of teeth in contact, operating at the same meshing frequency, referred to as $fmesh$. All sun-planet gear engagements exhibit the same pattern and periodicity in the variation of the number of teeth in contact, but these variations are generally not synchronized. This means there is a phase shift between the number of teeth in contact across the different gear engagements. The same phenomenon occurs with the ring-planet engagements. Additionally, a phase difference must also be considered between the sun-planet and ring-planet gear engagements [25].

The phase shifts between the different planets are:

- γ_{sn} is the relative phase shift between the engagement of the n-th sun-planet pair and that of the first sun-planet pair;

- γ_{rn} is the relative phase shift between the engagement of the n-th ring-planet pair and that of the first ring-planet pair;

- γ_{sr} is the relative phase shift between the engagement of the n-th sun-planet pair and the n-th ring-planet pair.

To determine γsn, we can imagine fixing the sun gear. After a complete rotation of the carrier, the first planet will have made a full 2π rotation around the sun's axis, coming into contact with all the sun's teeth. Consequently, with a carrier rotation ψ_n the same planet will mesh with a number of sun teeth equal to $z_{sol} * {}^{\psi_n}\!/_{2\pi}$. A similar reasoning applies to the determination of γ_{rn}.
Thus, the phase shifts between the planets are derived using the following relations:

$$\gamma_{sn} = \frac{z_{sol}*\psi_n}{2\pi} \quad \text{and} \quad \gamma_{rn} = -\frac{z_{ring}*\psi_n}{2\pi} \quad \text{with clockwise rotation of the planets} \tag{3.52}$$

If the rotation were counterclockwise, the signs would be reversed. Additionally:

$$\psi_n = p_n \frac{2\pi}{z_{sol}*z_{ring}} \tag{3.53}$$

With ψ_n the rotation angle of the carrier required to bring the first planet into the initial position of the n-th planet.
To calculate γ_{sr} the procedure described by R.G. Parker was followed [26]:

$$\gamma_{sr} = \frac{P_{m\_ring} C_{ring\_planet}}{p_{base}} \tag{3.54}$$

Where:

- P_{m_ring} is the point on the contact line segment of the ring gear-planet gear mesh, corresponding to the moment when the contact point for the sun-planet gear mesh coincides with the instantaneous center of rotation.

- C_{ring_planet} is the instantaneous center of rotation for the ring gear-planet gear contact.

Using a form of the meshing stiffness (3.48) expressed through a Fourier series [27], which accounts for the phase shifts just described, we can write the 6 time-varying meshing stiffness values: 3 for the sun-planet meshing and 3 for the planet-ring meshing:

$$K_{sp1}(t) = K_{sp} + \frac{K_{sp}}{\pi} * \sin\big(\omega_m(t - T_m * \gamma_{s1})\big) + \frac{K_{sp}}{3\pi} * \sin\big(3\omega_m(t - T_m * \gamma_{s1})\big) + \frac{K_{sp}}{5\pi} * \sin\big(5\omega_m(t - T_m * \gamma_{s1})\big) \tag{3.55}$$

$$K_{sp2}(t) = K_{sp} + \frac{K_{sp}}{\pi} * \sin\big(\omega_m(t - T_m * \gamma_{s2})\big) + \frac{K_{sp}}{3\pi} * \sin\big(3\omega_m(t - T_m * \gamma_{s2})\big) + \frac{K_{sp}}{5\pi} * \sin\big(5\omega_m(t - T_m * \gamma_{s2})\big) \tag{3.56}$$

$$K_{sp3} = K_{sp} + \frac{K_{sp}}{\pi} * \sin\big(\omega_m(t - T_m * \gamma_{s3})\big) + \frac{K_{sp}}{3\pi} * \sin\big(3\omega_m(t - T_m * \gamma_{s3})\big) + \frac{K_{sp}}{5\pi} * \sin\big(5\omega_m(t - T_m * \gamma_{s3})\big) \tag{3.57}$$

$$K_{rp1} = K_{rp} + \frac{K_{rp}}{\pi} * \sin\big(\omega_m(t - T_m * (\gamma_{r1} + \gamma_{rs})\big) + \frac{K_{rp}}{3\pi} * \sin\big(3\omega_m(t - T_m * (\gamma_{r1} + \gamma_{rs}))\big) + \frac{K_{rp}}{5\pi} * \sin\big(5\omega_m(t - T_m * (\gamma_{r1} + \gamma_{rs}))\big) \tag{3.58}$$

$$K_{rp2} = K_{rp} + \frac{K_{rp}}{\pi} * \sin\big(\omega_m(t - T_m * (\gamma_{r2} + \gamma_{rs})\big) + \frac{K_{rp}}{3\pi} * \sin\big(3\omega_m(t - T_m * (\gamma_{r2} + \gamma_{rs}))\big) + \frac{K_{rp}}{5\pi} * \sin\big(5\omega_m(t - T_m * (\gamma_{r2} + \gamma_{rs}))\big) \tag{3.59}$$

$$K_{rp3} = K_{rp} + \frac{K_{rp}}{\pi} * \sin\big(\omega_m(t - T_m * (\gamma_{r3} + \gamma_{rs})\big) + \frac{K_{rp}}{3\pi} * \sin\big(3\omega_m(t - T_m * (\gamma_{r3} + \gamma_{rs}))\big) + \frac{K_{rp}}{5\pi} * \sin\big(5\omega_m(t - T_m * (\gamma_{r3} + \gamma_{rs}))\big) \tag{3.60}$$

With:

- ω_m is the meshing rotation speed. ($\omega_m = 2\pi * f_m$);
- f_m is the meshing frequency given by $f_m = f_{sol} * \frac{z_{sol} * z_{ring}}{z_{sol} + z_{ring}}$;
- T_m is the meshing period ($T_m = {}^{1}\!/_{f_m}$).

Additionally, a constant stiffness value K_{sp} and K_{rp} was used as an initial value, without accounting for the variation in stiffness as a function of the load applied on the tooth, nor the change in the number of teeth in contact during meshing.

$$k_{sp} = (0.75 * \varepsilon + 0.25) * k_c * b_s \tag{3.61}$$

$$k_{rp} = (0.75 * \varepsilon + 0.25) * k_c * b_r \tag{3.62}$$

Having:

- k_c is the stiffness of a pair meshing teeth;
- ε is the contact ratio;
- b_s is the face width of the sun gear;
- b_r is the face width of the ring gear.

The stiffness has been expressed as a function of time because, although the formulation based on angular position is more accurate, it is more convenient to express it in relation to the time during which the dynamics of the epicyclic gear train evolve. It should also be noted that the Fourier series is merely a sum of harmonics with frequencies equal to the meshing frequency f_m of the tooth and its multiples.
As an example, the stiffness values calculated for the minimum command meshing, specifically at 0.01 rad/s, are reported in figures:

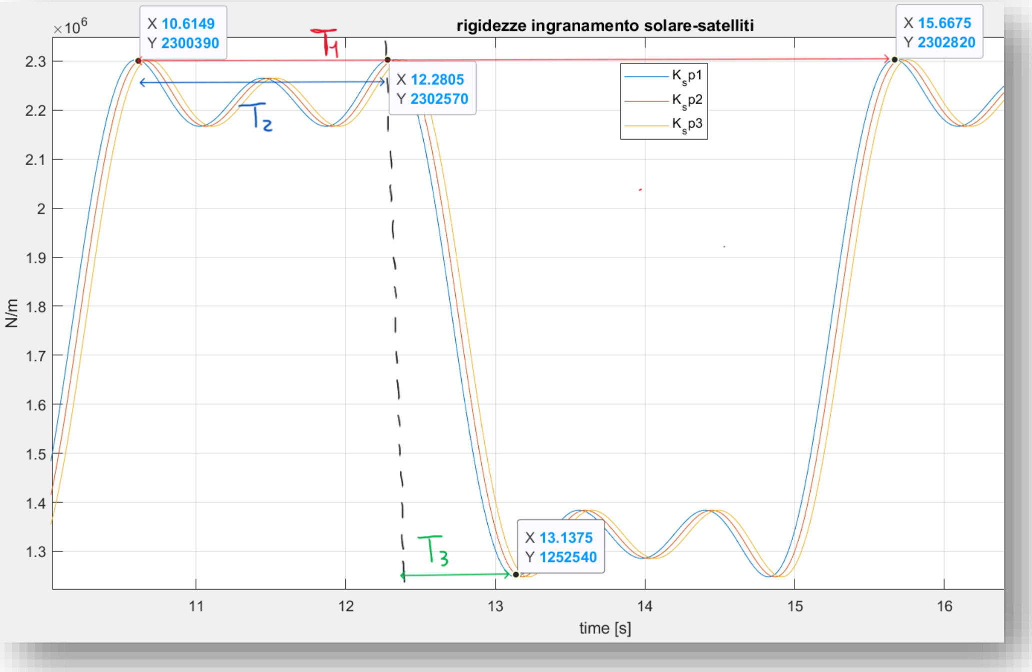

Figure 3.20: Trend of mesh stiffness between sun gear and planets.

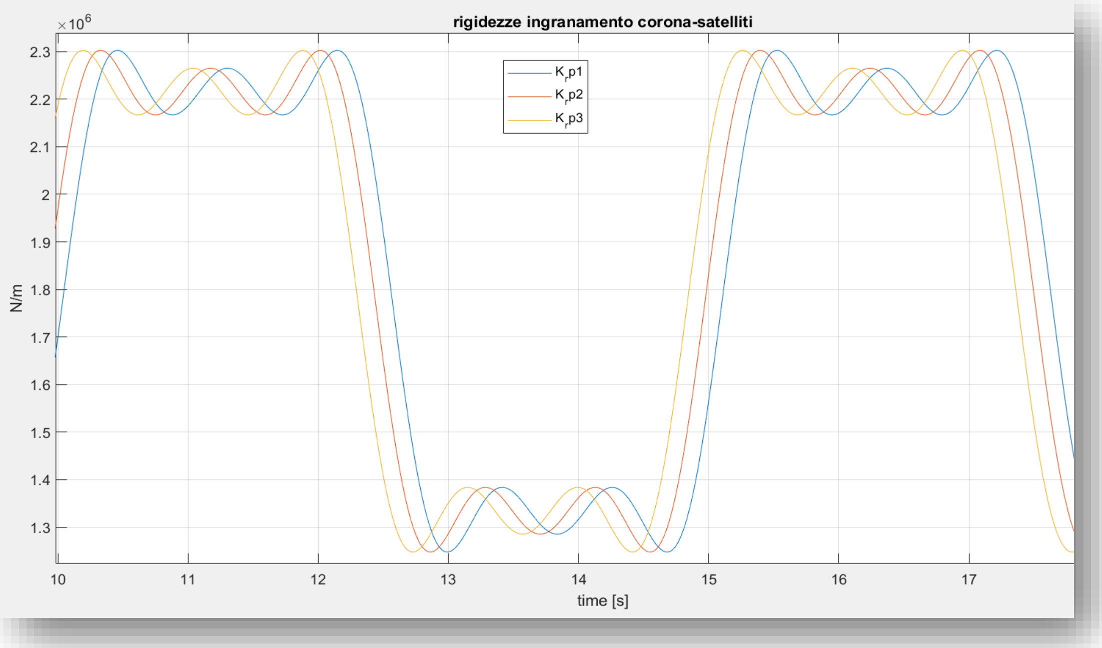

Figure 3.21: Trend of mesh stiffness between crown and planets

The highest stiffness values represent the meshing between two pairs of teeth, while the lowest values correspond to the meshing between a single pair. It is also observed that there is a phase shift among the three planets during meshing with both the sun gear and the ring gear; thus, the stiffness values K_{sp} and K_{rp} exhibit the same trends but are shifted by a certain Δt.

Now, let’s analyze a specific test, for instance, the command value of 0.01 rad/s, and make some considerations regarding the stiffness that apply to any command.

The period of the stiffness for this command is approximately 0.3 s and, by analyzing Figures 3.17 and 3.18, we can observe intervals of time in which all values are at their maxima, all at their minima, and intervals where they cross each other.

If we analyze the factors contributing to the stiffness, we have 3 characteristic contributions with their own periods:

$$k_{xy}(t) = k_{xy} + a \cdot \sin\big(w_m(t - \cdots)\big) + b \cdot \sin\big(3w_m(t-..)\big) + c \cdot \sin\Big(5\big(w_m(t - \cdots)\big)\Big) \tag{3.63}$$

With a, b, c numerical coefficient.

We have 3 periods:

- $T_1 = \frac{2\pi}{|w|} = \frac{2\pi}{w_m} = 4{,}98\ s$;
- $T_2 = \frac{2\pi}{|w|} = \frac{2\pi}{3w_m} = 1{,}66\ s$;
- $T_3 = \frac{2\pi}{|w|} = \frac{2\pi}{5w_m} = 0{,}99\ s$

Since all three periods are rationally related, the resulting function will be periodic. The overall period of the function will be the minimum common multiple (m.c.m.) of the three periods, which in this case is:

$$T_{tot} = m.c.m.(4.98, 1.66, 0.99) \cong 5 \text{ s}$$

In reality, since the periods are not perfectly rationally related but approximated, the function will not be perfectly periodic and regular. It will exhibit irregular segments and quasi-periodicity.

We observe this in the behavior of the current flowing through the rotor windings of the electric motor. In fact, as shown in Figure 3.19, the current behavior measured during the first test, corresponding to the first command of 0.01 rad/s, displays a clear periodicity of 5s seconds between current peaks. This corresponds to the meshing periodicity between two gears.

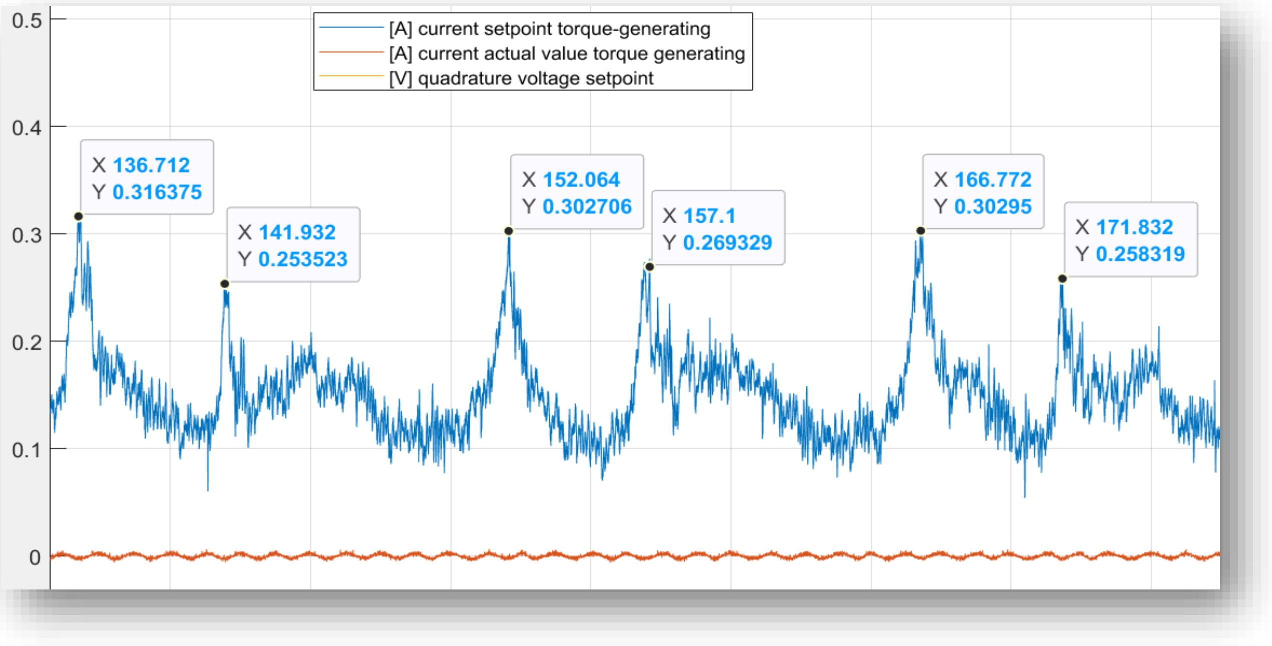

Figure 3.22: Current behavior periodicity in the motor.

The second and third periods T_2 and T_3 are less visible when observing the current due to disturbances and noise. They correspond respectively to the first period $T_2 = 1{,}66s$ during which the stiffness reaches its maximum value (indicating two pairs of teeth in mesh, see Figure 3.17), and the second period $T_3 = 0{,}99s$ which represents the time interval during which the gear transitions from two pairs of teeth in mesh to one.

The current peaks occur for two main reasons: either because at those points there is engagement between a single pair of teeth, necessitating more effort from the motor to complete the meshing, which leads the inverter to send a higher power signal to compensate for this deficiency; or because, after nnn meshing cycles involving multiple teeth, the phase difference between the solar-planet meshing and the corresponding planet-ring meshing is detected. Locally, there will be a brief current spike due to the fact that the tooth is essentially commanded to engage but does not immediately find the corresponding tooth of the other gear to mesh with.

All these considerations have been presented for a single command but apply to all other commands discussed in this work, as outlined in Chapter 5.

4. Simulink model

After describing the phenomenon from a mathematical and physical perspective, the corresponding block model has been developed in Simulink. Each block represents the realization of the mathematical equations outlined in the previous chapter.

Inside the Mechanical transmission model, which was one of the main block of the High Fidelity system, has been developed the friction model below.

The entire friction model consists of 7 main blocks, each containing sub-blocks. The figure presents a schematic representation with the blocks numbered to facilitate their description.

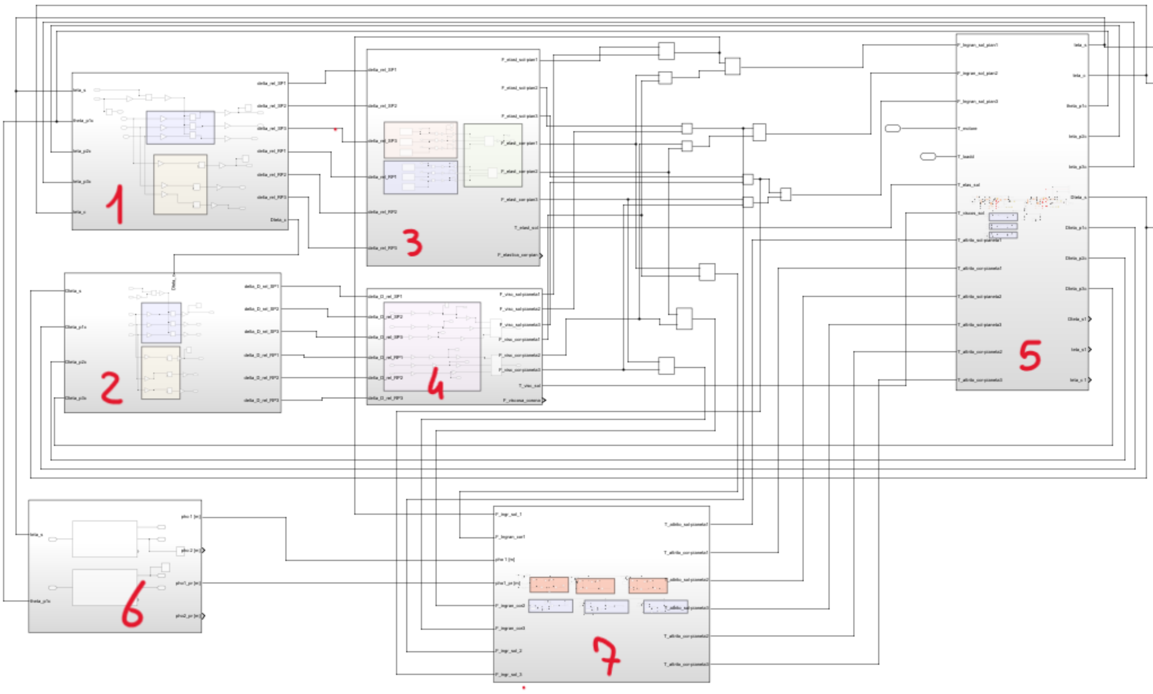

Figure 4.1: Simluink Friction model blocks

4.1. Block 1 and 2: Relative displacements and their derivatives

Block 1 and block 2 represents the mathematical formulation described in the paragraph 3.2.3. and the implementation of the equations 3.17 to 3.28, i.e., the relative displacements along the line of action between sun and planet gears and their derivates.

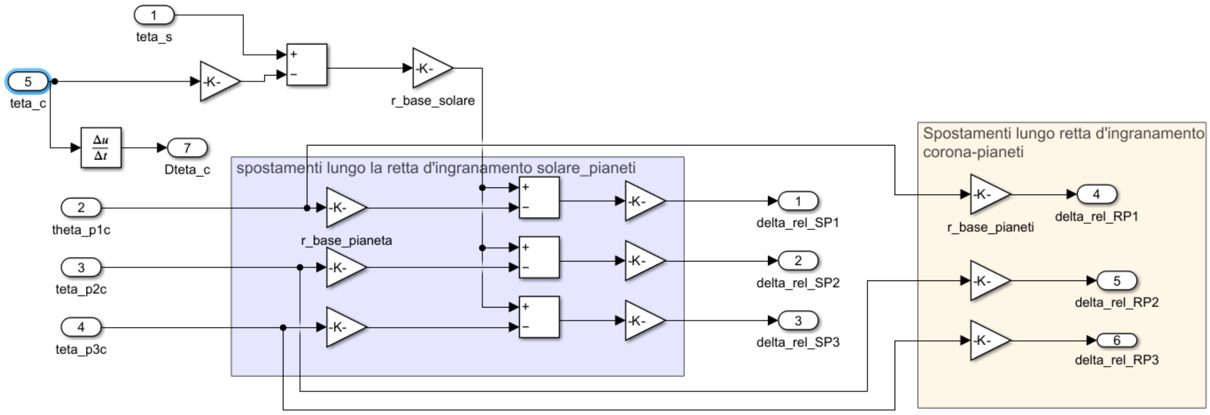

Figure 4.2: Relative elastic displacements

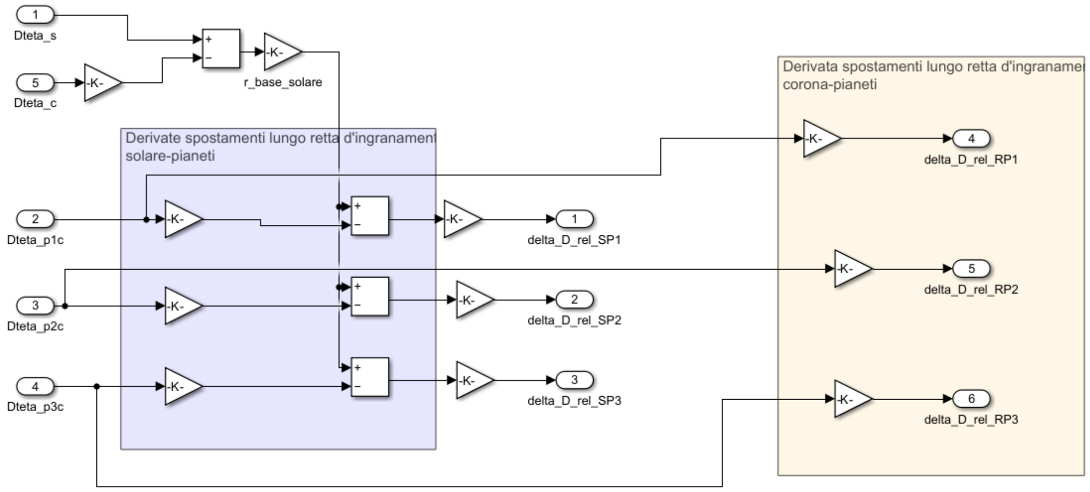

Figure 4.3: Relative elastic displacements derivates

4.2. Block 3: Gear mesh elastic forces

This block calculates the elastic forces exchanged between two meshing teeth; specifically, equations 3.9 to 3.12 described in the previous chapter. The inputs are the relative displacements previously calculated and the gear mesh stiffnesses, expressed according to the model [27] and described in paragraph 3.9. The block outputs the torque exerted by the elastic actions between the sun-planet and planet-ring gear meshes, obtained by multiplying the elastic forces by the radius of the gear to which they refer.

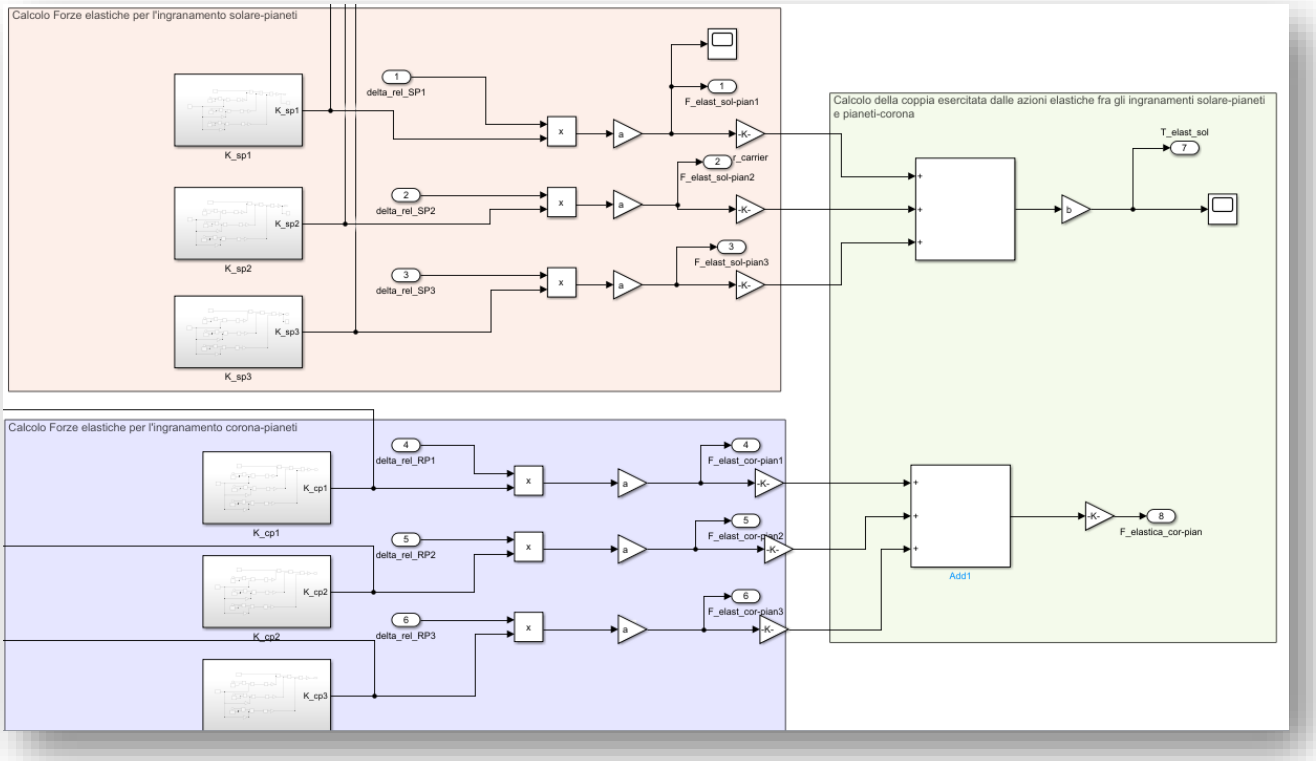

Figure 4.4: Elastic torque between the sun-planet and planet-ring gear meshes

4.3. Block 4: Gear mesh viscous forces

As the previous one, this block calculate the viscous forces exchanged during the meshing, as described in paragraph 3.2.3. It represents the equations 3.13 to 3.16, and, like the previous block, takes as input the relative displacement velocities and the viscous damping coefficients. It outputs both the viscous forces and torques acting in the gear meshes.

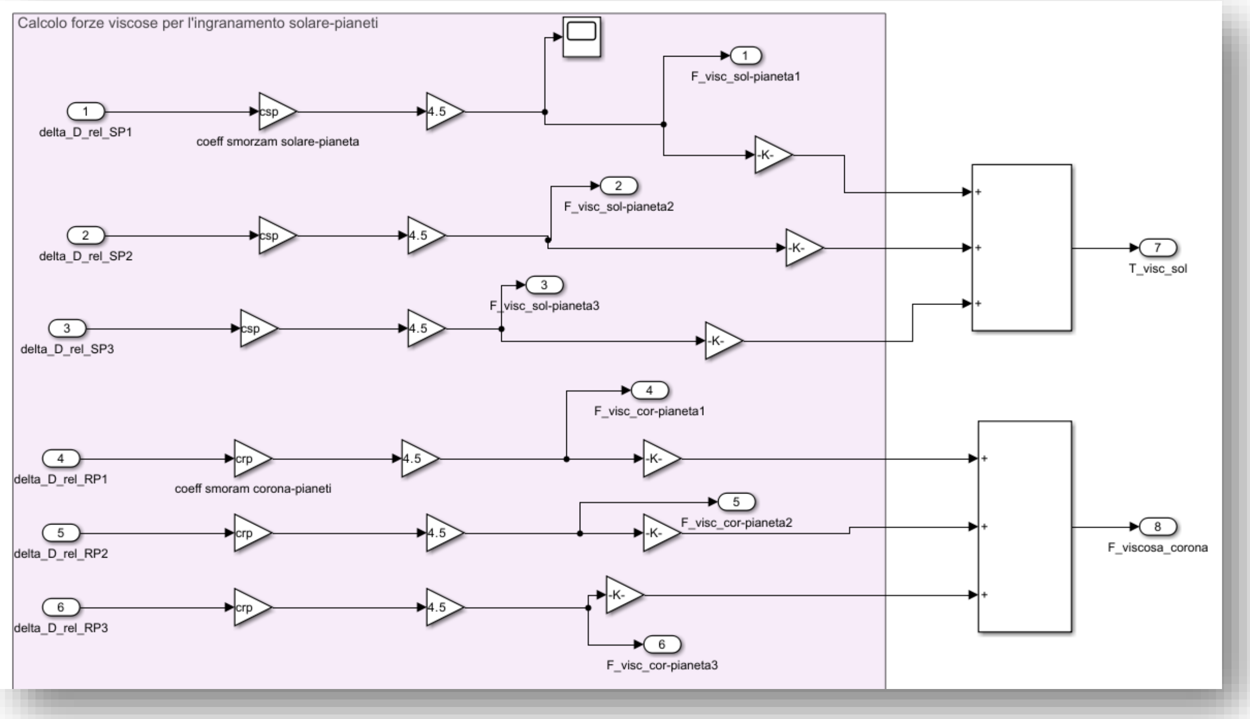

Figure 4.5: Viscous torque between the sun-planet and planet-ring gear meshes

4.4. Block 5: Equations of motion

This block contains the equations of rotational equilibrium for the sun gear and the three satellites, as described in Chapter 3. In particular, Equation 3.42 is presented in figure 4.6 while equations 3.43 to 3.45 in figure 4.7.

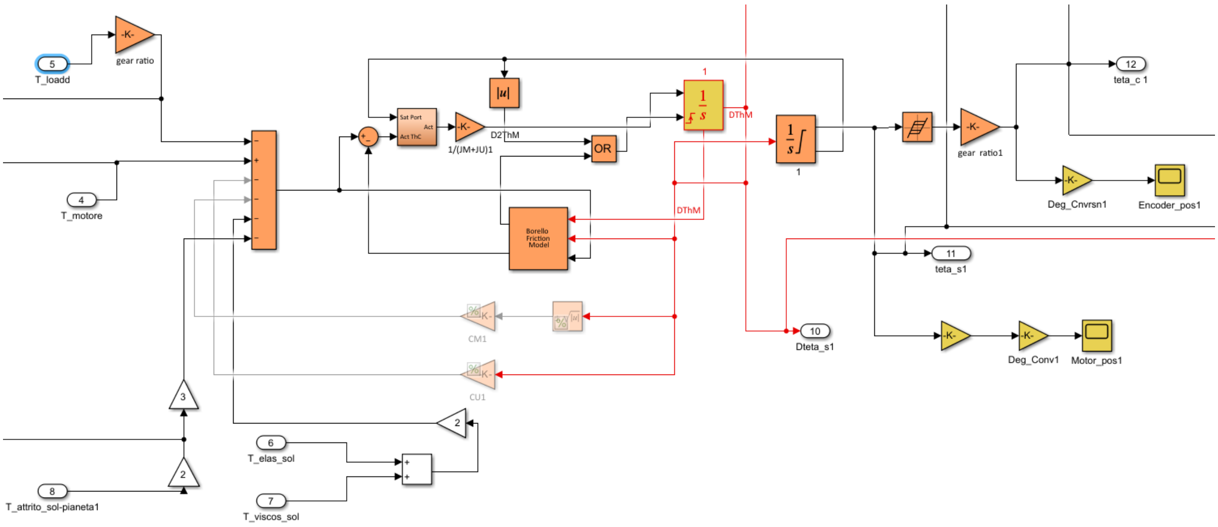

Figure 4.6: Equation of equilibrium for the sun gear

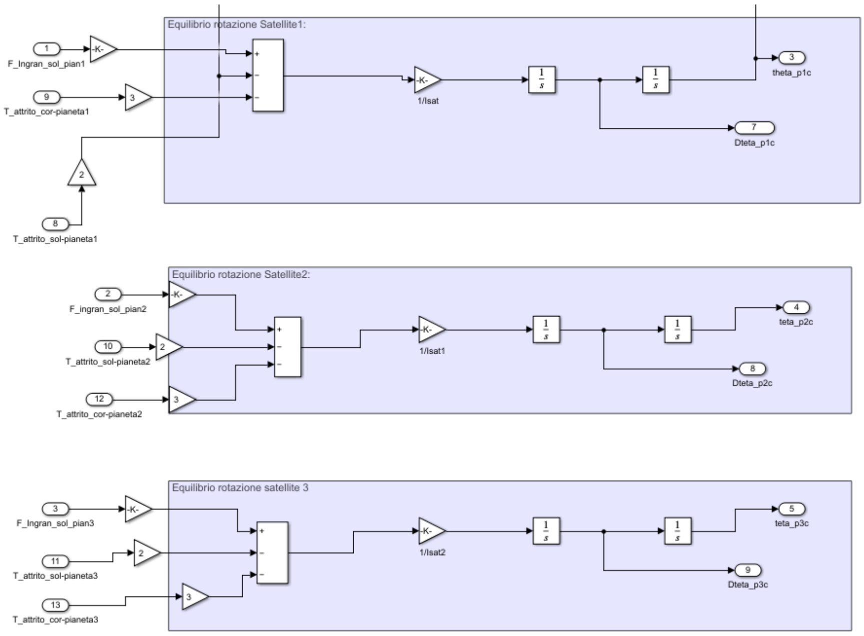

Figure 4.7: Equation of equilibrium for the satellites

It is immediately apparent that the model for the equation of the sun gear is more developed than those for the satellites. This is because our primary interest lies in studying the angular position and velocity of the sun gear rather than that of the satellites. In fact, the behavior of the sun gear governs the other equations; therefore, a more detailed model was created solely for this equation to avoid overloading the simulation environment.

It can be observed that the equilibrium equation for the sun gear includes the 'Borello friction model' block for the static friction of the gear, as well as the torques that are added and subtracted to obtain the angular velocity and position of the motor shaft through integration blocks. Initially, this equation also included a contribution that accounted for the dimensional viscous damping coefficient of the DC motor and the load; however, it was removed (or rather, modified) due to numerical issues. This factor, when directly multiplied by the rotational speed of the shaft, was subtracted from the other driving and resisting torques acting on the shaft. During the validation of this model, this led to numerical instability in the computational process, specifically within the integration block.
This instability occurred because the speed, at the initial time intervals, reached values higher than those commanded, resulting in a resistive contribution that was greater than the actual value, which inverted the physics of the model (resistive contributions greater than the driving ones, causing the sun gear to hypothetically rotate in the opposite direction).

To avoid this issue, the subtractive contribution due to the dimensional viscous damping of the DC motor and the load has been transferred directly into the elastic and viscous torques, through a multiplicative coefficient that reduces the torques by the same amount obtained from the product of the damping coefficient CM (or CU) and the velocity w_m, with CM dimensional viscous damping coefficient of the DC motor (CU respectively the load) and w_m the steady-state velocity of the motor.

As output, we obtain, in addition to the angular velocity of the motor shaft, the corrected angular position, taking into account the forces and frictions exchanged between the gear trains, and consequently, the angular position of the load, which represents the final user's position.

4.5. Block 6: Curvature radii of friction

We have seen that the contact between the teeth occurs along the tangent line to the two base circles, within a portion of it referred to as the contact segment. This block performs the calculation of these segments, as described in Chapter 3.5, both for the driving gear (pho1) and for the driven gear (pho2).

pho1_pr and pho2_pr refers instead to the curvature radii of a planet gear and the ring gear, respectively.

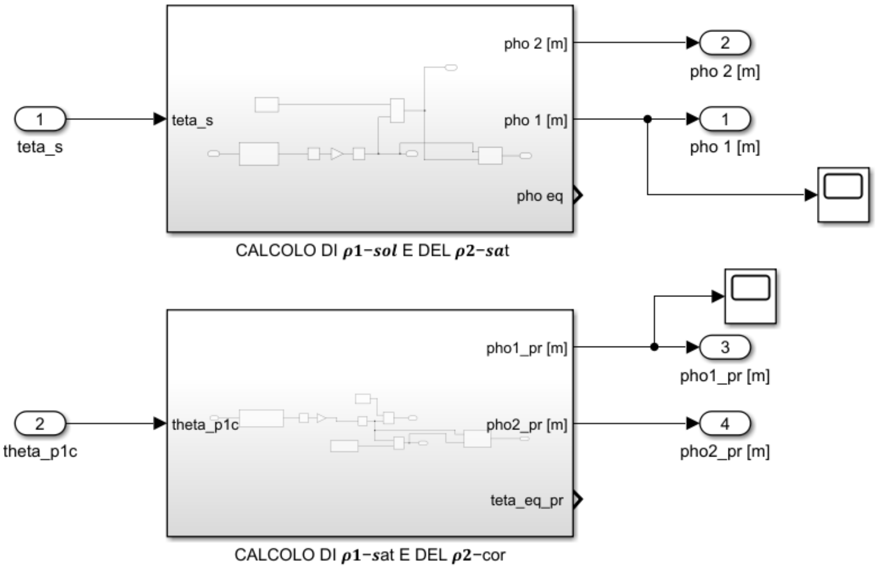

Figure 4.8: Calculation of friction curvature radii

The calculation of the curvature radii is essential for the validation of the model, as the friction forces exchanged during meshing vary their distance from the axis of rotation of the shafts, since they act along the contact segment. Consequently, the torque exerted by friction during meshing will also vary.

These curvature radii, along with the engagement forces from blocks 3 and 4, serve as inputs to block 7, which then calculates the corresponding friction torques.

4.6. Block 7: Calculation of friction losses for gearing

Having calculated all the components required by equations 3.46 and 3.47, this block computes the dissipative friction forces for each gear engagement. The friction coefficients, according to ISO/TR 14179-2 and 6336-4 [18], as described in paragraph 3.4.2, are labeled in the model as *f_att_average* for sun-planet gears and *f_att_average_r* for planet-ring gears, and are calculated in the *dinamica_riduttore* Matlab script.

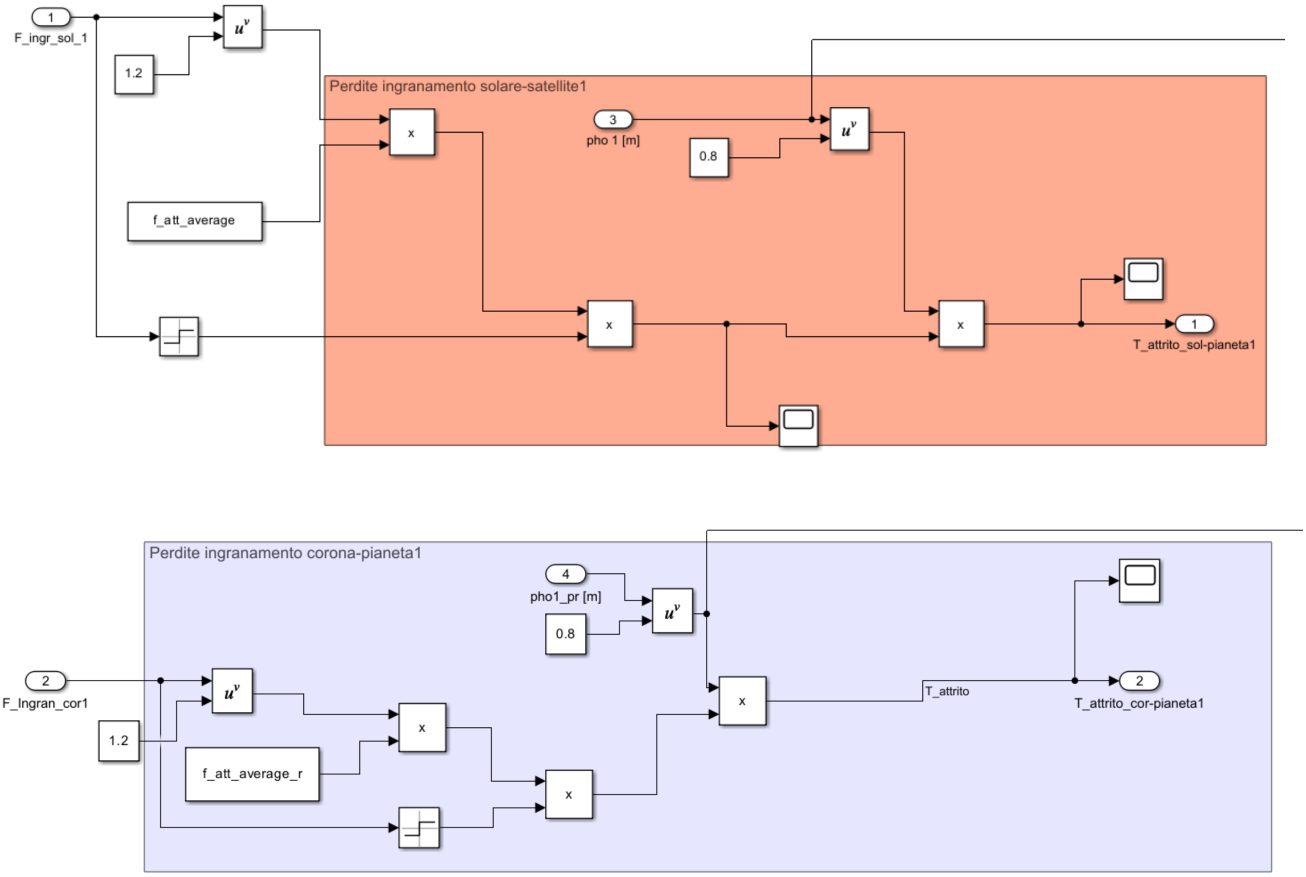

Figure 4.9: Frictional torque losses in gear engagements

This block outputs all the frictional torques T_{att_sp1}, T_{att_sp2}, T_{att_sp3}, T_{att_rp1}, T_{att_rp2}, T_{att_rp3}, which are then fed into block 5, i.e., into the equations of motion corrected by this model, as well as the equations 3.42 to 3.45.

5. Comparison and final results

After describing the Simulink model created for the examined gearbox system, this chapter presents the final simulation results.
All ramp commands estimated at the beginning of the project were executed to better evaluate the actuation of a secondary flight control command. The graphs plot the angular position of the motor and that of the encoder, compared with the experimental data recorded by the sensors during the tests.

In the first 5 commands, only the angular positions of the friction model were plotted and compared with the experimental results, whereas for the last 5 commands, both models were compared (HF and HF Friction).
This is because the friction model is more noticeable in low ramp commands, as the forces exchanged by the gears are much closer in magnitude to the friction forces, resulting in a more visually significant impact on the graph. In contrast, with larger commands, the effect of friction is less dominant.
(In thi
Here the results for each command:
(In the interpretation of the following figures, 'HF' refers to the newly developed friction model described here, not the previous model).

1. Ramp command 0.01 rad/s

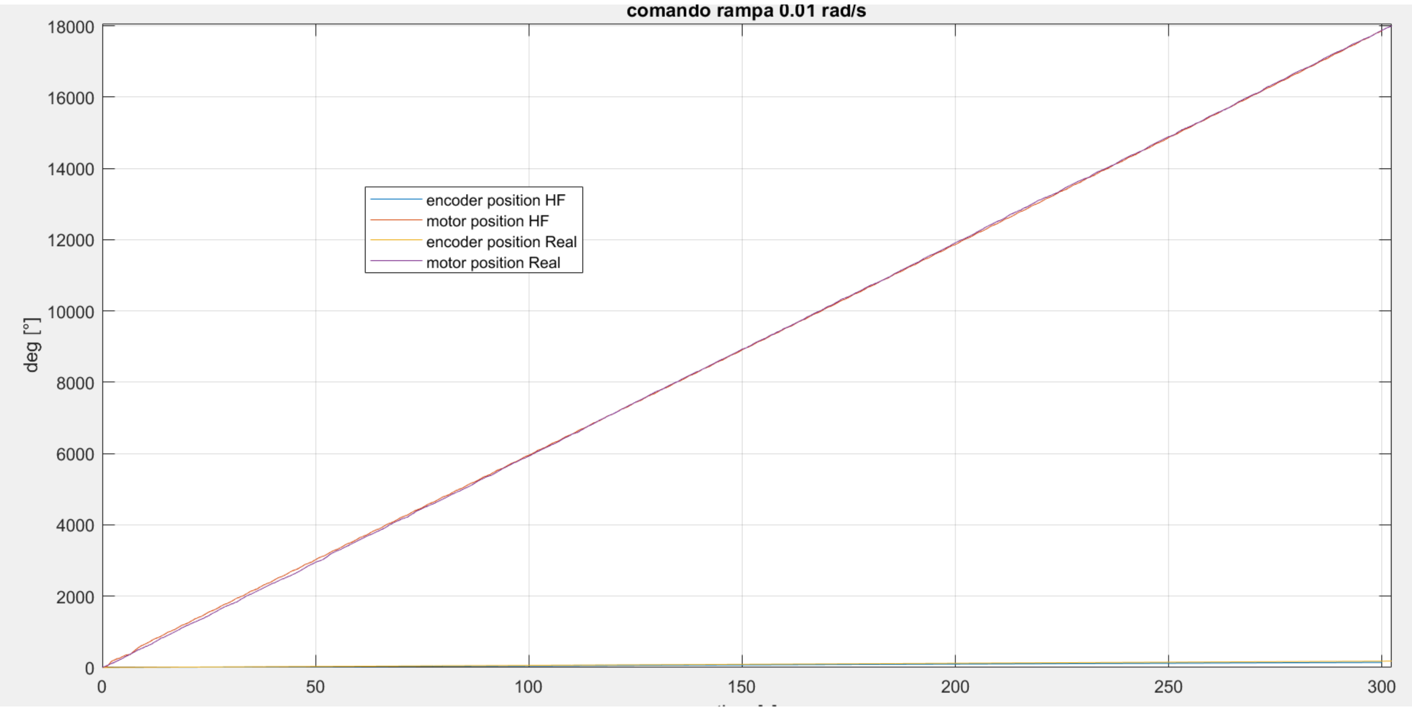

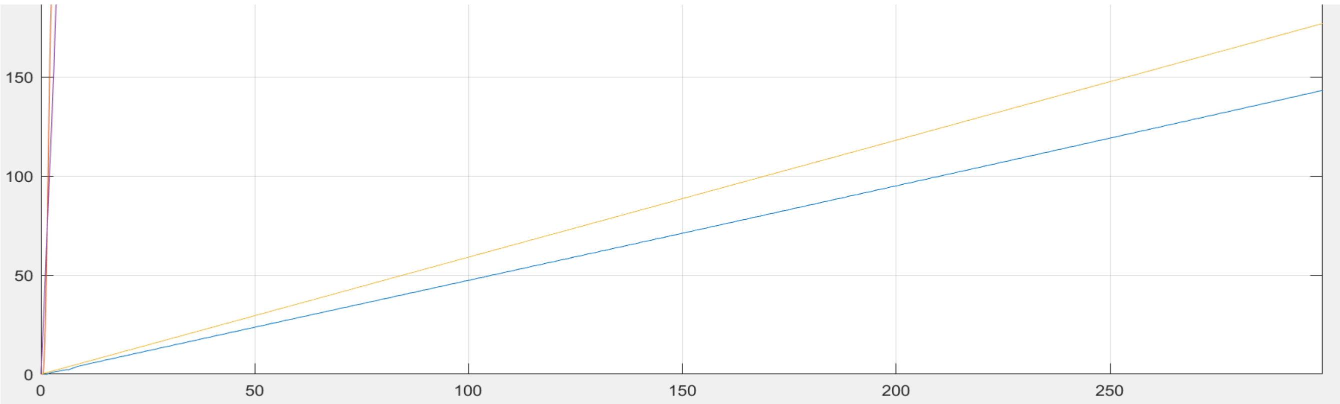

Figure 5.1: Ramp 0.01, Motor and encoder angular position

As can be seen in Figure 5.2, where the motor angular position is plotted for the first ramp, the motor's angular position exhibits a wavy nature, closely resembling the behavior recorded during the test (purple line). As previously mentioned, the influence of friction is clearly visible here through small oscillations around the rising line that the angular position would follow. It is also evident, in line with the developed model, that the period of these small oscillations matches the gear engagement period described in Chapter 3, confirming that for small commands, the gear forces are significant enough to slightly alter the angular position read by the sensor placed on the motor shaft. Moreover, note how realistically close this position is to the one actually recorded during the tests.

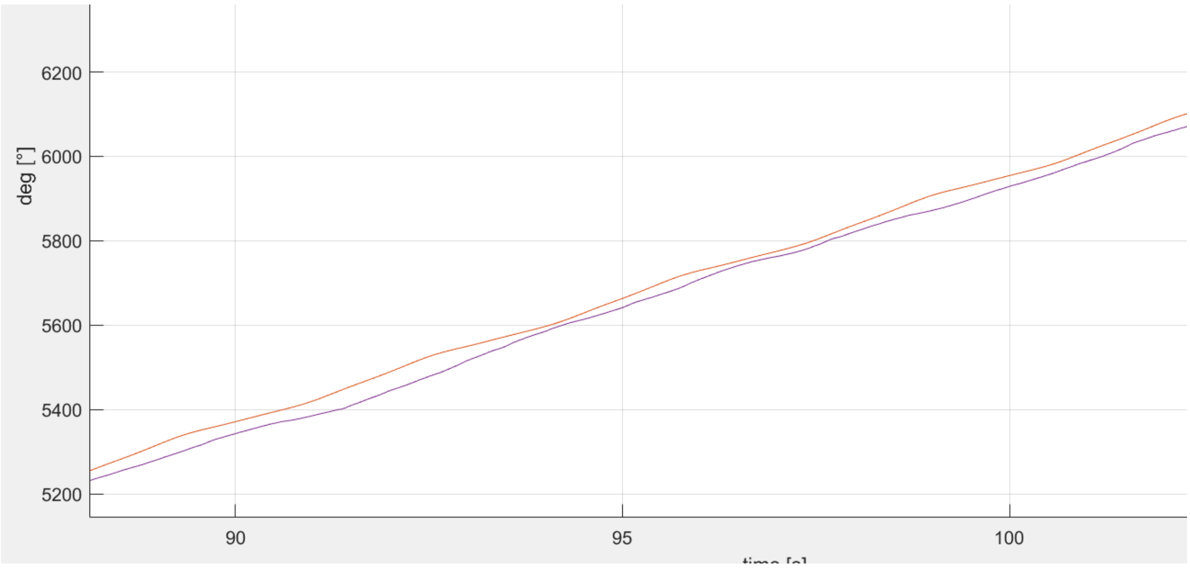

Figure 5.2: Detail of the almost oscillatory trend of motor angular position

2. Ramp command 0.02 rad/s

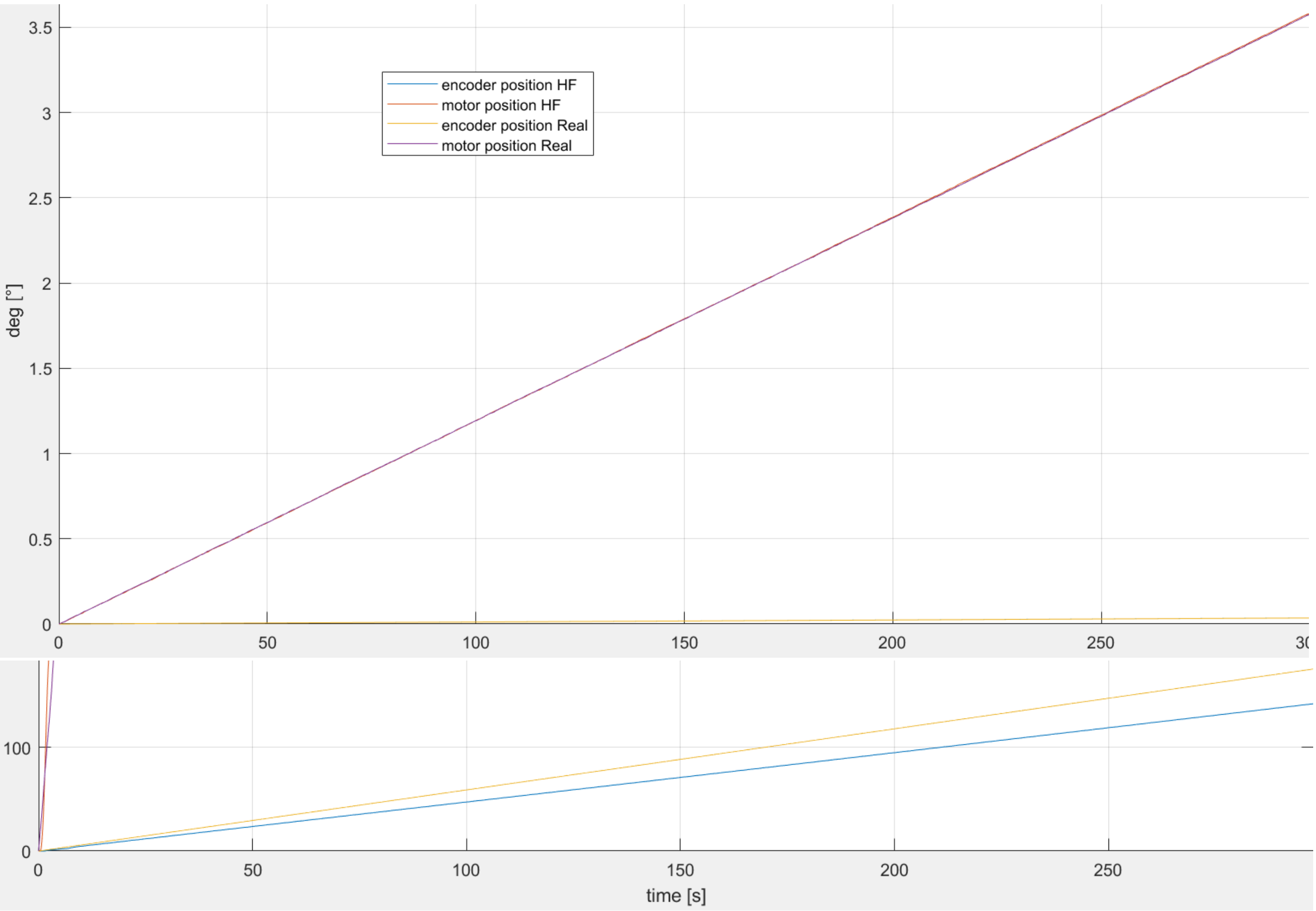

Figure 5.3: Ramp 0.02, Motor and encoder angular position

The order of magnitude in the image above is 10^4.

3. Ramp command 0.03 rad/s

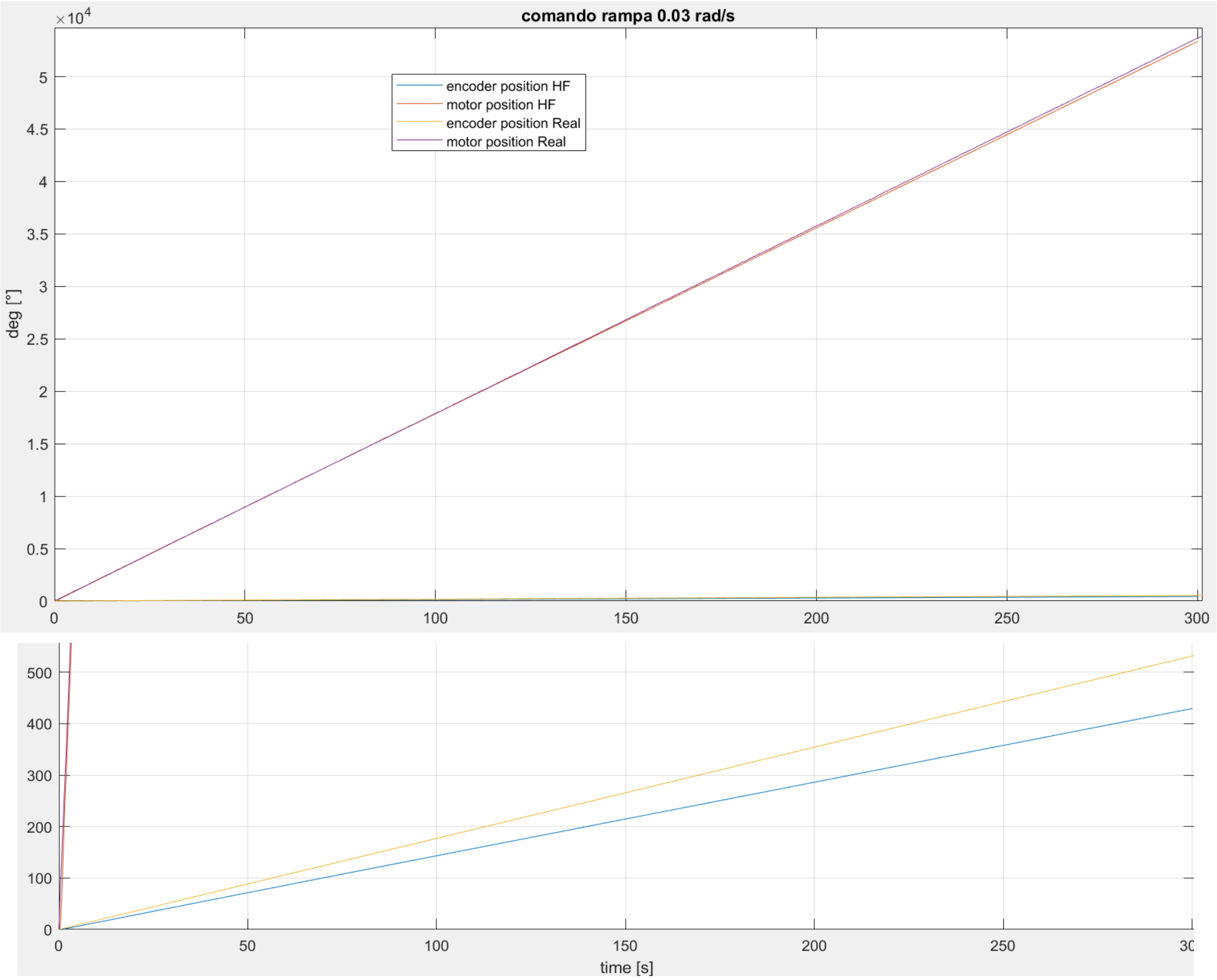

Figure 5.4: Ramp 0.03, Motor and encoder angular position

4. Ramp command 0.04 rad/s

Starting from approximately 0.04 rad/s, the slight fluctuations that were clearly noticeable in the initial ramps begin to fade and are no longer clearly visible, except when zooming into the graph at the order of magnitude of a second.

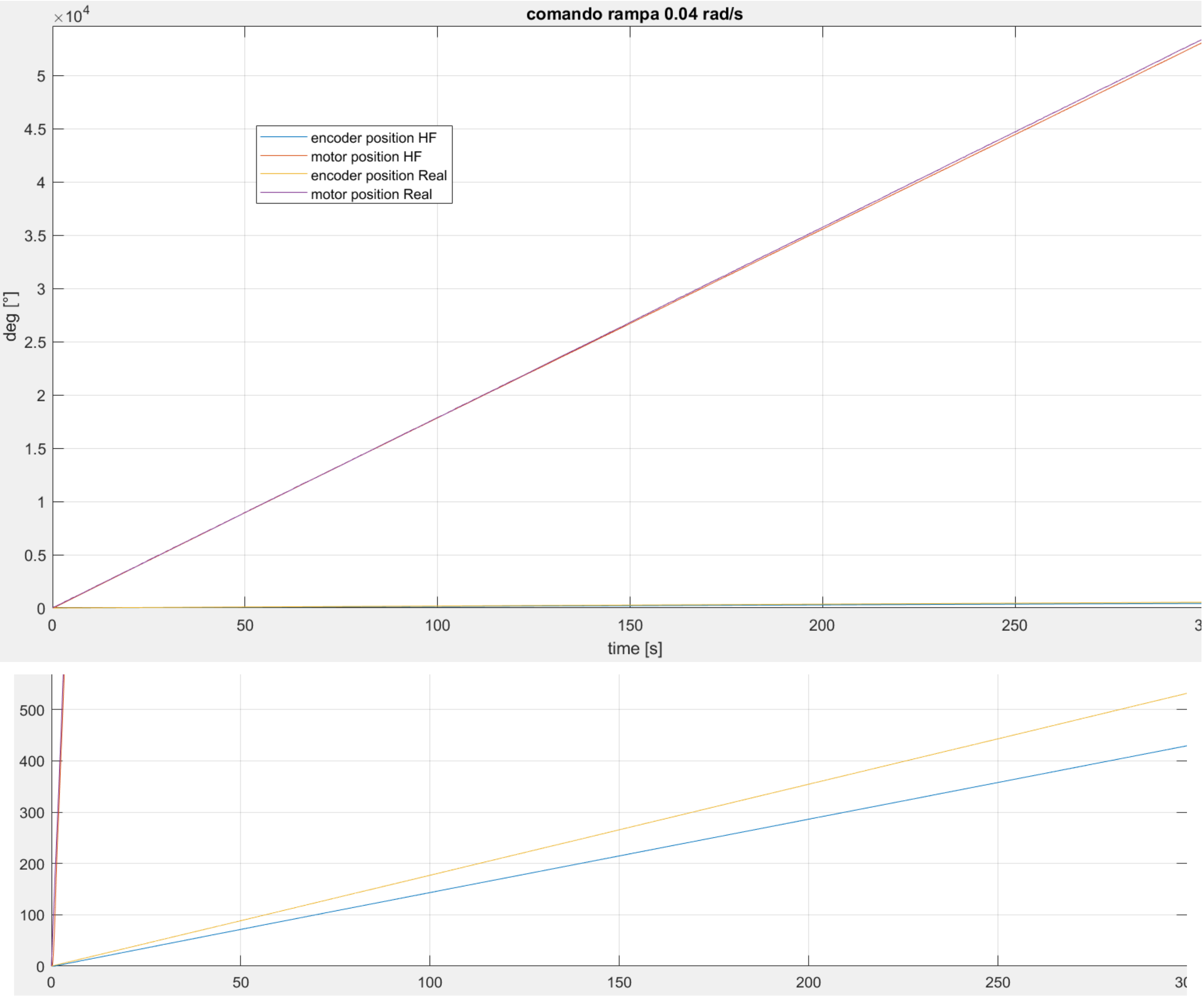

Figure 5.5: Ramp 0.04, Motor and encoder angular position

5. Ramp command 0.05 rad/s

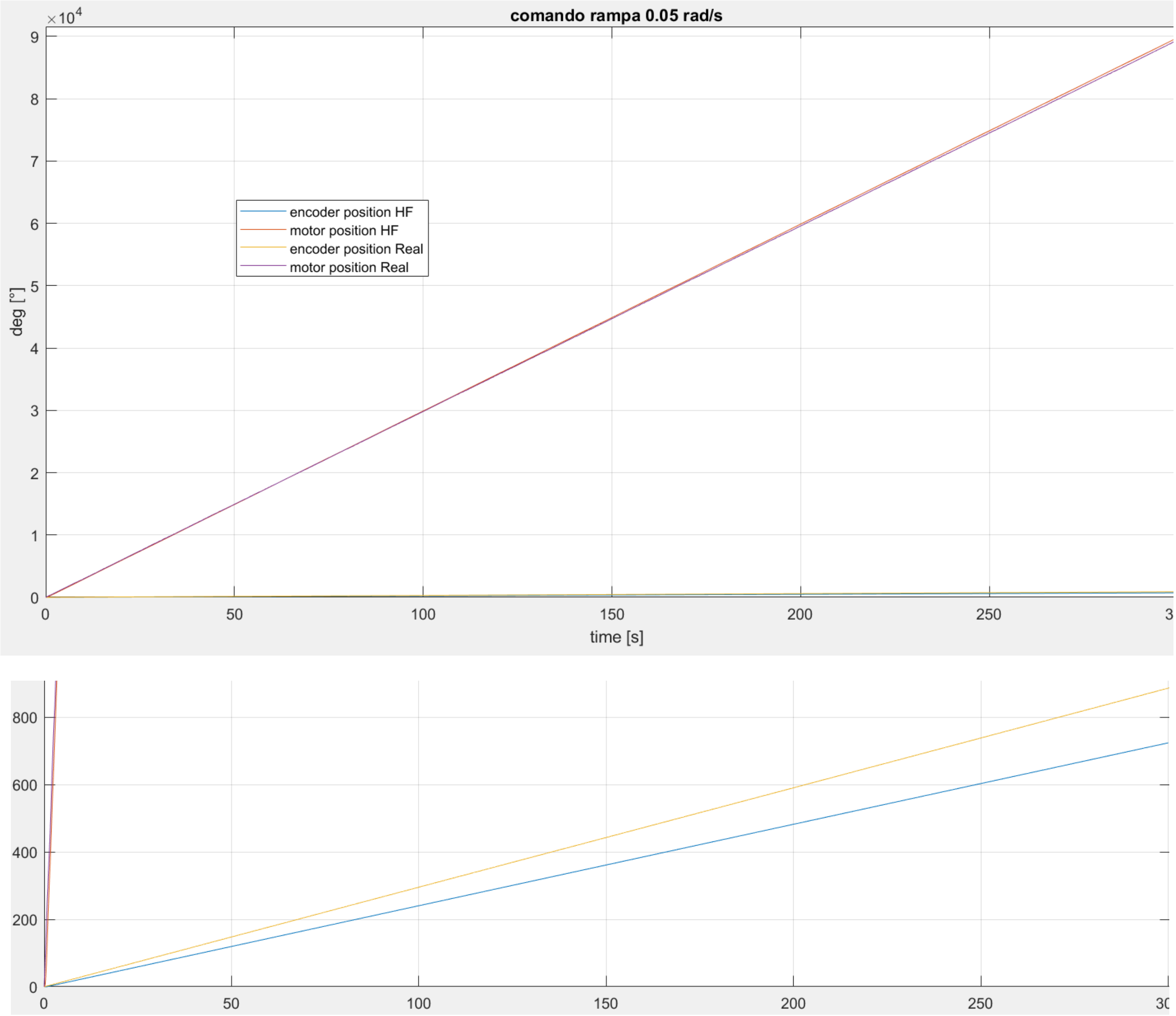

Figure 5.6: Ramp 0.05, Motor and encoder angular position

6. Ramp command 0.06 rad/s

The remaining commands are plotted in graphs that show the experimental results, the old HF model and the new model with the implementation of friction, to better visualize the differences.

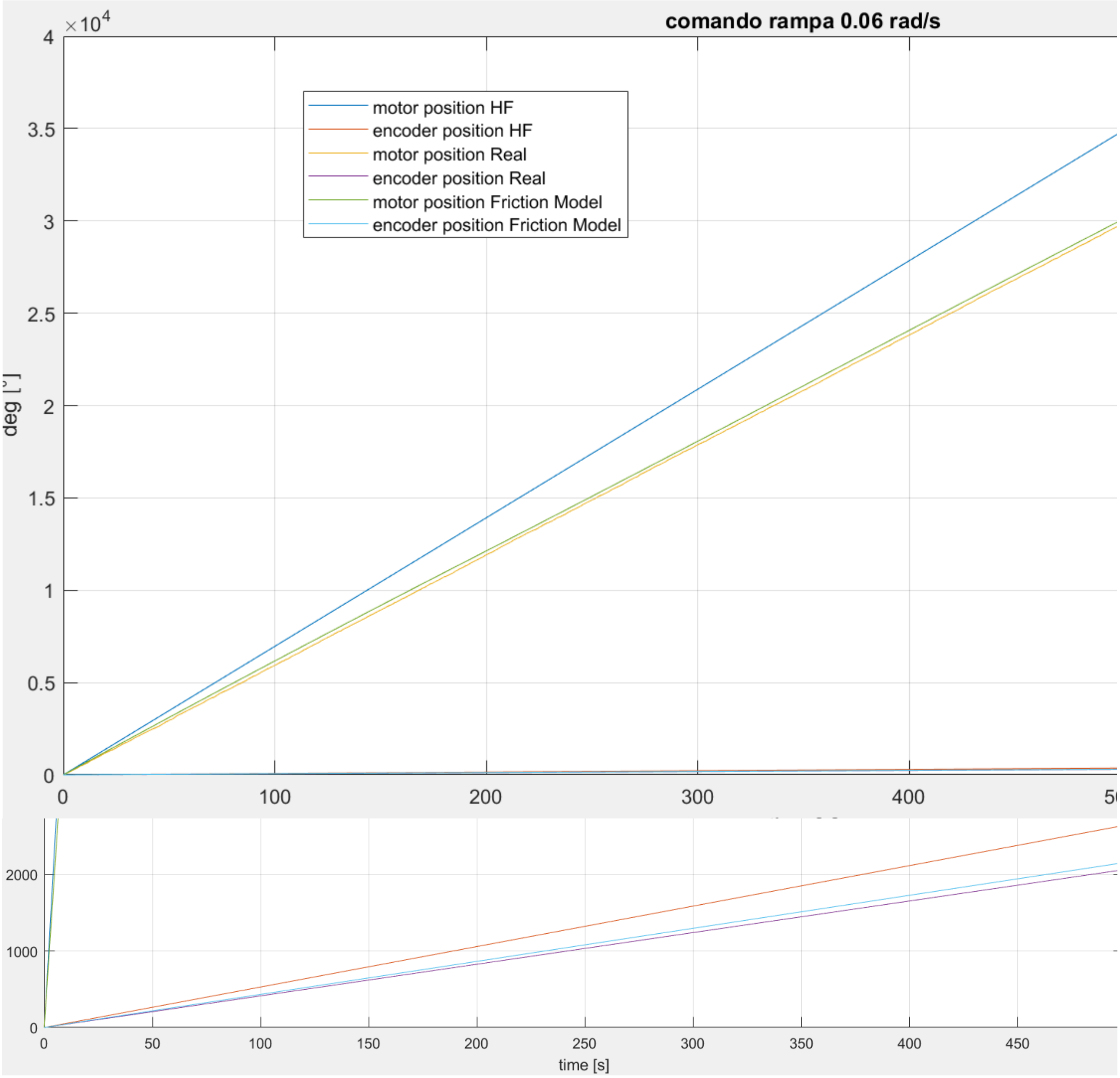

Figure 5.7: Ramp 0.06, Motor and encoder angular position of HF and HFF model

As we can observe, and this applies to previous commands as well, the old HF model is very inaccurate for commands that are prolonged over time, accumulating a steady position error that causes the system to diverge from the actual commanded position. In comparison, the new HFF (High Friction Fidelity) model is much more precise and realistic, deviating from the real position by a much smaller error.

7. Ramp command 0.07 rad/s

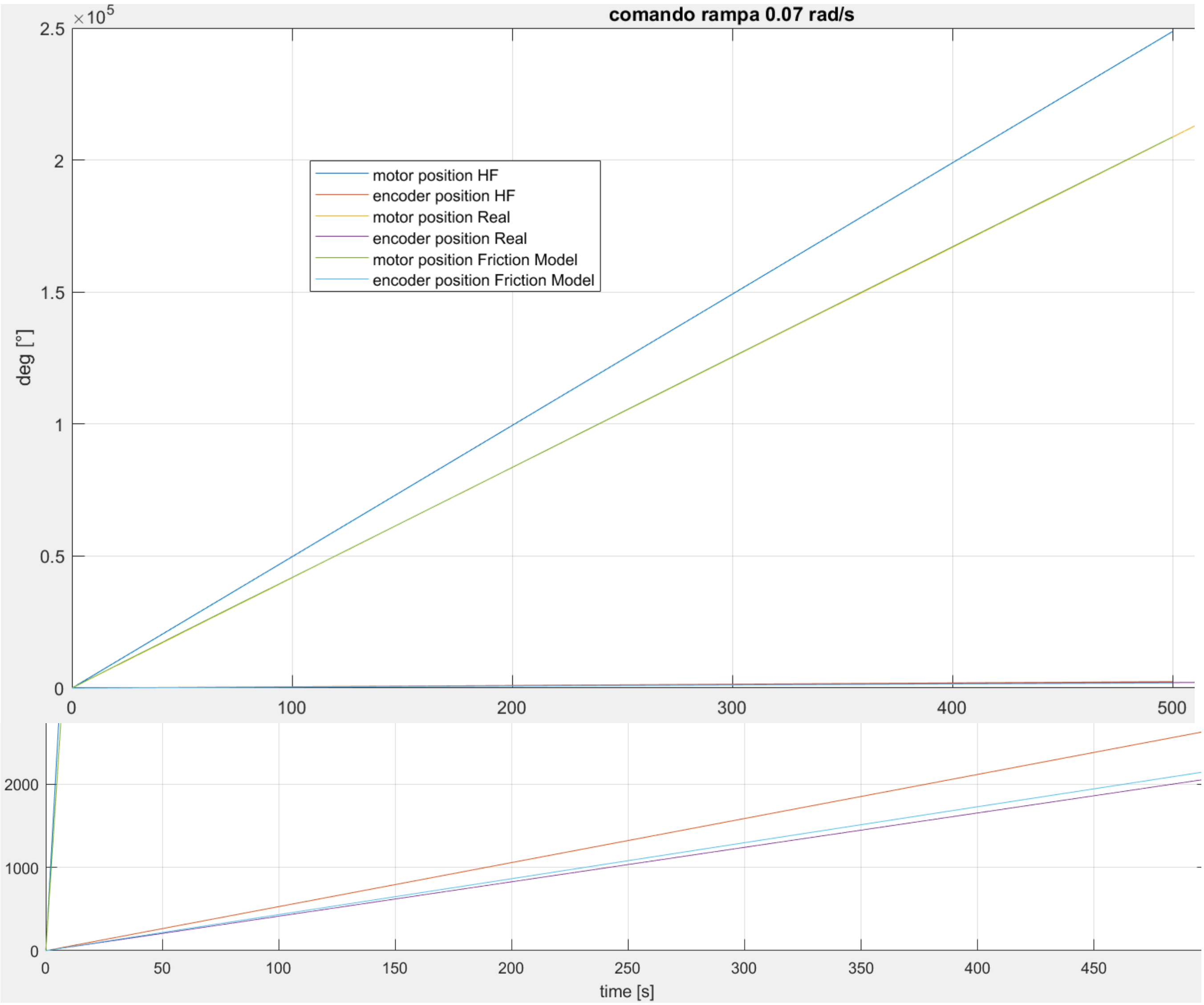

Figure 5.8: Ramp 0.07, Motor and encoder angular position of HF and HFF model

8. Ramp command 0.08 rad/s

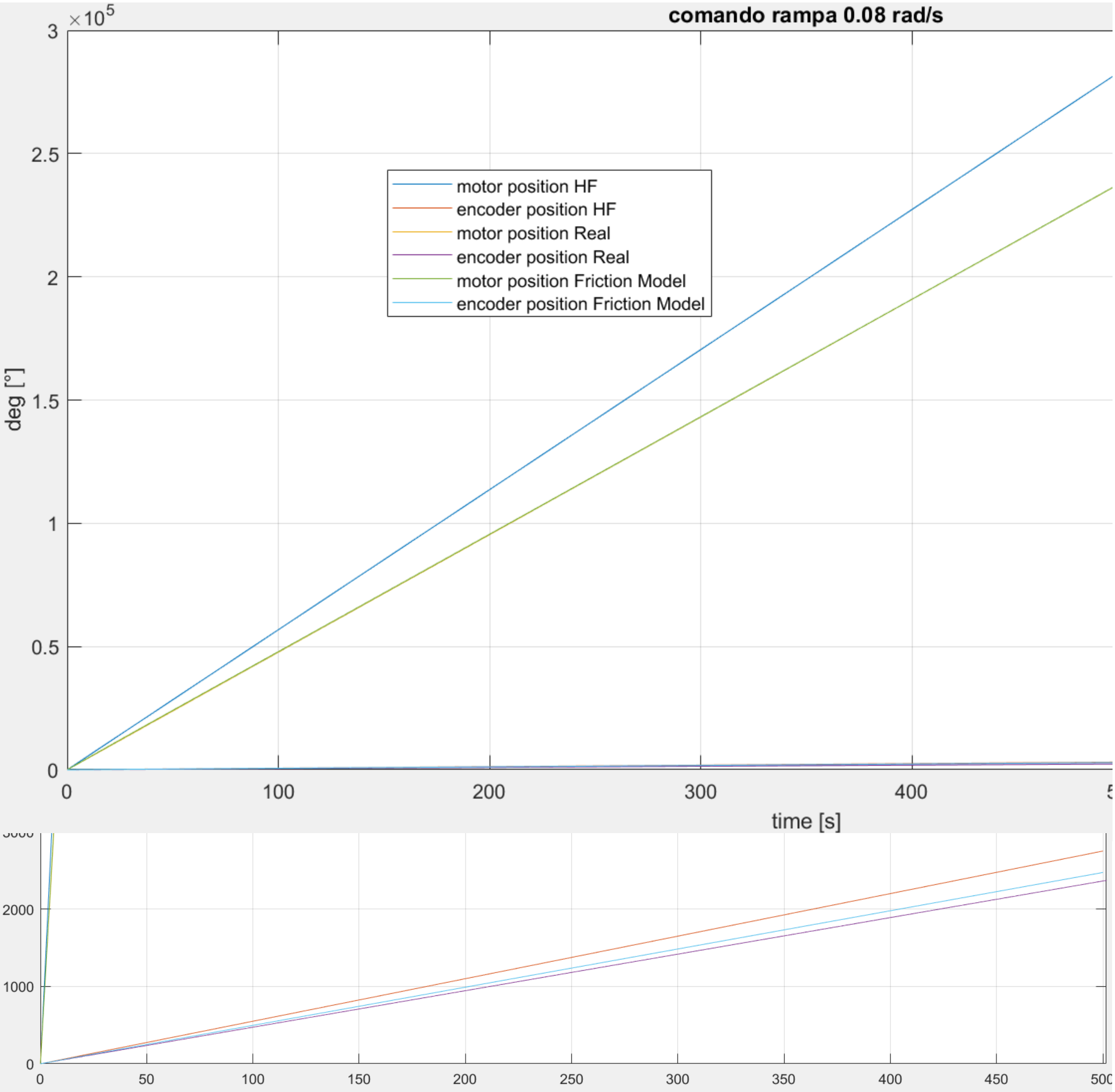

Figure 5.9: Ramp 0.08, Motor and encoder angular position of HF and HFF model

9. Ramp command 0.09 rad/s

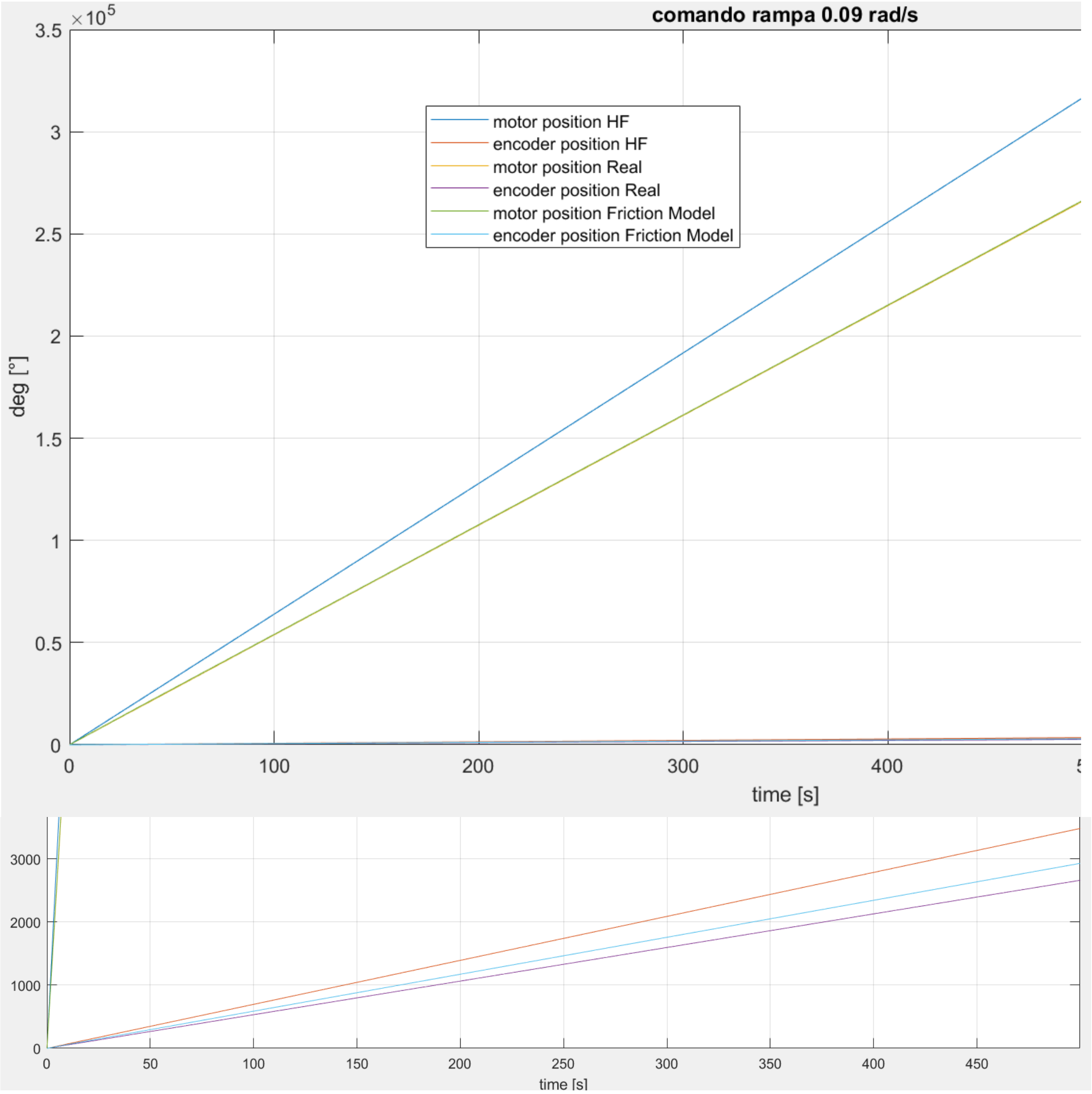

Figure 5.10: Ramp 0.09, Motor and encoder angular position of HF and HFF model

10. Ramp command 0.1 rad/s

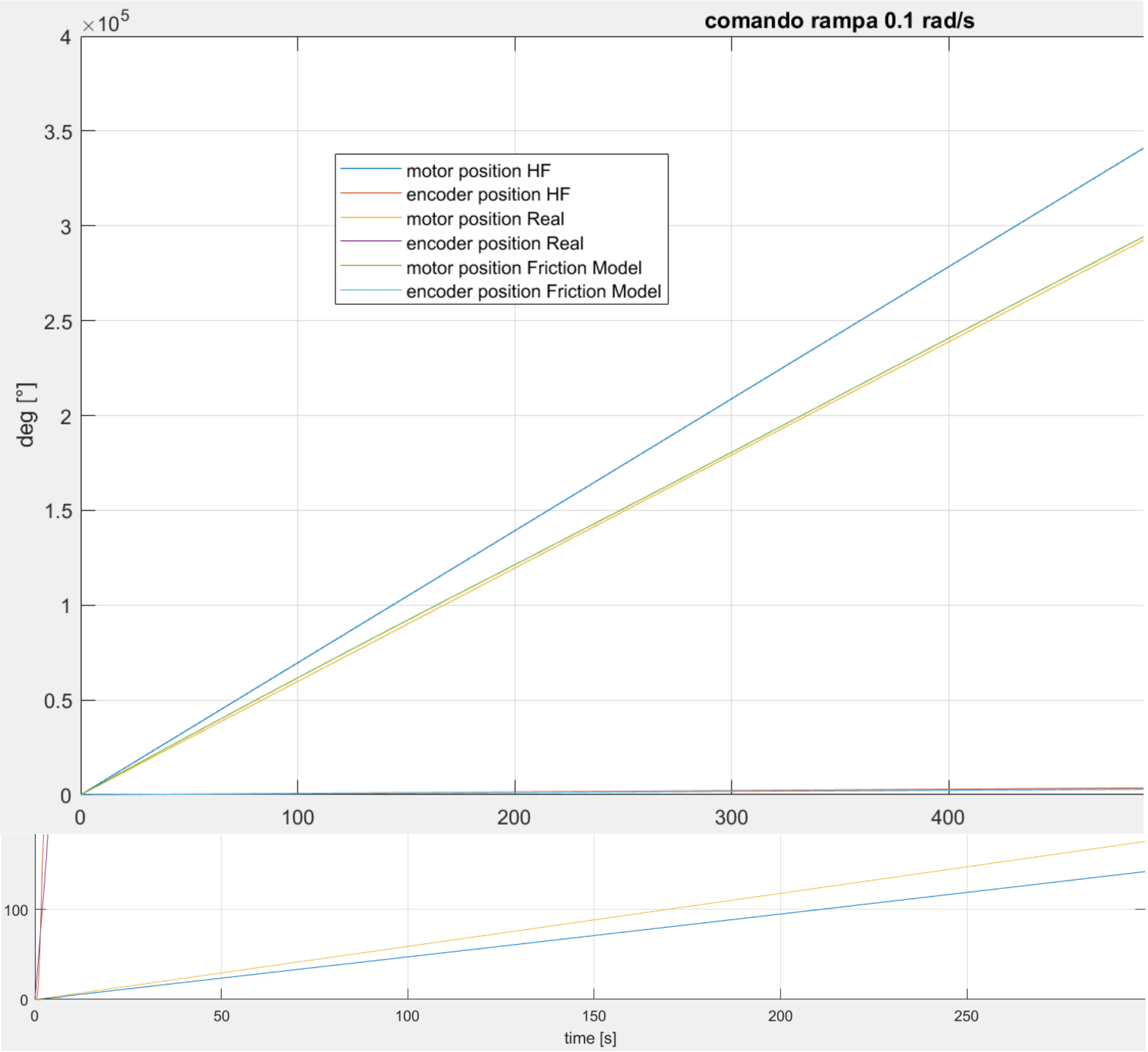

Figure 5.11: Ramp 0.1, Motor and encoder angular position of HF and HFF model

5.1. RMSE calculation

The RMSE (Root Mean Square Error) is a measure of the difference between the predicted values from a model and the actual observed values. It is widely used to assess the accuracy of predictions in regression models or simulations and it has the same unit of measurement as the variables being compared."

To assess the accuracy of the two models, the RMSE of both was estimated with respect to the experimentally recorded values, as it provides an indication of the average magnitude of the error. The formula implemented is:

$$RMSE = \sqrt{\sum_{i=1}^{n} \frac{(\hat{y}_i - y_i)^2}{n}} \tag{5.1}$$

With:

- n is the total number of observations,
- y_i are the actual (measured) values,
- $\tilde{y}_i$ are the predicted (or estimated) values from the model.

Ramp command	**RMSE new HFF model**	**RMSE old HF model**
0,01 rad/s	288,45	4006,93
0,02 rad/s	258,86	7189,55
0,03 rad/s	196,56	10370,17
0,04 rad/s	120,78	13550,79
0,05 rad/s	178,24	16729,41
0,06 rad/s	288,58	19908,03
0,07 rad/s	103,46	23058,65
0,08 rad/s	107,77	26318,57
0,09 rad/s	261,29	29487,77
0,1 rad/s	245,65	32650,39

Table 5.1: RMSE values

A lower value indicates that the model is more accurate in reproducing the actual data; Conversely, a high RMSE indicates that the model is inaccurate.

As we can see from the table, the old HF model gradually reaches increasingly higher RMSE values, which not only means that the model is inaccurate, but also that with larger commands it becomes progressively more imprecise, accumulating an error that grows larger and leads to a response that diverges from the commanded input.

The new model, on the other hand, has low RMSE values, meaning it is very reliable and closely reflects reality. These values are slightly different from each other because the model still includes some simplifications of reality, which bring it closer to it but do not describe it perfectly. In this case, factors such as backlash (which was not considered in the model), numerical factors found in literature, and formulas regarding dissipation between straight-tooth gears (while ours are helical) create small imperfections and differences in the simulation results, but they are negligible compared to the overall outcome.

6. Conclusion and future developments

This thesis explored the dynamic behavior and modeling of an electromechanical actuator (EMA) with a focus on its integration into secondary flight control systems. Through experimental testing and subsequent numerical analysis, it has been developed a refined model that better represents the real-world performance of the EMA, specifically targeting the interaction between the gearbox components and the dissipative forces caused by friction.

The simulation results demonstrate that the newly implemented friction model aligns closely with the experimental data, especially at lower command rates. The observed fluctuations in angular position during meshing further confirm the influence of friction, with periods corresponding to gear engagement cycles. As expected, for smaller commands, the impact of meshing forces becomes increasingly significant, reflecting real-world conditions.

Comparing the old High Fidelity (HF) model with the enhanced friction model, we observed a significant reduction in the Root Mean Square Error (RMSE) values for the new model. The old HF model showed increasing RMSE as commands grew larger, indicating growing divergence from the desired outcomes, while the new model maintained low RMSE, suggesting its reliability in reflecting physical behaviour despite some minor discrepancies due to modelling simplifications.
Looking forward, the model serves as a foundation for future developments, particularly in the areas of prognostics and health management. By incorporating advanced algorithms for predicting the Remaining Useful Life (RUL) of actuator components, future studies could contribute significantly to the reliability and safety of these systems. Additionally, refining the model to account for complex phenomena like backlash and the use of helical gears will further enhance its accuracy and applicability in aerospace applications.

For this particular study, potential future work could include:

- The study and implementation of a gear degradation model, as the presence of tooth damage can induce undesirable dynamic behavior, leading to noise, acoustic emissions, and unacceptable performance, as well as significant reductions in the gearbox's useful life. Therefore, a study on Prognostics and Health Management (PHM) could be conducted;

- The implementation of the backlash function in the new HF Friction model is essential to fully describe the behavior of the meshing gears. It would be important to verify how this affects the model's accuracy and the behavior of the friction forces.

In conclusion, this work offers valuable insights into the behavior of EMAs, contributing to the larger effort of advancing "More Electric Aircraft" technology and paving the way for their broader adoption in critical flight systems.

Politecnico di Torino

Politecnico
di Torino

Appendix A

Kinematic analysis

The components of an epicyclic gear train are:

- the sun gear;
- the ring gear;
- the planets (or satellites);
- the carrier (or planet carrier)

The sun gear is an externally toothed wheel, and the ring gear has internal teeth, both of which are coaxial with the main axis of the gear system. The planets are externally toothed wheels that simultaneously mesh with both the sun and the ring gears. Finally, the planet carrier is the kinematic structure that constrains the axes of the planets to rotate around the main axis of the gear system. There are at least three planets to ensure the balance of inertia forces generated by their rotation around the carrier axis. The planets perform both a rotation around their own axis and a revolution around the sun gear's axis.

The figure belowc shows a schematic of a single-stage epicyclic gear train, indicating the four components that comprise it.

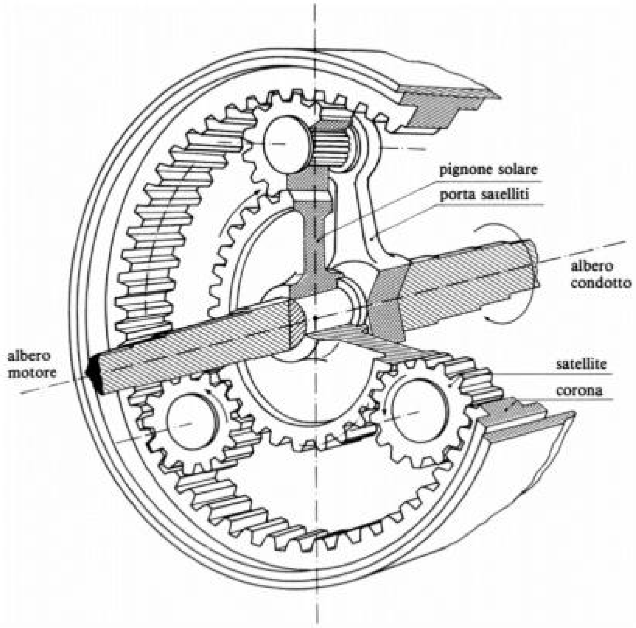

Figure A.1: Single-stage epicyclic gear train

The actuator under examination consists of two stages: the first stage is made up of two sets of sun-planet-ring gears located at the ends of the gearbox to self-balance it. The second stage, where the load is connected via an external gear, is placed in the centre. All the gears have helical teeth, except for the one that engages with the encoder on the output shaft, which has straight teeth. The sun gear is mounted on the input shaft of the gearbox, and the planet carrier is mounted on the output shaft.

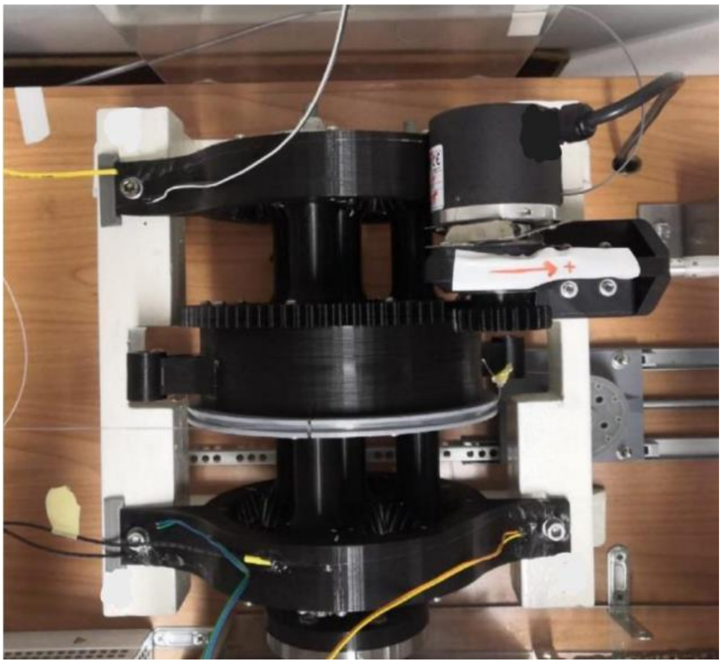

Figure A.2: Top view epicyclic reducer

The first aspect to consider involves the velocities of each individual component and the calculation of the correct transmission ratios. In epicyclic gear reducers, the gears (the satellites) not only rotate around their own axis but also revolve around the axis of the sun gear (i.e., the primary axis of the reducer). This results in relative motions, so each component will have both a relative and an absolute velocity. Assuming an observer fixed to a virtual satellite carrier (even though such a carrier does not exist in our case, we consider it for simplicity), the relative velocities of the sun and the ring gear with respect to the carrier (denoted with an apostrophe) can be expressed as:

$$w'_s = w_s - w_p$$
$$w'_c = w_c - w_p$$

Where:

- w_s is the rotational speed of the sun gear (and w_s' is the relative velocity) [rad/s];
- w_c is the rotational speed of the ring gear (and w_c' is the relative velocity) [rad/s];
- w_p is the rotational speed of the carrier [rad/s].

Using the relative velocities and applying Willis's formula between the sun gear and the ring gear, we have:

$$\tau_o = \frac{w_s'}{w_c'} = \frac{w_c - w_p}{w_s - w_p} = -\frac{z_c}{z_s}$$

The negative sign indicates the opposite directions of rotation. If the ring gear is fixed, with the sun gear mounted on the input shaft and the carrier on the output shaft, the overall transmission ratio of the first stage is determined by setting $w_c = 0$, giving:

$$\tau_0 = \frac{w_s'}{w_c'} = -\frac{w_p}{w_c - w_p}$$

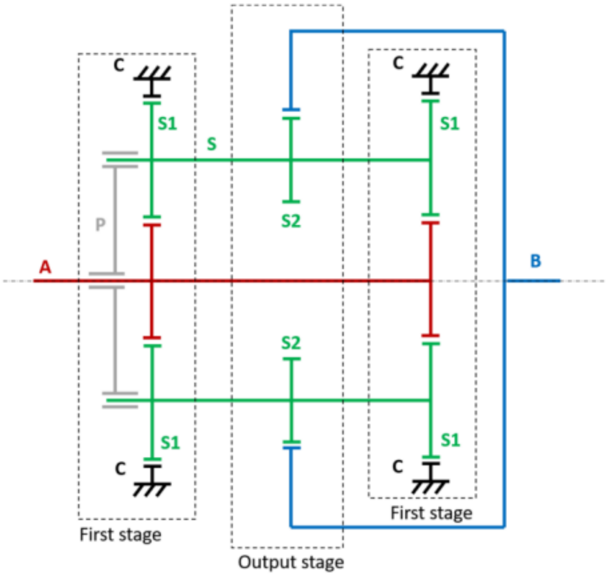

And rewriting $\Omega = \frac{w_s}{\frac{z_c}{z_s}+1}$.

Figure: A.3: Reducer shaft diagram

Finally, apply Willis's formula between the sun gear (input) and the carrier (output).

$$\tau_1 = \frac{w_s - \Omega}{w_p - \Omega} = -\frac{z_p \cdot z_{s_1}}{z_s \cdot z_{s_2}}$$

Substituting the value of Ω found before and doing some calculations we get:

$$\tau = \frac{w_s}{w_p} = \frac{\frac{z_c}{z_s} + 1}{1 - \frac{z_c \cdot z_{s_2}}{z_p \cdot z_{s_1}}} = \frac{4}{0.03225} = 124$$

PLANETARY GEARBOX Basic Datasheet

Moment of inertia reduced to the input shaft.	$\mathbf{1.75 \cdot 10^3}$ $\boldsymbol{g \cdot mm^2}$
Number of teeth of the sun gear z_s	21
Number of teeth of the crown gear z_c	63
Number of teeth of the satellite 1 S_1	21
Number of teeth of the satellites 2/3 S_2	20
Number of teeth of the output shaft z_p	62
Transmission ratio τ	124

Table A.1: Planetary gearbox Datasheet

Appendix B

Script Matlab

Main HF

```
%% Unità di misura utilizzate nella simulazione
% test.time        [s]
% test.pos_ref     [rad] in albero lento
% test.speed_ref   [rad/s]
% test.Iq_ref      [A]
% test.tens_out    [V]
% test.Id          [A]
% test.Iq          [A]
% test.RPM_lvl_act  [rad/s]
% test.pos_act     [rad] in albero veloce
%
%% Unità di misura dati sperimentali
% data.time          [s]
% data.posEncoder    [°] in albero lento
% data.posMotor      [°] in albero lento
% data.velCom        [rpm] in albero lento
% data.velRead       [rpm] in albero lento
% data.ISetpoint     [A]
% data.IActValue     [A]
% data.quadVSetpoint  [V]
% data.Load          [Nm]
% data.amplCom       [°] in albero lento
% data.phCom         [°] in albero lento
% data.freqCom       [Hz] in albero lento

%% Calcolo del gioco sperimentale

%err = max( abs(data.posMotor-data.posEncoder) );
dynamics.BLK = 0.0023;       % [rad] Backlash Width (albero lento)

%% DEFINIZIONE PARAMETRI HF MODEL
%% Parametri simulazione

simulation.TiBr = 10;            % [s] Durata simulazione
simulation.DT = 1e-6;            % [s] Passo di integrazione
simulation.initPos = 0;          % [rad] Posizione iniziale (albero lento)

simulation.tauFilter = 5*10e-5;    % [s] Tempo caratteristico filtro I_3eq

flag = 1;      % Controllo in posizione

%simulation.comSinAmpl = deg2rad( data.amplCom );    % [rad] Ampiezza del comando
%simulation.comSinFreq = data.freqCom * (2*pi);      % [rad/s] Frequenza del comando
```

```
%simulation.comSinPh = deg2rad( data.phCom );       % [rad] Fase iniziale

%% Controller

controller.Gprop = 1000/60*124;    % [1/s] Guadagno proporzionale controller   % 5e2/tau
controller.W_refMax = 8000*pi/30;  % [rad/s] Saturazione errore posizione      % 6060*pi/30%;
controller.I_Max = 22.5;           % [A] Saturazione I_ref
controller.Knoise = 0;             % [] Coefficiente moltiplicativo Rumore (0 - 1 - 10 - 100)

controller.PID.GAP = 0.2368;       % [Nms/rad] Guadagno proporzionale PID      % 0.05;%0.1;%0.75
% controller.PID.GAI = 0;          % [Nm/rad] Guadagno integrativo PID         % 10
% controller.PID.GAD = 0;          % [Nms^2/rad] Guadagno derivativo PID       % 5e-5

controller.PID.ErIM = 100;         % [Nm] Max Errore Integrativo
controller.PID.band = 1e-3;        % [rad] Tolleranza ramo integrativo
controller.PID.Ti = 0.01;          % [s] Tempo caratteristico ramo integrativo
controller.PID.Tt = 1;             % [s] Tempo caratteristico compensazione windup

controller.PID.Td = 0;             % [s] Tempo caratteristico ramo derivativo
controller.PID.N = 1000;           % [1/s] Banda passante filtro derivativo

%% Inverter

inverter.PWM.hb = 0.1;             % [A] Ampiezza banda di isteresi
inverter.Hbridge.Vdc = 380;        % [V] Tensione alimentazione
inverter.Hbridge.RSnubber = 1e5;   % [ohm] Resistenza snubber
inverter.Hbridge.CSnubber = inf;   % [F] Capacità snubber
inverter.Hbridge.Ron = 1e-2;       % [ohm] Ron (in Universal Bridge)

%% Motore

BLDC.P = 4;           % [] Numero paia poli
BLDC.Nabc = [1 1 1];  % [] Frazione spire attive (fasi A, B, C)

BLDC.Rs = 2.75;       % [ohm] Resistenza nominale fase-fase (es. Rab)
BLDC.Ls = 30.5e-3;    % [H] Induttanza nominale fase-fase (es. Lab)
BLDC.Ke = 1.91/2;     % [Nm/A] Costante di fcem del motore

BLDC.TMM = 11.842;    % [Nm] Saturazione coppia
BLDC.zeta = 0;        % [] Modulo eccentricità statica
BLDC.phi = 0;         % [] Fase eccentricità statica

%% Dinamica motore-trasmissione

dynamics.tau = 1/124;       % Rapporto di trasmissione
dynamics.JM = 0.00077;      % [kg*m^2]    Momento d'inerzia del DC Motor (AV=albero veloce)
dynamics.CM = 0.0255;       % [N*m*s/rad]   Coefficiente di smorzamento viscoso dimensionale DC Motor (AV)
dynamics.JU = 1e-3;         % [kg*m^2]    Momento d'inerzia utilizzatore ridotto all'albero veloce
dynamics.CU = 4.5070e-7; %4.5070e-7;     % [N*m*s/rad]   Coefficiente di smorzamento viscoso dimensionale utilizz.(AV)
```

```
dynamics.CM1 = 0.0163;

dynamics.friction.FSTm = 2*0.0676/BLDC.TMM;      % [] Attrito statico  motore       (albero veloce - espresso in percentuale di BLDC.TMM)
dynamics.friction.FDTm = 0.0676/BLDC.TMM;        % [] Attrito dinamico motore       (albero veloce - espresso in percentuale di BLDC.TMM)
dynamics.friction.FSTu = 2*0.045/BLDC.TMM;       % [] Attrito statico  utilizzatore (albero veloce - espresso in percentuale di BLDC.TMM)
dynamics.friction.FDTu = 0.045/BLDC.TMM;         % [] Attrito dinamico utilizzatore (albero veloce - espresso in percentuale di BLDC.TMM)

dynamics.ThUmin = -1.5;    % [rad] Finecorsa inferiore
dynamics.ThUmax = 1500000;    % [rad] Finecorsa superiore

%% Simulation

%data.resistence = data.load + data.friction;

%%
% *BOLD TEXT*

exeSimulation = tic;
sim('modelHF_friction_final.slx')
enlapsedTime = toc(exeSimulation);

%% Salvataggio dati

simResults.time = tout;                  % tempo simulazione
simResults.iA = out(:,1);                % Iq
simResults.V_Afiltered = out(:,2);       % Va filtrata
simResults.V_Bfiltered = out(:,3);       % Vb filtrata
simResults.V_Cfiltered = out(:,4);       % Vc filtrata
simResults.V_3eq = out(:,5);             % V equivalente filtrata
simResults.Vd = out(:,6);                % V dirette filtrata
simResults.deltaVfiltered =out(:,7);     % Delta V filtrata
simResults.Dtheta_m = out(:,8);          % Dtheta M
simResults.theta_u = out(:,9);           % Theta u
simResults.I_3eq = out(:,10);            % I quadratura equivalente trifase
simResults.theta_m = out(:,11);          % Theta M
simResults.Id = out(:,12);               % I diretta equivalente trifase
simResults.PosRef = out(:,13);           % Comando istante per istante
simResults.VelRef = out(:,14);           % Velocità di riferimento ingresso PID
simResults.IqRef = out(:,15);            % I quadratura di riferimento in uscita dal PID
simResults.Tm = out(:,16);               % Coppia esercitata dal motore


simResults.backlash = dynamics.BLK;
simResults.exeTime = enlapsedTime;  % [s]
```

Dinamica riduttore

```
%% RIDUTTORE EPICICLOIDALE
% clear all;
% close all;
% clc

eps=0.047; % pressure-induced shear coefficient
c1=-1.890758; % -1.890758 -2.999
c2=10.5253; % 10.5253 7.852
T=20; %-20:0.20066889:40; % temperature range Celsius
nu_cin=10^(10^(c1*log(T+273.15)+c2)); % viscosità cinematica f(T)
pho_lub=0.869; % densità del lubrificante (assente quindi si prende aria in considerazione)lla temperatura di riferimento[kg/dm3]

psi=-0.001; % density-temperature coefficient
pho_T=pho_lub-((T-15)*6.444*(10^-4));
pho2_T=pho_lub.*(exp(psi.*(T-15)));
nu_din=(nu_cin./10^6).*(pho2_T*1000);

%% dati geometrici delle ruote dentate
pho=7850; % densità [kg/m3]
ns=3; % numero di pianeti
eps_1=1.2;%2 % rapporto di condotta
x_i=0; % fattore di correzione dentatura
alpha=22.5*(pi/180); % angolo di pressionem [rad]
phi_0=(2*pi)/ns; % angolo di distanziamento satelliti [rad]
z_1 = [21 21 63]'; % Solar-satellite-internal gear - 1st stage


% interasse e raggi di base e testa
rbs= 35; %(d_1(1)/2)-1.25*mn_1; % Raggio base solare [mm]
rbp=35; %(d_1(2)/2)-1.25*mn_1 ; % Raggio base satellite [mm]
m= rbs/21;% % modulo normale d_primitivo/n_denti[mm]

Int=rbs+rbp; % Interasse [mm]
rbr=132; % Raggio base corona [mm]
rbc=rbs+rbp; % "Raggio base" porta satellite [mm]
rts=40.6; % Raggio testa solare [mm]
rtp=40.6; % Raggio testa satellite [mm]
rtr=126.4; % Raggio testa corona [mm]
rp= 39.5; %Raggio primitivo solare/satellite [mm]
rpr=127.5; %Raggio primitivo corona [mm]

s_dente=pi*m/2; % spessore dente nella circonferenza primitiva [mm]
s_dente_sat=pi*m/2;
p_base=m*pi*cos(alpha);
```

```
b_1=18; % [mm] larghezza di fascia

m_sol_1=2.5;  % solar mass [kg]
m_cor_1=1.5;  % ring mass [kg]
m_sat_1=2;  % planet mass [kg]


% alberi
d_shaft_in=33; % diametro albero ingresso [mm]
m_shaft_in=0.10; % massa albero ingresso [kg]
l_shaft_in=220; % lunghezza albero ingresso [mm]
E_shaft_in=210; % modulo di elasticità [Gpa]
v=0.3; % coefficiente di poisson
G_shaft_in=E_shaft_in/(2*(1+v)); % modulo elasticità tangenziale [Gpa]

%% cinematica
% rapporti di trasmissione

tau_rp = z_1(2)/z_1(3);
tau_sp = -(z_1(1)/z_1(2));
tau = 1 + (z_1(3)/z_1(1));

% distribuzione coppie-analisi statica
T_s= 6; % [Nm]
T_load_id=T_s*tau;
T_sp=(T_s/3)*(z_1(2)/z_1(1));
F_sp=T_s./(3*2*rp*cos(alpha));
F_rp=F_sp;
F_car=F_sp*cos(alpha) + F_rp*cos(alpha);
T_car=F_car*3*(rp+rp);

%calcolo coppia Tm generata dal comando
Potenza=mean(y5)*mean(y7);
Coppia=Potenza/mean(y4);


% velocità
n_in=0.01*124*60/(2*pi);  %%0.02 0.03 0.04 0.05 ... 0.1   %[rpm]    (velocità motore in rpm) rad/s *60/(2pi) = rpm
omega_in=(2*pi*n_in)/60; % Velocità dell'albero del solare [rad/s]
omega_c=omega_in/tau; % Velocità portasatellite ideale [rad/s]
omega_s=omega_in; % Velocità solare [rad/s]
omega_p=(omega_s-omega_c)*(z_1(1)/z_1(2)); % Velocità relativa satellite [rad/s]
omega_p_ax=omega_p-omega_c; % Velocità assoluta satellite [rad/s]


%% dinamica
% Momenti d'inerzia
I_sol=(((2*rp)^2)/8)*m_sol_1; % momento inerzia solare % [kg*m2]
I_sat=(((2*rp)^2)/8)*m_sat_1; % inerzia satelliti % [kg*m2]
```

```
Igear1 = 1.75E-6; %9.52E-7; % [kgm2] inertia driving shaft (somma dell'inerzia riportata all'albero motore)
Jgb = Igear1*124; % [kgm2] inertia power screw shaft (in quanto Igear1 rappresenta il momento di inerzia ridotto all'albero motore)
Jm= 7700e-6;


%% Rigidezza di ingranamento
%% Solare-pianeta
R_sol_inf=sqrt(((Int*sin(alpha)) - sqrt((m + rp)^2 -(((rp)*cos(alpha))^2)))^2 + ((rp)*cos(alpha))^2);
A=0; % inizio segmento dei contatti
B=(eps_1-1)*2*pi/z_1(1);
C=2*pi/z_1(1);
D=eps_1*2*pi/z_1(1);

% primo tratto (due coppie di denti in presa)
tetaAB=linspace(A,B); % vettore avanzamento angolo di ingranamento da A a B
rAB_1=sqrt((((rp)*cos(alpha)).^2) + (sqrt((R_sol_inf.^2)-(((rp)*cos(alpha)).^2)) + (rp)*cos(alpha).*tetaAB).^2);
rAB_2=sqrt((((rp)*cos(alpha)).^2) + ((Int*sin(alpha) - sqrt(rAB_1.^2 - ((rp)*cos(alpha)).^2))).^2);
[KAB_sol]=mesh_stiffness(m,z_1(1),2*rp,rAB_1,x_i);
[KAB_sat]=mesh_stiffness(m,z_1(2),2*rp,rAB_2,x_i);

% secondo tratto (una coppia di denti in presa)
tetaBC=linspace(B,C); % vettore avanzamento angolo di ingranamento da A a B
rBC_1=sqrt((((rp)*cos(alpha)).^2) + (sqrt((R_sol_inf.^2)-(((rp)*cos(alpha)).^2)) + (rp)*cos(alpha).*tetaBC).^2);
rBC_2=sqrt((((rp)*cos(alpha)).^2) + ((Int*sin(alpha) - sqrt(rBC_1.^2 - ((rp)*cos(alpha)).^2))).^2);
[KBC_sol]=mesh_stiffness(m,z_1(1),2*rp,rBC_1,x_i);
[KBC_sat]=mesh_stiffness(m,z_1(2),2*rp,rBC_2,x_i);

% terzo tratto (due coppie di denti in presa)
tetaCD=linspace(C,D); % vettore avanzamento angolo di ingranamento da C a D
rCD_1=sqrt((((rp)*cos(alpha)).^2) + (sqrt((R_sol_inf.^2)-(((rp)*cos(alpha)).^2)) + (rp)*cos(alpha).*tetaCD).^2);
rCD_2=sqrt((((rp)*cos(alpha)).^2) + ((Int*sin(alpha) - sqrt(rCD_1.^2 - ((rp)*cos(alpha)).^2))).^2);
[KCD_sol]=mesh_stiffness(m,z_1(1),2*rp,rCD_1,x_i);
[KCD_sat]=mesh_stiffness(m,z_1(2),2*rp,rCD_2,x_i);

% rigidezza con due coppie di denti in presa (AB e CD)
KAB_eq= (KAB_sol.*KAB_sat)./(KAB_sol + KAB_sat); % rigidezza equivalente due molle in serie (1 coppia di denti in presa)
KCD_eq= (KCD_sol.*KCD_sat)./(KCD_sol + KCD_sat); % rigidezza equivalente due molle in serie (1 coppia di denti in presa)
Keq_2cop = (b_1/1000).*(KAB_eq + KCD_eq); % rigidezza equivalente due molle in parallelo (due coppie di denti in presa)

% rigidezza con 1 coppiA di denti in presa (BC)
Keq_1cop= (b_1/1000).*((KBC_sol.*KBC_sat)./(KBC_sol + KBC_sat));
% creazione vettori da plottare
tetaAD=[tetaAB tetaBC tetaCD];
```

```
Rig_sol_sat=[Keq_2cop Keq_1cop Keq_2cop];
r_punto_pignonesol=[rAB_1,rBC_1,rCD_1];
r_punto_ruotasat=[rAB_2,rBC_1,rCD_2];


%% Pianeta-corona
R_sat_inf=sqrt(((Int*sin(alpha)) - sqrt((-m + (rpr))^2 -(((rpr)+ (1.25*m))^2))^2 + ((rp)*cos(alpha))^2));
Apr=0; % inizio segmento dei contatti
Bpr=(eps_1-1)*2*pi/z_1(2);
Cpr=2*pi/z_1(2);
Dpr=eps_1*2*pi/z_1(2);

% primo tratto (due coppie di denti in presa)
tetaABpr=linspace(Apr,Bpr); % vettore avanzamento angolo di ingranamento da A a B
rAB_1_pr=sqrt((((rp)*cos(alpha)).^2) + (sqrt((R_sat_inf.^2)-(((rp)*cos(alpha)).^2)) +
(rp)*cos(alpha).*tetaABpr).^2);
rAB_2_pr=sqrt((((rpr)+ (1.25*m)).^2) + ((Int*sin(alpha) - sqrt(rAB_1_pr.^2 - ((rp)*cos(alpha)).^2))).^2);
[KAB_sat_pr]=mesh_stiffness(m,z_1(2),2*rp,rAB_1_pr,x_i);
[KAB_ring_pr]=mesh_stiffness(m,z_1(3),2*rpr,rAB_2_pr,x_i);

% secondo tratto (una coppia di denti in presa)
tetaBCpr=linspace(Bpr,Cpr); % vettore avanzamento angolo di ingranamento da A a B
rBC_1_pr=sqrt((((rp)*cos(alpha)).^2) + (sqrt((R_sat_inf.^2)-(((rp)*cos(alpha)).^2)) +
(rp)*cos(alpha).*tetaBCpr).^2);
rBC_2_pr=sqrt((((rpr)+ (1.25*m)).^2) + ((Int*sin(alpha) - sqrt(rBC_1_pr.^2 - ((rp)*cos(alpha)).^2))).^2);
[KBC_sat_pr]=mesh_stiffness(m,z_1(2),2*rp,rBC_1_pr,x_i);
[KBC_ring_pr]=mesh_stiffness(m,z_1(3),2*rpr,rBC_2_pr,x_i);

% terzo tratto (due coppie di denti in presa)
tetaCDpr=linspace(Cpr,Dpr); % vettore avanzamento angolo di ingranamento da A a B
rCD_1_pr=sqrt((((rp)*cos(alpha)).^2) + (sqrt((R_sat_inf.^2)-(((rp)*cos(alpha)).^2)) +
(rp)*cos(alpha).*tetaCDpr).^2);
rCD_2_pr=sqrt((((rpr)+ (1.25*m)).^2) + ((Int*sin(alpha) - sqrt(rBC_1_pr.^2 - ((rp)*cos(alpha)).^2))).^2);
[KCD_sat_pr]=mesh_stiffness(m,z_1(2),2*rp,rCD_1_pr,x_i);
[KCD_ring_pr]=mesh_stiffness(m,z_1(3),2*rpr,rCD_2_pr,x_i);

% rigidezza con due coppie di denti in presa (AB e CD)
KAB_eq_pr= (KAB_sat_pr.*KAB_ring_pr)./(KAB_sat_pr + KAB_ring_pr); % rigidezza equivalente due molle in serie
(1 coppia di denti in presa)
KCD_eq_pr= (KCD_sat_pr.*KCD_ring_pr)./(KCD_sat_pr + KCD_ring_pr); % rigidezza equivalente due molle in serie
(1 coppia di denti in presa)
Keq_2cop_pr = (KAB_eq_pr + KCD_eq_pr).*(b_1/1000);% rigidezza equivalente due molle in parallelo (due coppie
di denti in presa)

% rigidezza con 1 coppiA di denti in presa (BC)
Keq_1cop_pr= ((KBC_sat_pr.*KBC_ring_pr).*(b_1/1000))./(KBC_sat_pr + KBC_ring_pr);
% creazione vettori da plottare
tetaADpr=[tetaABpr tetaBCpr tetaCDpr];
Rig_sat_ring=-[Keq_2cop_pr Keq_1cop_pr Keq_2cop_pr];
Rig_sat_ring_TOT=repmat(Rig_sat_ring,1,14);
```

```
r_punto_pignonesat=[rAB_1_pr,rBC_1_pr,rCD_1_pr];
r_punto_ruotacor=[rAB_2_pr,rBC_1_pr,rCD_2_pr];
lcont_1=rbs.*tan(tetaAD);
tetaADpr_TOT=linspace(0,2*pi,length(Rig_sat_ring_TOT));

%% rigidezza con Fourier e smorzamento riduttore
% rigidezze e smorzamenti costanti
Keq_1cop_const=mean(Keq_1cop); % in prima approssimazione considero ksp=krp=costante
Keq_1cop_const_pr=mean(Keq_1cop_pr);
ksp=(0.75*eps_1 + 0.25)*Keq_1cop_const*(b_1/1000);
kcp=ksp;
damp_ratio=(0.3+0.17)/2;
csp=2*damp_ratio*sqrt((ksp*m_sol_1*m_sat_1/(m_sat_1+m_sol_1)));
crp=2*damp_ratio*sqrt(kcp*m_sat_1);

p=[32 63 95];
FI=[p(1)*2*pi/(z_1(1)+z_1(3)) p(2)*2*pi/(z_1(1)+z_1(3)) p(3)*2*pi/(z_1(1)+z_1(3))];

gammaS1=(z_1(1)*FI(1)/(2*pi))*pi/180; %sfasamento relativo fra l ingranamento della 1a coppia solare-pianeta e quello fra la prima coppia solare-pianeta (se stessa);
gammaS2=(z_1(1)*FI(2)/(2*pi))*pi/180;%sfasamento relativo fra l ingranamento della 2a coppia solare-pianeta e quello fra la prima coppia solare-pianeta;
gammaS3=(z_1(1)*FI(3)/(2*pi))*pi/180;%sfasamento relativo fra l ingranamento della 3a coppia solare-pianeta e quello fra la prima coppia solare-pianeta;


gammaC1=-(z_1(3)*FI(1)/(2*pi))*pi/180;%sfasamento relativo fra l'ingranamento della 1a coppia corona-pianeta e quello fra la prima coppia corona-pianeta
gammaC2=-(z_1(3)*FI(2)/(2*pi))*pi/180; %sfasamento relativo fra l'ingranamento della 2a coppia corona-pianeta e quello fra la prima coppia corona-pianeta
gammaC3=-(z_1(3)*FI(3)/(2*pi))*pi/180;%sfasamento relativo fra l'ingranamento della 2a coppia corona-pianeta e quello fra la prima coppia corona-pianeta

gammaCS=(gammaS1-gammaC1)/p_base;


%%
f_s = omega_in/(2*pi);
fmesh= f_s*(z_1(1)*z_1(3))/(z_1(1)+z_1(3));
Tmesh=1/fmesh;

%% %% rigidezza alberi
k_shaft_in=0*(G_shaft_in)*pi*(d_shaft_in/2)^4/(6*l_shaft_in); % [Nm] rigidezza torsionale albero solare
c_shaft_in=0.003;
K_shaft = (pi*8^4/32)*(210*1E3*0.33)/40/1000;
C_shaft = 2*0.1*sqrt((Jgb/tau^2*Jm)/(Jgb/tau^2+Jm)*K_shaft);

%% segmento di contatto SOLARE-PIANETA
% lunghezza segmenti di contatto solare-satellite
s_acc=sqrt((rtp^2)-(rbp^2)) - rp*sin(alpha); % tutti in [mm]
```

```
s_rec=sqrt((rts^2)-(rbs^2)) - rp*sin(alpha);
s_cont=s_acc+s_rec;
s_base=(rbs+rbp)*tan(alpha);
d1=sqrt((r_punto_pignonesol.^2)-(R_sol_inf^2));
d2=s_cont-d1;
lcont=rbs.*tan(tetaAD);

% t_medio=sbase/(1.15*(d_1st(1)/2)*cos(alpha));
T1A=(rp + rp)*sin(alpha) - sqrt((rtp^2)-(rbp^2));
BT2=(rp + rp)*sin(alpha) - sqrt((rts^2)-(rbs^2));
% tperc=lcont./(omega_s*rbs*cos(alpha));
teta_rif_A=atan((rbs*tan(alpha) - s_acc)/rbs); % maldotti
teta_rif_B=atan((rbs*tan(alpha) + s_rec)/rbs); % maldotti
teta_rif=linspace(teta_rif_A,teta_rif_B,300); % maldotti
ldc_length_deg=(teta_rif(end)-teta_rif(1))/10; % delta di rotazione solare contatto segmento di ingranamento
pho1=(rbs/1000)*tan(teta_rif); % raggi dei cerchi equivalenti


% carico che si divide lungo la linea di contatto
F_spAB=linspace(F_sp/3,(2/3)*F_sp,length(tetaAB));
F_spBC=(2/3)*F_sp*ones(1,length(tetaBC));
F_spCD=linspace((2/3)*F_sp,F_sp/3,length(tetaCD));
F_sp_lin=[F_spAB F_spBC F_spCD];


%% segmento di contatto CORONA-PIANETA
% lunghezza segmenti di contatto solare-satellite
s_cont_pr=Int*sin(alpha)+ sqrt((rtp^2)-(rbp^2)) - sqrt((rbr^2)-(rtr^2));  % [mm]
s_acc_pr=rbr*tan(alpha) - sqrt((rbr^2)-(rtr^2));
s_rec_pr= s_acc_pr-s_cont_pr;
teta_rif_A_pr=atan((rbp*tan(alpha) - s_acc_pr)/rbp);
teta_rif_B_pr=atan((rbp*tan(alpha) + s_rec_pr)/rbp);
teta_rif_pr=-linspace(teta_rif_A_pr,teta_rif_B_pr,300);
ldc_length_deg_pr=-(teta_rif_pr(end)-teta_rif_pr(1))/15;
N2B2=sqrt((rbr^2)-(rtr^2))-Int*sin(alpha);
Q2B2=(rbp*tan(alpha) + rbp*(pi-(2*alpha)) + rbp*tan(alpha)) -s_acc_pr -s_dente_sat;
B2Q3= p_base - p_base.*((Q2B2/p_base)-round(Q2B2/p_base));
P2Q3=abs(B2Q3-s_acc_pr);
gamma_rs=P2Q3./p_base;
pho1_pr=N2B2/1000 +(rbp/1000)*tan(teta_rif_pr);
pho2_pr=Int*sin(alpha)+pho1_pr; % da correggere
lcont_2_pr=linspace(-s_acc_pr,s_rec_pr,length(teta_rif_pr));


%% stima coefficiente di attrito ISO/TR 14179-2
% SOLARE-PIANETA
sigma=(0.1+0.1)/(2*(10^6)); % sqrt((0.1/(10^6))^2 + (0.1/(10^6))^2) (0.1+0.1)/(2*(10^6))
r_curv=1/(rp/1000) + 1/(rp/1000);
v_per=omega_s*rp/(1000);   % m/s
v_sw=2*v_per*sin(alpha);
```

```
K=(1000*T_s*(z_1(1)+z_1(2)))/(2*(b_1)*((rp^2)*z_1(2)));
f_att=((nu_cin.^(-0.223))*(K.^(-0.40)))./(3.239*v_per.^(0.7));
f_att2=0.048*(((1./(b_1/1000))./v_sw).^0.2).*((nu_din).^(-0.05))*(sigma^0.25);    %% r_curv_r
const=0.048*((nu_din).^(-0.05)).*(sigma^0.25);
f_att_average=mean(f_att2);


% PIANETA-CORONA
sigma_r=(0.1+0.1)/(2*(10^6)); % sqrt((0.1/(10^6))^2 + (0.1/(10^6))^2) (0.1+0.1)/(2*(10^6))
r_curv_r=1/(rp/1000) - 1/(rpr/1000);
v_per_r=omega_p*(rp)/(1000);
v_sw_r=2*v_per_r*sin(alpha);
K_r=(1000*(T_s/3)*(z_1(2)+z_1(3)))/(2*(b_1/1000)*((rp^2)*z_1(3)));
f_att_r=((nu_cin.^(-0.223))*(K_r.^(-0.40)))./(3.239*v_per_r.^(0.7));
f_att2_r =0.048.*(((1./(b_1/1000))./(v_sw_r)).^0.2).*((nu_din).^(-0.05))*(sigma.^0.25);
const_r= 0.048*((nu_din*1000).^(-0.05)).*(sigma_r^0.25);
f_att_average_r=mean(f_att2_r);

%% stima coefficiente di attrito ISO/TS 6336-4
f_att_6336=0.143.*(((sigma.*(1./(b_1/1000)))./(v_per.*nu_din)).^0.25);
f_att_average_6336=mean(f_att_6336);
f_att_6336_r=0.143.*(((sigma_r.*(1./(b_1/1000)))./(v_per_r.*nu_din)).^0.25);
f_att_average_6336_r=mean(f_att_6336_r);
```

Mesh Stifness

```
function [K] =mesh_stiffness(mn,Z,d,r,x_i)
% % La funzione calcola le rigidezze del dente e la rigidezza di ingranamento
% Input:
% - mn=modulo
% - Z: vettore 3x1 contenente il numero di denti delle ruote dei due stadi
% - d=diametro primitivo
% - r=posizione punto di contatto dentatura lungo la linea di contatto
% - x_i= fattore di correzione

A_0 = 3.867 + 1.612*Z - 0.02916*(Z^2) + 0.0001553*(Z^3);
A_1 = 17.060 + 0.7289*Z - 0.01728*(Z^2) + 0.00009993*(Z^3);
A_2 = 2.637 - 1.222*Z + 0.02217*(Z^2) - 0.0001179*(Z^3);
A_3 = -6.330 - 1.033*Z + 0.02068*(Z^2) - 0.0001130*(Z^3);
K=(10^9)*((A_0 + A_1*x_i) + (A_2 + A_3*x_i)*(((r)-(d/2))/((1+x_i)*mn)));
end
```

BancoEMA_ramp0.01

```
%% 0,02 %%0,03 %0,04… %0,09 %0,1

tau=124;
opts = delimitedTextImportOptions("NumVariables", 9);

% Specify range and delimiter
opts.DataLines = [1, Inf];
opts.Delimiter = ";";

% Specify column names and types
opts.VariableNames = ["Xms", "C0Drive_axis_1r4821", "C1Drive_axis_1r4820", "C2Drive_axis_1r62",
"C3Drive_axis_1r63", "C4Drive_axis_1r77", "C5Drive_axis_1r76", "C6Drive_axis_1r1733", "Var9"];
opts.SelectedVariableNames = ["Xms", "C0Drive_axis_1r4821", "C1Drive_axis_1r4820", "C2Drive_axis_1r62",
"C3Drive_axis_1r63", "C4Drive_axis_1r77", "C5Drive_axis_1r76", "C6Drive_axis_1r1733"];
opts.VariableTypes = ["double", "double", "double", "double", "double", "double", "double", "double", "string"];

% Specify file level properties
opts.ExtraColumnsRule = "ignore";
opts.EmptyLineRule = "read";

% Specify variable properties
opts = setvaropts(opts, "Var9", "WhitespaceRule", "preserve");
opts = setvaropts(opts, "Var9", "EmptyFieldRule", "auto");
opts = setvaropts(opts, ["Xms", "C0Drive_axis_1r4821", "C1Drive_axis_1r4820", "C2Drive_axis_1r62",
"C3Drive_axis_1r63", "C4Drive_axis_1r77", "C5Drive_axis_1r76", "C6Drive_axis_1r1733"], "TrimNonNumeric",
true);
opts = setvaropts(opts, ["Xms", "C0Drive_axis_1r4821", "C1Drive_axis_1r4820", "C2Drive_axis_1r62",
"C3Drive_axis_1r63", "C4Drive_axis_1r77", "C5Drive_axis_1r76", "C6Drive_axis_1r1733"], "DecimalSeparator",
",");
opts = setvaropts(opts, ["Xms", "C0Drive_axis_1r4821", "C1Drive_axis_1r4820", "C2Drive_axis_1r62",
"C3Drive_axis_1r63", "C4Drive_axis_1r77", "C5Drive_axis_1r76", "C6Drive_axis_1r1733"], "ThousandsSeparator",
".");

% Import the data
BancoEMAramp10 = readtable("C:\Users\buonp\OneDrive\Desktop\tesi
magistrale\TEST17_04\BancoEMA_ramp1,0.CSV", opts);

% conversioni

BancoEMAramp10.C0Drive_axis_1r4821(2:end)=BancoEMAramp10.C0Drive_axis_1r4821(2:end)*360/400000
00;
BancoEMAramp10.C1Drive_axis_1r4820(2:end)=BancoEMAramp10.C1Drive_axis_1r4820(2:end)*360/(40960*
tau);

BancoEMAramp10.C2Drive_axis_1r62(2:end)=BancoEMAramp10.C2Drive_axis_1r62(2:end)*2*pi/60;
BancoEMAramp10.C3Drive_axis_1r63(2:end)=BancoEMAramp10.C3Drive_axis_1r63(2:end)*2*pi/60;

%% Clear temporary variables
```

```
clear opts
x=BancoEMAramp10.Xms(2:end)/1000;  %tempo
y1=BancoEMAramp10.C0Drive_axis_1r4821(2:end); % [°] encoder position, fast shaft
y2=BancoEMAramp10.C1Drive_axis_1r4820(2:end); % [°] motor position, fast shaft
y3=BancoEMAramp10.C2Drive_axis_1r62(2:end); % [rad/s] speed setpoint after filter, fast shaft"
y4=BancoEMAramp10.C3Drive_axis_1r63(2:end); % [rad/s] actual speed smoothed, fast shaft"
y5=BancoEMAramp10.C4Drive_axis_1r77(2:end); % [A]current setpoint torque-generating (comando in corr)
y6=BancoEMAramp10.C5Drive_axis_1r76(2:end); % [A] current actual value torque generating (comando in corrente reale)
y7=BancoEMAramp10.C6Drive_axis_1r1733(2:end); % [A]   quadrature voltage setpoint

%correzzioni dovuti all'errore di siemens
k=y1(1)-y2(1);
y2(:)=y2(:)+k;
c=y2(32060)-y2(32061);
y2(32061:1:end)=y2(32061:1:end)+c;
y1(:)=y1(:)-y1(1);
y2(:)=y2(:)-y2(1);

%coeff che sostituisce il coeff di smorzamento viscoso dimensionale DC Motor (AV)
a=1;         % variano in base al comando
b=0.09564;

%valori medi

Media_speed_setpoint_after_filter_fast_shaft=mean(y3)
%Media_actual_speed_smoothed_fast_shaft_rads = mean(y4)
% mean(y5)
% mean(y7)
% mean(y6)


% Rappresentazione solo comando a rampa 0.01
plot(x,y1,x,y2)
legend("[°] encoder position","[°] motor position")
grid on
xlabel('time [s]')
ylabel('deg [°]')
% axis([0 1000000 0.071845 0.0725])

%Rappresentazione altre grandezze
figure
plot(x, y3,x, y4)
legend("[rad/s] speed setpoint after filter","[rad/s] actual speed smoothed")
grid on
xlabel('time [s]')

figure
plot(x, y5,x, y6,x, y7)
```

```
legend("[A] current setpoint torque-generating","[A] current actual value torque generating","[V] quadrature voltage setpoint")
% axis([0 10000 0.071824 0.071827])")
grid on
xlabel('time [s]')
```


1859
Politecnico
di Torino

Politecnico
di Torino

Bibliography

[1] Aircraft Control and Simulation: Dynamics, Controls Design, and Autonomous Systems by Brian L. Stevens and Frank L. Lewis – This text provides in-depth technical coverage of flight control systems, including both traditional and modern methods.

[2] https://www.lavionnaire.fr/ItaControllodelvolo.php

[3] Application of Modelica/MWorks on modeling, simulation and optimization for electro-hydraulic servo valve system, 2012, Ming Li, Jianping;

[4] Flight Stability and Automatic Control by Robert C. Nelson – This book covers the principles of flight control systems, including fly-by-wire technology and stability control.

[5] Modern Control Systems by Richard C. Dorf and Robert H. Bishop ;

[6] Qiao G, Liu G, Shi Z, Wang Y, Ma S, Lim TC. A review of electromechanical actuators for More/All Electric aircraft systems. *Proceedings of the Institution of Mechanical Engineers, Part C: Journal of Mechanical Engineering Science*. 2018;232(22):4128-4151.

[7] Janker P, Claeyssen F, Grohmann B, et al. New actuators for aircraft and space applications. In: *Eleventh international conference on new actuators*, Bremen, Germany, 9–11 June 2008, pp.346–354.

[8] Generalità sugli azionamenti elettrici e controllo di velocità, Fondamenti di Azionamenti elettrici; S. Bolognani, 25 settembre 2020.

[9] Claeyssen F. Grohamann B. Janker P, et al. «New actuators for aircraft and space applications.», International conference of new actuators, Bremen, Germany, June 2008.

[10] Sorli Massimo, Meccatronica, Dispense del corso, 2019.

[11] “Development and integration of a FBG optical sensor network for prognostics of electromechanical actuators”, Francesco Gerbino, 2022.

[12] “Development of an experimental test bench for the validation of prognostic algorithms for electromechanical actuators”, Matteo Bertone, 2022.

[13] “Experimental Validation of Multifidelity digital twins of electromechanical actuators for prognostics”; Simone Dei Rossi, 2023.

[14] “Development and Validation of Prognostic Algorithms for Electromechanical Actuators”, Pietro Sciandra, 2020.

[15] “Modellazione di un riduttore epicicloidale e relativa difettosità in un sistema di servocomando elettromeccanico EMA”, Riccardo Calamante, 2020.

[16] Fan L., Wang S., Wang X., Han F., Lyu H., «Nonlinear dynamic modeling of a helicopter planetary gear train for carrier plate crack fault diagnosis,» Chinese Journal of Aeronautics, vol. Vol 29(3) , pp. 675-687.

[17] Dalla Vedova M.D.L., Maggiore P., Riva G., Berri P. C., «Design and Development of a Planetary Gearbox for Electromechanical Actuator Test Bench through Additive Manufacturing,» Actuators, May 2020

[18] ISO/TR 14179-2:2001, Gears – Thermal capacity - Part 2: Thermal loadcarrying capacity

[19] N. Ludivion, ISO/TS 6336-4. Calcul de la capacité de charge au grippage des engrenages cylindriques, coniques et hypoïdes, 2016

[20] N. Ludivion, ISO/TS 6336-4. Calcul de la capacité de charge au grippage des engrenages cylindriques, coniques et hypoïdes, 2016.

[21] Savage M., Coy J.J., Townsend D.P., «The Optimal Design of Standard Gearsets,» The University of Akron. Propulsion Laboratory, U.S. Army Research and Technology Laboratories, NASA Lewis Research Center.

[22] Xinlei W., Changle X., Chunming L., Shenlong L., Yimin S., Liming W., «Effect of roughness on meshing power loss of planetary gear set considering elastohydrodynamic lubrication,» in Advances in Mechanical Engineers, vol. Vol. 12(2), 2020, pp. pp. 1-12.

[23] Ian H., Shengxiang J., Jiande W., «The dynamic modelling of a spur gear in mesh including friction and crack,» in Mechanical Systems and Signal Processing, vol. 15(5), 2001, pp. pp. 831-853

[24] https://docente.unife.it/emiliano.mucchi/a-a-2009-2010-meccanica-delle-macchine-e-dei-meccanismi/tutorial_KY.pdf/at_download/file

[25] Kuang J.H., Yang Y.T., «An estimate of mesh stiffness and load sharing ratio of a spur gear pair,» in International Power Transmission and Gearing Conference, 1992.

[26] R.G. Parker, J. Lin, «Mesh phasing relationships in planetary and epicyclic gears,» Journal of Mechanical Design, Transactions of the ASME, vol. Vol. 126, pp. pp. 365-370, 2004.

[27] Fan L., Wang S., Wang X., Han F., Lyu H., «Nonlinear dynamic modeling of a helicopter planetary gear train for carrier plate crack fault diagnosis,» Chinese Journal of Aeronautics, vol. Vol 29(3) , pp. 675-687.

[28] Certification Specifications and Acceptable Means of Compliance for Large Aeroplanes (CS-25)